

SYNTHESIS AND CHARACTERIZATION OF PLATINUM DECORATED IRON OXIDE
NANOPARTICLES FOR BIOMEDICAL APPLICATIONS

by

SoubantiKa PalChoudhury

DR. YUPING BAO, COMMITTEE CHAIR
DR. CHRISTOPHER S. BRAZEL
DR. SUBHADRA GUPTA
DR. STEPHEN M.C. RITCHIE
DR. C. HEATH TURNER

A DISSERTATION

Submitted in partial fulfillment of the requirements
for the degree of Doctor of Philosophy
in the Department of Chemical and Biological Engineering
in the Graduate School of
The University of Alabama

TUSCALOOSA, ALABAMA

2012

Copyright Soubantika Palchoudhury 2012
ALL RIGHTS RESERVED

ABSTRACT

This dissertation focuses on the development of a bifunctional nanoparticle system that can potentially offer simultaneous imaging and therapy in the future. Recently, small platinum (Pt) nanoparticles (< 5 nm) have shown great potential in therapeutic applications, such as DNA dissociation, radiation therapy, and oxidative stress treatment. Therefore, the small Pt nanoparticles of size comparable to DNA grooves are chosen as potential therapeutic components in this research. However, such small sized Pt nanoparticles tends to aggregate, and are difficult to target. Therefore, this research reports the synthesis, characterization, and DNA interaction of small Pt decorated iron oxide nanoparticles. The iron oxide carriers provide stability to the small Pt nanoparticles, and can potentially serve as MRI contrast agents. The hypothesis of this research is that the Pt nanoparticles supported on iron oxide nanoparticle surfaces can effectively interact with DNA molecules similar to the free Pt nanoparticles.

A reproducible synthetic technique was first developed to prepare iron oxide nanoparticles with excellent size control and narrow size distribution. Subsequently, two different approaches were utilized to produce multiple small Pt nanoparticle attached iron oxide nanoparticles. The first route involved attachment of Pt nanoparticles onto iron oxide seeds of various shapes in an organic solvent, followed by an aqueous phase transfer. Here, the shape of the nanoparticles was controlled to facilitate heterogeneous nucleation of Pt nanoparticles. The protective biocompatible polymer coating (polyacrylic acid) in this method could prevent interaction of the Pt nanoparticles with undesirable biomolecules. Several non-spherical iron oxide nanoparticles were explored, including whiskers, worms, plates, and flowers. In the second method, an

aqueous phase ligand exchange process was performed first, prior to the deposition of multiple Pt nanoparticles. This facile method provided more accessibility of the Pt nanoparticles for DNA interactions. The DNA interaction of these nanoparticles was investigated using gel electrophoresis, electron microscopy, dynamic light scattering, and atomic absorption spectroscopy. By comparing with control DNA, we suggested that two possible interactions between DNA and Pt-iron oxide nanoparticles were present: (1) DNA molecules directly linked to the Pt-iron oxide nanoparticles, and (2) DNA molecules de-attached the Pt nanoparticles from the iron oxide support.

This reported nanodrug system could potentially open up new possibilities in the design of therapeutic agents using multifunctional nanoparticles. Future efforts are to investigate the *in vivo* characteristics of this integrated nanostructure.

ACKNOWLEDGEMENTS

I am fortunate to have found an excellent mentor like ***Professor Yuping Bao***, who has helped me shape my professional career from start. I am greatly indebted to Dr. Bao for her enthusiasm, hands-on guidance, and advice that have immensely helped me in developing my research techniques, writing skills, and communicating ability.

It is a great honor to have Professor C. Heath Turner, Professor Steven M.C. Ritchie, Professor Christopher S. Brazel, and Professor Subhadra Gupta in my Ph. D. committee. I am sincerely obliged to them for their valuable guidance and suggestions.

I am greatly indebted to Professor Arunava Gupta for his constant support and guidance.

I owe a lot to the staff of the Central Analytical Facility, for training me on the characterization tools with great patience. I am especially thankful to Johnny Goodwin for his valuable training on the Transmission Electron Microscope, one of the most important instruments required in my work. I thank the MINT Center for the use of Alternating Gradient Field Magnetometer. I thank Lukai Yang for her help with the atomic absorption spectroscopy. I would also like to acknowledge Dr. Snigdha Palchaudhury for valuable suggestions in atomic absorption spectroscopic analysis. I also thank John M. Melnyczuk for valuable help during documentation.

I am grateful to the faculty and staff of our Department, and my lab members, especially Yaolin Xu, Amanda Rushdie, Rachel Michelle, Jesse McClung, and David Ward for their valuable help.

I would like to acknowledge my friends John M. Melnyczuk, Jayraj Shethji, and Adam Dayan for making research at the University of Alabama highly enjoyable.

Finally, I owe a very special thanks to my parents, Dr. Snigdha Palchaudhury and Dr. Santiranjan Palchaudhuri, and my little brother, Rangan Palchaudhuri for their constant love and support, without which my research would be incomplete.

Soubantika

CONTENTS

ABSTRACT	ii
ACKNOWLEDGEMENTS	iv
1 INTRODUCTION	1
2 LITERATURE REVIEW	12
2.1 Magnetism and Magnetic Properties of Nanoparticles	12
2.1.1 Magnetism.....	12
2.1.2 Magnetic Properties of Iron Oxide Nanoparticles	18
2.1.3 Crystal Structure of Iron Oxide.....	21
2.2 Synthesis of Magnetic Iron Oxide Nanoparticles	23
2.2.1 Synthetic Approaches	23
2.2.2 Shape Control of Iron Oxide Nanoparticles.....	26
2.3 Synthesis of Platinum Attached Iron Oxide Nanoparticles	28
2.4 Interaction of Platinum with DNA Molecules	29
2.5 Characterization of Nanoparticles.....	30
3 EXPERIMENTS, RESULTS, AND DISCUSSION	48
3.1 Iron Oxide Nanospheres	48
3.2 Platinum Attached Iron Oxide Nanoparticles via Organic Route.....	54

3.3 Shape Controlled Iron Oxide Nanoparticles	61
3.3.1 Iron Oxide Nanowhiskers	61
3.3.2 Iron Oxide Nanoworms.....	73
3.3.3 Iron Oxide Nanoplates and Nanoflowers.....	77
3.4 Water Soluble Iron Oxide Nanoparticles	86
3.5 Platinum Attached Iron Oxide Nanoparticles via Aqueous Route	89
3.6 DNA Interaction of Platinum Attached Iron Oxide Nanoparticles.....	92
4 FUTURE WORK.....	108
4.1 Synthesis	108
4.1.1 Iron Oxide Nanoworms and Nanofishes.....	108
4.1.2 Platinum Attachments on Iron Oxide Nanoparticles of Other Shapes	109
4.1.3 Phase Transfer of the Integrated Nanoparticles Synthesized via Organic Route .	109
4.1.4 Polymer Encapsulation of the Platinum-Iron Oxide Integrated Nanoparticle	110
4.2 Characterization	111
4.2.1 Quantification	111
4.2.2 Simulation	112
4.3 Biological Studies	112
4.3.1 DNA Interaction of Platinum Attached Iron Oxide Nanoparticles In Vitro.....	113

4.3.2	Platinum Attached Iron Oxide Nanoparticles as Radiation Therapy Enhancers ..	113
5 CONCLUSION.....		119
APPENDIX.....		125

CHAPTER 1

INTRODUCTION

Small Pt nanoparticles (NPs) have recently drawn much attention due to their reported therapeutic abilities. For example, Pt NPs showed great potential as sensitizers for cancer radiation therapy.¹ They could enhance the DNA double strand breaks in proton therapy by a factor of 2.² Here, the Auger electrons from de-excitation of the irradiated Pt NPs (< 5 nm) could ionize the surrounding water molecules, and excite the adjacent atoms. This auto-amplification of the radiation induced higher double strand breaks, lethal to the cancer cells. The radiation energy deposition was calculated to be most effective for small, high- atomic number (Z) NPs (< 5 nm).^{3,4} Pt NPs also held great promise in free radical scavenging for oxidative stress treatment. Polyacrylic acid (PAA) coated Pt NPs (2 nm) could effectively scavenge reactive oxygen species (ROS).⁵ The scavenging activity was comparable to that of antioxidant cellular defense enzymes such as, superoxide dismutase.⁶ Recently, Pt NPs were shown to partially mimic the function of mitochondrial complex I (nicotinamide adenine dinucleotide: ubiquinone oxidoreductase).⁷ This is attractive for the treatment of oxidative stress disease caused by mitochondrial complex I deficiency. Another potential application of Pt NPs is chemotherapy. Pt complexes have served as one of the most efficient anticancer drugs in chemotherapy.^{8,9} Intravenously administered Pt complex drugs are activated by hydrolysis to form replication-inhibiting DNA adducts (interstrand, intrastrand, and protein).^{10,11} The hydrolysis of the inert Pt is slow compared to other metals (*e.g.*, Pd). Therefore, the hydrolyzed Pt complexes are more likely to reach the target tumor.¹² However, thiol groups in the body have a high affinity for Pt^{2+} , and limit the

DNA binding of Pt complexes on continued exposure.^{13,14} Consequently, the high doses of Pt complex drugs required can cause nephrotoxic side effects, like kidney toxicity, nausea, hearing impairment, and peripheral nerve damage. Recently, DNA templated synthesis of Pt NPs suggested their ability to complex with DNA nucleobases (guanine).^{15,16,17} This observation indicate the great promise of Pt NPs for chemotherapy.

A low IC₅₀ (drug concentration required to inhibit cell growth by 50% compared to controls) of Pt based yolk-shell NPs supported the chemotherapeutic potential of Pt NPs.^{18,19} Release of Pt²⁺ species following endocytosis²⁰ of the Pt NPs, or ROS production were proposed as probable causes of increased cell (HeLa) death.²¹ Folic acid capped Pt NPs showed such endocytosis mediated Pt²⁺ conversion to kill breast cancer cells.²² The second mechanism of ROS production is often associated with the decrease of glutathione level in the body. Such glutathione depletion was observed after uptake of Pt NPs by human colon carcinoma cells. However, further analysis assigned this depletion to covalent DNA-NP and thiol-NP adduct formation.²³ In *Salmonella Enteriditidis*, the DNA-Pt NP bindings could disintegrate the cell walls.²⁴ These results show the antitumor potential of Pt NPs. A key advantage of Pt NPs over Pt complex anticancer drugs is the multiple therapeutic potential of these NPs. A simple, target-specific delivery is also possible with the NPs.²⁵ The high surface area NPs can be targeted via conjugation with peptides, antibodies, or proteins. However, challenges such as aggregation and poor circulation time need to be tackled for effective use of Pt NPs in chemotherapy. The small Pt NPs show aggregation due to their high surface energy, and their quick detection by the reticuloendothelial system (RES) is a challenge for targeting.²⁶

A structural support for the small Pt NPs could overcome the rapid clearance and aggregation. Recently, small Pt NPs loaded onto a TiO₂/SiO₂ support induced apoptosis of

glioma cells.^{27,28} Iron oxide NPs would provide more biocompatibility, compared to these support materials.²⁹ First, Food & Drug Administration (FDA) approved dextran-coated iron oxide NPs are currently in clinical use.^{30,31} Second, human tissues contain approximately 3.5 g iron (hemosiderin, ferritin, and transferring).³² Therefore, the iron oxide NPs can be potentially reabsorbed through normal iron metabolic pathways. Additionally, iron oxide NPs hold great potential as magnetic resonance imaging (MRI) contrast agents. Ferridex (Endorem-Guerbet, Ferumoxide, AMI-25 in initial clinical development by Advanced Magnetics) was the first superparamagnetic iron oxide NP contrast agent approved by the FDA. This compound had to be slowly infused to avoid cardiovascular side effects. This led to the second clinically approved iron oxide NP contrast agent, ferucarbotran (Resovist, Schering). Both of these compounds are liver-specific. Recently, iron oxide nanoworms showed good circulation time for tumors in other locations.^{33,34} The results suggested the good biocompatibility and imaging ability of the iron oxide NPs. Therefore, an integrated Pt NP decorated iron oxide NP could potentially offer simultaneous imaging and therapy.

This research reports the synthesis, characterization, and DNA interaction of multiple Pt NP-attached iron oxide NPs. Here, multiple small Pt NPs are attached to iron oxide NP surfaces. The hypothesis is that the Pt NPs attached to iron oxide seeds can effectively interact with the DNA, similar to the free Pt NPs reported in literature (Figure 1). After successfully destroying the cancer cell DNA, the nanodrug inside the dead cancer cell can be potentially removed from the body by macrophages.^{35,36} The small sized Pt NPs (~ 2 nm) can potentially fit into DNA grooves³⁷ for efficient DNA-NP interaction.³⁸ The multiple small Pt NPs could potentially serve as the therapeutic agent in the future. The iron oxide NP support could act as the contrast agent

in MRI. To potentially increase the drug payload in the future, multiple small Pt NPs are attached per iron oxide carrier NP.

Multiple Pt NP attachments had proved challenging so far. Single Pt attached iron oxide NPs (dimer NPs) were synthesized by growing Fe on pre-formed Pt NP seeds.^{39,40} However, the strong interaction between metal NPs (electron flow at Fermi level from iron oxide NPs to Pt NPs) limited further attachments in this method. In other reports, iron oxide NP overgrowth caused Pt NPs to be completely embedded inside core-shell structures. The size of the Pt NPs was difficult to control in all these methods. For example, uncontrolled reduction led to flower-like Pt NPs.⁴¹ The limitations of most of these synthetic techniques arise from growing iron oxide NPs on pre-formed Pt NPs. So, our approaches to obtain multiple Pt NP attachments involve synthesis of iron oxide NPs, prior to Pt attachment reactions.

Two routes were followed to synthesize water soluble multiple Pt attached iron oxide NPs. In the first method, Pt NPs were grown on iron oxide NP surfaces in an organic solvent, followed by an aqueous phase transfer of the integrated NP. The organic ligand coating and shape of the iron oxide NPs were modified to facilitate heterogeneous nucleation of Pt NPs.⁴² Iron oxide nanoplates, nanoflowers, nanoworms, and nanowhiskers were reproducibly synthesized in the process. Here, the biocompatible polymer that coats the whole NP can potentially minimize the loss of therapeutic Pt NPs before reaching the target. The second method involved bringing the iron oxide NP seeds to the aqueous phase, prior to deposition of multiple Pt NPs onto the biocompatible polymer coating the seeds. This approach makes the Pt NPs more accessible for DNA interaction. Next, DNA interaction of the integrated NPs was investigated for proof of concept.

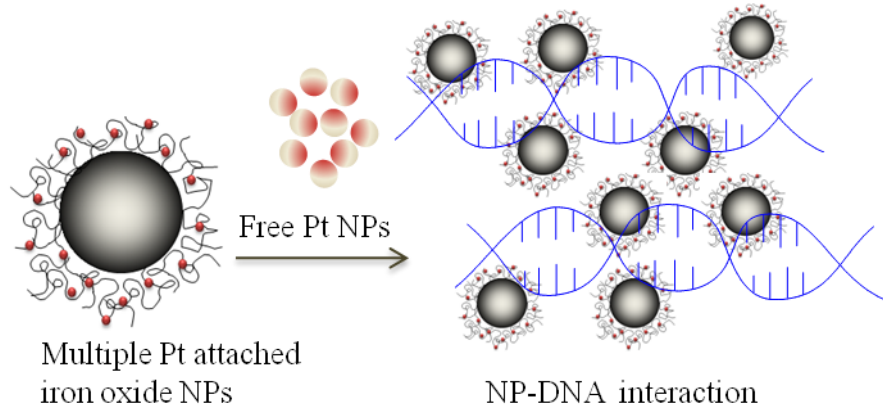


Figure 1. Research hypothesis: multiple small Pt NPs attached on iron oxide NPs can interact with the DNA like free Pt NPs (NPs not drawn to scale).

This dissertation will include research background, methods and results, future work, and conclusion. The research background will cover magnetic properties of NPs, spinel magnetic NP structure, NP synthesis, shape control, characterization tools, and possible NP-DNA interaction mechanisms (Chapter 2). Chapter 3 will discuss the experimental details and results. Specifically, these studies are the single and multiple Pt NP attachments on spherical iron oxide NPs in organic solvent, shape control of iron oxide NPs in organic solvents, synthesis and formation mechanisms of iron oxide nanoworms, nanowhiskers, nanoplates, and nanoflowers, an aqueous route for multiple Pt NP attachments, and DNA interaction experiments using aqueous Pt attached iron oxide NPs. Finally, this will be followed by the future work (Chapter 4), and conclusion (Chapter 5).

References

1. Kobayashi, K.; Usami, N.; Porcel, E.; Lacombe, S.; Le Sech, C., Enhancement of radiation effect by heavy elements. *Mutation Research-Reviews in Mutation Research* **2010**, *704* (1-3), 123-131.
2. Porcel, E.; Liehn, S.; Remita, H.; Usami, N.; Kobayashi, K.; Furusawa, Y.; Le Sech, C.; Lacombe, S., Platinum nanoparticles: a promising material for future cancer therapy? *Nanotechnology* **2010**, *21* (8), 085103(1-7).
3. Carter, J. D.; Cheng, N. N.; Qu, Y.; Suarez, G. D.; Guo, T., Nanoscale energy deposition by x-ray absorbing nanostructures. *Journal of Physical Chemistry B* **2007**, *111* (40), 11622-11625.
4. Pradhan, A. K.; Nahar, S. N.; Montenegro, M.; Yu, Y.; Zhang, H. L.; Sur, C.; Mrozik, M.; Pitzer, R. M., Resonant x-ray enhancement of the auger effect in high-Z atoms, molecules, and nanoparticles: potential biomedical applications. *Journal of Physical Chemistry A* **2009**, *113* (45), 12356-12363.
5. Watanabe, A.; Kajita, M.; Kim, J.; Kanayama, A.; Takahashi, K.; Mashino, T.; Miyamoto, Y., In vitro free radical scavenging activity of platinum nanoparticles. *Nanotechnology* **2009**, *20* (45), 455105(1-9).
6. Kajita, M.; Hikosaka, K.; Iitsuka, M.; Kanayama, A.; Toshima, N.; Miyamoto, Y., Platinum nanoparticle is a useful scavenger of superoxide anion and hydrogen peroxide. *Free Radical Research* **2007**, *41* (6), 615-626.
7. Hikosaka, K.; Kim, J.; Kajita, M.; Kanayama, A.; Miyamoto, Y., Platinum nanoparticles have an activity similar to mitochondrial NADH : ubiquinone oxidoreductase. *Colloids and Surfaces B-Biointerfaces* **2008**, *66* (2), 195-200.

8. Bhattacharya, R.; Mukherjee, P., Biological properties of "naked" metal nanoparticles. *Advanced Drug Delivery Reviews* **2008**, *60* (11), 1289-1306.
9. Sherman, S. E.; Lippard, S. J., Structural aspects of platinum anticancer drug-interactions with DNA. *Chemical Reviews* **1987**, *87* (5), 1153-1181.
10. Rosenberg, B; Vancamp, L.; Krigas, T., Inhibition of cell division in *escherichia coli* by electrolysis products from a platinum electrode. *Nature* **1965**, *205* (4972), 698-699.
11. Lippard, S. J., Chemistry and molecular-biology of platinum anticancer drugs. *Pure and Applied Chemistry* **1987**, *59* (6), 731-742.
12. Abu-Surrah, A. S.; Al-Sa'doni, H. H.; Abdalla, M. Y., Palladium-based chemotherapeutic agents: routes toward complexes with good antitumor activity. *Cancer Therapy* **2008**, *6*, 1-10.
13. Bose, R. N.; Ghosh, S. K.; Moghaddas, S., Kinetic analysis of the cis-diamminedichloroplatinum(II)-cysteine reaction: implications to the extent of platinum-DNA binding. *Journal of Inorganic Biochemistry* **1997**, *65* (3), 199-205.
14. Zhang, K.; Chew, M.; Yang, E. B.; Wong, K. P.; Mack, P., Modulation of cisplatin cytotoxicity and cisplatin-induced DNA cross-links in HepG2 cells by regulation of glutathione-related mechanisms. *Molecular Pharmacology* **2001**, *59* (4), 837-843.
15. Yang, J.; Lee, J. Y.; Too, H.-P.; Chow, G.-M.; Gan, L. M., Stabilization of Pt nanoparticles by single stranded DNA and the binary assembly of Au and Pt nanoparticles without hybridization. *Journal of Nanoparticle Research* **2006**, *8* (6), 1017-1026.
16. Berti, L.; Burley, G. A., Nucleic acid and nucleotide-mediated synthesis of inorganic nanoparticles. *Nature Nanotechnology* **2008**, *3* (2), 81-87.

17. Seidel, R.; Ciacchi, L. C.; Weigel, M.; Pompe, W.; Mertig, M., Synthesis of platinum cluster chains on DNA templates: Conditions for a template-controlled cluster growth. *Journal of Physical Chemistry B* **2004**, *108* (30), 10801-10811.
18. Gao, J.; Liang, G.; Zhang, B.; Kuang, Y.; Zhang, X.; Xu, B., FePt@CoS₂ yolk-shell nanocrystals as a potent agent to kill HeLa cells. *Journal of the American Chemical Society* **2007**, *129* (5), 1428-1433.
19. Gao, J. H.; Liang, G. L.; Cheung, J. S.; Pan, Y.; Kuang, Y.; Zhao, F.; Zhang, B.; Zhang, X. X.; Wu, E. X.; Xu, B., Multifunctional yolk-shell nanoparticles: a potential MRI contrast and anticancer agent. *Journal of the American Chemical Society* **2008**, *130* (35), 11828-11833.
20. Scott, C.; Gruenberg, J., Ion flux and the function of endosomes and lysosomes: pH is just the start. *Bioessays* **2010**, *33*, 103-110.
21. Asharani, P. V.; Xinyi, N.; Hande, M. P.; Valiyaveettil, S., DNA damage and p53-mediated growth arrest in human cells treated with platinum nanoparticles. *Nanomedicine* **2010**, *5* (1), 51-64.
22. Teow, Y.; Valiyaveettil, S., Active targeting of cancer cells using folic acid-conjugated platinum nanoparticles. *Nanoscale* **2010**, *2* (12), 2607-2613.
23. Pelka, J.; Gehrke, H.; Esselen, M.; Tuerk, M.; Crone, M.; Braese, S.; Muller, T.; Blank, H.; Send, W.; Zibat, V.; Brenner, P.; Schneider, R.; Gerthsen, D.; Marko, D., Cellular uptake of platinum nanoparticles in human colon carcinoma cells and their impact on cellular redox systems and DNA integrity. *Chemical Research in Toxicology* **2009**, *22* (4), 649-659.
24. Sawosz, E.; Chwalibog, A.; Szeliga, J.; Sawosz, F.; Grodzik, M.; Rupiewicz, M.; Niemiec, T.; Kacprzyk, K., Visualization of gold and platinum nanoparticles interacting with

Salmonella Enteritidis and Listeria Monocytogenes. *International Journal of Nanomedicine* **2010**, *5*, 631-637.

25. Gu, F. X.; Karnik, R.; Wang, A. Z.; Alexis, F.; Levy-Nissenbaum, E.; Hong, S.; Langer, R. S.; Farokhzad, O. C., Targeted nanoparticles for cancer therapy. *Nano Today* **2007**, *2* (3), 14-21.
26. Choi, H. S.; Liu, W.; Misra, P.; Tanaka, E.; Zimmer, J. P.; Ipe, B. I.; Bawendi, M. G.; Frangioni, J. V., Renal clearance of quantum dots. *Nature Biotechnology* **2007**, *25*, 1165-1170.
27. Lopez, T.; Figueras, F.; Manjarrez, J.; Bustos, J.; Alvarez, M.; Silvestre-Albero, J.; Rodriguez-Reinoso, F.; Martinez-Ferre, A.; Martinez, E., Catalytic nanomedicine: a new field in antitumor treatment using supported platinum nanoparticles. In vitro DNA degradation and in vivo tests with C6 animal model on Wistar rats. *European Journal of Medicinal Chemistry* **2010**, *45* (5), 1982-1990.
28. Lopez, T.; Islas, E.; Lemus, M.; Gonzalez, R., Nanostructured Pt(NH₃)₄Cl₂/SiO₂ for nanomedicine: catalytic degradation of DNA in cancer cells. *Nano Reviews* **2011**, *2*, 1-7.
29. Colombo, M.; Carregal-Romero, S.; Casula, M. F.; Gutierrez, M.; Morales, M. P.; Bohm, I. B.; Herverhagen, J. T.; Prosperi, D.; Parak, W. J., Biological applications of magnetic nanoparticles. *Chemical Society Reviews* **2012**.
30. Jung, C. W.; Jacobs, P., Physical and chemical-properties of superparamagnetic iron-oxide MR contrast agents - ferumoxides, ferumoxtran, ferumoxsil. *Magnetic Resonance Imaging* **1995**, *13* (5), 661-674.
31. Fang, C.; Bhattacharai, N.; Sun, C.; Zhang, M., Functionalized nanoparticles with long-term stability in biological media. *Small* **2009**, *5* (14), 1637-1641.

32. Reimer, P.; Balzer, T., Ferucarbotran (Resovist): a new clinically approved RES-specific contrast agent for contrast-enhanced MRI of the liver: properties, clinical development, and applications. *European Radiology* **2003**, *13* (6), 1266-1276.
33. Park, J. H.; von Maltzahn, G.; Zhang, L. L.; Schwartz, M. P.; Ruoslahti, E.; Bhatia, S. N.; Sailor, M. J., Magnetic iron oxide nanoworms for tumor targeting and imaging. *Advanced Materials* **2008**, *20* (9), 1630-1631.
34. Gossuin, Y.; Disch, S.; Vuyong, Q. L.; Gillis, P.; Hermann, R. P.; Park, J. H.; Sailor, M. J., NMR relaxation and magnetic properties of superparamagnetic nanoworms. *Contrast Media and Molecular Imaging* **2010**, *5* (6), 318-322.
35. Sears, H. C.; Kennedy, C. J.; Garrity, P. A., Macrophage-mediated corpse engulfment is required for normal Drosophila CNS morphogenesis. *Development* **2003**, *130* (15), 3557-3565.
36. Schrijvers, D. M.; De Meyer, G. R. Y.; Herman, A. G.; Martinet, W., Phagocytosis in atherosclerosis: molecular mechanisms and implications for plaque progression and stability. *Cardiovascular Research* **2007**, *73* (3), 470-480.
37. Watson, J. D.; Crick, F. H. C., Molecular-structure of nucleic-acids - a structure for deoxyribose nucleic-acid. *JAMA-Journal of the American Medical Association* **1993**, *269* (15), 1966-1967.
38. Liu, Y. P.; Meyer-Zaika, W.; Franzka, S.; Schmid, G.; Tsoli, M.; Kuhn, H., Gold-cluster degradation by the transition of B-DNA into A-DNA and the formation of nanowires. *Angewandte Chemie-International Edition* **2003**, *42* (25), 2853-2857.
39. Wang, C.; Daimon, H.; Sun, S. H., Dumbbell-like Pt-Fe₃O₄ nanoparticles and their enhanced catalysis for oxygen reduction reaction. *Nano Letters* **2009**, *9* (4), 1493-1496.

40. Wang, C.; Xu, C. J.; Zeng, H.; Sun, S. H., Recent progress in syntheses and applications of dumbbell-like nanoparticles. *Advanced Materials* **2009**, *21* (30), 3045-3052.
41. Choi, S. H.; Bin Na, H.; Park, Y. I.; An, K.; Kwon, S. G.; Jang, Y.; Park, M.; Moon, J.; Son, J. S.; Song, I. C.; Moon, W. K.; Hyeon, T., Simple and generalized synthesis of oxide-metal heterostructured nanoparticles and their applications in multimodal biomedical probes. *Journal of the American Chemical Society* **2008**, *130* (46), 15573-15580.
42. Kashchiev, D.; van Rosmalen, G. M., Review: nucleation in solutions revisited. *Crystal Research and Technology* **2003**, *38* (7-8), 555-574.

CHAPTER 2

LITERATURE REVIEW

This chapter gives an introduction about the iron oxide NPs, Pt-iron oxide NP heterostructures, DNA interactions of the free Pt NPs, and the different techniques used for NP characterization. The goal of this research is to synthesize multiple Pt-attached iron oxide NPs and to prove their ability to interact with DNA like the free Pt NPs. Therefore, the basic magnetic properties and structure of the iron oxide NPs are first explained to better understand the iron oxide NPs used in this research. Subsequently, the literature methods used to synthesize iron oxide NPs and iron oxide supported Pt NPs are reviewed in detail. Next, the recent reports of DNA interactions of free Pt NPs are overviewed to better understand the DNA-NP interactions in this research. Finally, the characterization techniques used to study the size, morphology, crystal structure, chemical composition, and DNA interactions of the NPs in this research are introduced in detail.

2.1 Magnetism and Magnetic Properties of Nanoparticles

2.1.1 Magnetism

Magnetism is a result of the movement of the negatively charged electrons within the material.¹ The electron spins around its axis to create a magnetic field known as the orbital magnetic moment of the electrons. The spin magnetic moment of electrons comes from their inherent parallel or antiparallel spin states. In an orbital, paired electrons with opposite spins cancel the moment of each other. Materials with uncancelled moments can respond to an

external magnetic field.² The common terms to explain material magnetic properties are summarized in Table 2.1. Table 2.2 lists the magnetic units (CGS, and SI).

Table 2.1. Magnetic terms.

Magnetic property	Definition
Magnetic field, H	A unit magnetic field exerts 1 dyne force on a unit magnetic pole
Magnetic flux density, B	Magnetic field induced within a substance in external magnetic field
Magnetic moment, m	Moment of couple exerted on the material by a perpendicular field
Magnetization, M	Tendency of magnetic moments within the material to align with the applied field
Permeability, μ	B/H (Vacuum permeability, μ_0 is treated as a universal constant)
Relative permeability, μ_r	Tendency of the substance to get magnetized by an applied field
Magnetic susceptibility, χ	Indicates the response of the material to an applied field ($=\mu_r - 1$)

Table 2.2. Magnetic units.

Magnetic property	Unit (CGS)	Unit (SI)	Conversion factor
H	Oersted (Oe)	A/m	$1 \text{ A/m} = 4\pi/10^3 \text{ Oe}$
B	Gauss (G)	Tesla (T)	$1 \text{ T} = 10^4 \text{ G}$
m	emu	Am^2	$1 \text{ Am}^2 = 10^3 \text{ emu}$
M	emu/ cm ³	A/m	$1 \text{ A/m} = 10^{-3} \text{ emu/cm}^3$
μ_0	-	H/m	$4\pi \times 10^{-7} \text{ H/m} = 1 \text{ (cgs)}$
μ_r	dimensionless	dimensionless	
χ	dimensionless	dimensionless	$4\pi \text{ (SI)} = 1 \text{ (cgs)}$

Bulk materials can be classified as diamagnetic, paramagnetic, ferromagnetic, ferrimagnetic, or antiferromagnetic depending on their response to an applied magnetic field (Table 2.3). In diamagnetic materials, the electrons spin faster to resist the externally applied magnetic field. The weak negative magnetization disappears with removal of the applied field. Diamagnetism

occurs when all the orbitals in an atom are filled with paired electrons. These materials show a negative susceptibility that is temperature independent. All materials are diamagnetic to some extent, as they possess electrons. However, if present, the other forms of magnetism dominate over the weak diamagnetic phenomenon in a material. Examples of diamagnetic materials include noble gases, metals (*e.g.*, Cu, Ag, Au, Bi, and Hg), non-metallic elements (*e.g.*, P and S), diatomic gases (*e.g.*, H₂ and N₂), and organic compounds.

Incomplete cancellation of the magnetic moment (orbital or spin) in unpaired electrons causes permanent atomic dipoles within the material. The dipoles show negligible interaction with each other. This behavior is called paramagnetism, and can be explained via Langevin theory. The Langevin theory explains that the atomic dipoles of a paramagnet orient randomly (zero magnetization) in the absence of an external magnetic field. When a magnetic field is applied, the dipoles try to align with the field. However, their random thermal motions prevent such alignment. This creates a relatively small, but positive susceptibility. The magnetic susceptibility of a paramagnet varies with temperature, according to Curie's law.^{1,2} Metals (Cr and Mn), diatomic gases (O₂ and NO), salts, oxides, and ions of transition and rare earth metals show paramagnetism.

In ferromagnetic materials, the electrons are not oriented to cancel the individual magnetic moments like dia and paramagnets. Here, the atoms band together in magnetic domains, where all electrons share the same orientation. However, different domains align randomly to be energetically favorable. This leaves a net weak magnetic moment in ferromagnets. Domain walls with rapidly changing electron spins separate the individual domains. An external field induces a high magnetization in ferromagnets because the individual domains are forced to coalesce into larger domains aligned with the field.³ The ferromagnets show a large susceptibility, and retain

the magnetization even after removal of the external field. This property of ferromagnets is called hysteresis.

- The flux density, B , in a ferromagnet is not proportional to the field, H . The domain boundaries move such that the domains nearly parallel to the applied field grow in size at the cost of unfavorably oriented domains. Therefore, M and B increase with H until saturation. Here, the material becomes a single domain oriented with the field. Upon reversal of the applied field, the single domain first rotates with the reversed field. The domains then rearrange so that the domains oriented with the new field direction increase in size. However, the increase of H in the opposite direction causes a resistance to the movement of the domain walls. This induces a slower decrease rate of B or M compared to H . The lagging of the M -field (or B -field) behind the H -field is the **hysteresis** effect. A residual or **remanent magnetization**, M_r , exists even when the applied field is reduced to zero. To reduce the magnetization of the ferromagnet to zero, it is necessary to apply a magnetic field in a direction opposite to that of the original field. This opposite magnetic field is called the **coercivity**, H_c (Table 2.3).
- The shape of the hysteresis curve shows the ability of the material to get magnetized and retain the magnetism. Soft magnetic materials (*e.g.*, permalloy, commercial iron ingot, and supermalloy) have a small hysteresis loop due to the relative ease of movement of their domain walls during magnetization and demagnetization. They are used as electromagnets or transformer cores. Hard magnets like tungsten and cobalt show more difficult domain wall motion, and a larger hysteresis loop. These hard magnets are ideal as permanent magnets because they are not easily magnetized or demagnetized.

The parallel electronic orientation within the domains is destroyed by the thermal motion of atoms above the **Curie temperature**.^{1,2} This temperature is higher relative to paramagnets. Fe, Ni, Co, and many of their alloys are typical ferromagnetic materials.

Ferrimagnetism is closely related to ferromagnetism. Ferrimagnetic materials are ionic compounds with M_a -O- M_b type linkage (Figure 2.1).⁴ Here, superexchange interaction between cation and anion wave functions indirectly couples the two cations. The oxygen anion interacts with the *d*-electrons of the transition metal ions. Since, the *a* and *b* sublattices are dissimilar, three possible interactions need to be considered for explaining the ferrimagnetic behavior. The *a*-*b* interaction between nearest neighbors attempts to align the magnetic moments antiparallel to each other. The *a*-*a* and *b*-*b* interactions in favor of parallel orientation of moments oppose the *a*-*b* interactions. This leaves a net magnetization, lower than that of a ferromagnet even in the absence of an applied magnetic field. Ferrimagnetism is destroyed above the Curie temperature. The susceptibility of ferrimagnets follows the Weiss law of ferromagnets. Ferrites, such as cobalt ferrite, manganese ferrite, magnetite, and maghemite, are the most important ferrimagnets.

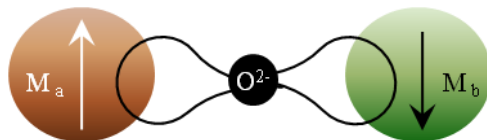


Figure 2.1. Superexchange interaction between metals M_a and M_b .

Antiferromagnetic materials also show superexchange interaction like ferrimagnets. The two identical, interpenetrating magnetic ion sublattices in antiferromagnets show opposite magnetic orientations below the Néel temperature.^{1,2} Therefore, below the Néel temperature,^{1,2} antiferromagnets have zero net magnetization in the presence of an external field. However, the antiparallel orientation is disrupted above this temperature. A paramagnet-like behavior is now

induced. Transition metal oxides, such as, MnO , CoO , NiO , and Cr_2O_3 are typical antiferromagnetic materials.

Table 2.3 summarizes the different material magnetic characteristics. These basic magnetic properties will help in understanding the magnetic characteristics of iron oxide NPs used in this research.⁵ Magnetic behavior of NPs such as magnetophoresis, and magnetic relaxation is useful for biomedical applications.⁶

Table 2.3. Classification of the magnetic materials

Materials	Magnetic orientation of atoms			Critical T	Susceptibility χ	
	Before applied field	Applied field	After applied field		Magnitude	T variation
Diamagnetic				None		
Paramagnetic				None		
Ferromagnetic				Curie T θ_c		
Ferrimagnetic				Curie T θ_c	Similar to ferromagnetic behavior	Similar to ferromagnetic behavior
Antiferromagnetic				Néel T θ_N	Similar to paramagnetic behavior	

2.1.2 Magnetic Properties of Iron Oxide Nanoparticles

The most interesting iron oxides found in nature are hematite ($\alpha\text{-Fe}_2\text{O}_3$), the strongly magnetic magnetite (Fe_3O_4), and its weathered form, maghemite ($\gamma\text{-Fe}_2\text{O}_3$). The unpaired $3d$ electrons (4 or 5) are responsible for the strong magnetic behavior of iron oxides (especially, Fe_3O_4 and $\gamma\text{-Fe}_2\text{O}_3$). However, magnetic properties of iron oxide NPs differ from the bulk behavior. For example, the size, morphology, and surface coating of the NP greatly affect the coercivity or susceptibility of the NP. In NPs below a critical size (**radius, R_c**), only one magnetic domain is energetically favored, compared to multiple domains in the bulk. A **single domain** particle contains high magnetostatic energy caused by the internal and external magnetic field. However, there is no domain wall (or exchange) energy. The critical radius for a single domain can be derived by balancing these two energies. The magnetostatic energy (ϵ_{ex}) of a single domain sphere of radius R and saturation magnetization M_s is given by:

$$\epsilon_{ex} = \frac{1}{2} \left(\frac{4\pi}{3} \right)^2 M_s^2 R^3 \quad 1$$

Additionally, anisotropy is the dependence of magnetic energy on a particular direction. For a sphere with a high anisotropy (K_u), the total energy consists of the magnetostatic energy of a half sphere and the domain wall energy:

$$\epsilon_{wall} = \pi R^2 (AK)^{1/2} \quad 2$$

where A and K are the exchange stiffness and anisotropy constants, respectively. In this case, the critical radius, R_c , for a stable single domain particle is given by:

$$R_c = \frac{9(AK)^{1/2}}{4\pi M_s^2} \quad 3$$

If the single domain sphere has a low anisotropy, the magnetization alignment follows the direction of the surface. In this case the exchange energy should be integrated over the entire surface of the sphere, as follows:

$$\varepsilon_{ex} = \frac{3A}{R^2} \left[\ln\left(\frac{2R}{a}\right) - 1 \right] \quad 4$$

where a is the radius of the core singularity. Here, the critical radius requires a graphical solution, and is expressed as:

$$R_c = \sqrt{\frac{9A}{4\pi M_s^2} \left[\ln\left(\frac{2R_c}{a}\right) - 1 \right]} \quad 5$$

The radius of a single domain state of magnetite is ~ 70 nm.

Superparamagnetism is another attractive magnetic property found in NPs (Figure 2.2). In this phenomenon the NPs rapidly magnetize with the applied magnetic field, and reach zero net magnetization ($H_c = 0$, $M_r = 0$) on removal of the field. This rapid demagnetization will prevent aggregation and rapid removal of NPs *in vivo* following application of a magnetic field (such as MRI or hyperthermia). Therefore, superparamagnetism of NPs is attractive for biomedical applications. The NPs exhibit superparamagnetism above the critical temperature, **T_b** (**blocking temperature**). Above T_b, the motion of individual magnetic moments within the NP (thermal energy) is sufficient to flip the magnetic spin direction in a NP (anisotropy energy). However, it cannot overcome the exchange energy. Therefore, in the absence of an applied field, T_b can be derived by equating the thermal and anisotropy energies.

$$T_b = \frac{VK_V}{25k_B} \quad 6$$

where, V is NP volume, K_V is anisotropy constant, and k_B is Boltzmann's constant.

The magnetic anisotropy constant is low in small NPs. This allows a blocking temperature that is below the room temperature. Therefore, such NPs are superparamagnetic at normal temperatures.⁷ Iron oxide NPs in the size range of 6 - 15 nm show superparamagnetism at room temperatures. At elevated temperatures (above the Curie or Néel critical limit), the magnetic order in iron oxide NPs is destroyed by vigorous thermal fluctuations.

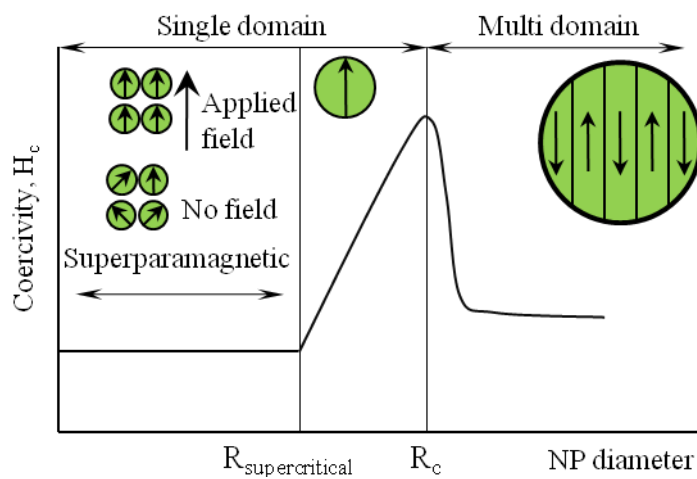


Figure 2.2. Size-dependent magnetic behavior of small spherical NPs.

The magnetic property of iron oxide NPs depends on the crystal phase. Magnetite shows ferrimagnetism at room temperature (Curie temperature = 850 K). The saturation magnetization for bulk magnetite is 92 emu/g.^{8,9} However, magnetite NPs below 6 nm are superparamagnetic at room temperatures.¹⁰ The magnetic properties of magnetite NPs is closely related to the synthesis method and surface coatings. The morphology of magnetite NPs can also affect their magnetic characteristics. For example, NP coercivity increases in the order sphere < cubes < octahedral. Maghemite is also ferrimagnetic at room temperatures but undergoes a phase change to hematite at ~ 400 °C. This irreversible crystallographic transformation to hematite makes it difficult to measure the accurate Curie temperature for maghemite (~ 820 K – 926 K). Bulk maghemite shows a saturation magnetization of 78 emu/g.¹¹ However, small (< 10 nm) maghemite NPs are

superparamagnetic at room temperature. Interestingly, magnetic coupling (superferromagnetism) is sometimes observed between aggregated maghemite NPs. Both the forms of iron oxide described above are strongly magnetic, with the unique capacity of superparamagnetism in the small size range. In contrast, hematite shows a weak ferromagnetism at room temperatures, and becomes antiferromagnetic above the Morin temperature (260 K). The saturation magnetization of bulk hematite (~0.4 emu/g) is low compared to maghemite. Therefore, the maghemite and magnetite NPs are more suitable for biomedical research, such as imaging and drug delivery. Both magnetite and maghemite show a spinel crystallographic structure.

2.1.3 *Crystal Structure of Iron Oxide*

There are approximately 30 oxide minerals in the class of spinel compounds. Their trademark is to crystallize in a cubic system to generate an octahedral crystal structure. Generally, a spinel has a chemical formula AB_2O_4 .^{12,13} Here, A represents a divalent ion of metals like iron, magnesium, nickel, or zinc. B is the trivalent metal ion of iron, aluminium, chromium, or manganese. Several different cationic combinations are possible in a spinel to match the eight anionic charges. However, the two cations should be comparable in size to stabilize the structure of oxide spinels. Therefore, spinels can be classified into aluminite (Al^{3+}), magnetite (Fe^{3+}), or chromite (Cr^{3+}) series, depending on the trivalent cation (B). Cation exchange is widespread within each series, but there is almost no exchange with the other series. Another important classification of spinels is based on their crystallographic arrangement, as described below.¹⁴

The arrangement of atoms in a crystal can be imagined to consist of a stack of unit cells called lattices. The lattice vectors, a_1 , a_2 , and a_3 define this unit cell in space. The unit cell is also expressed via k-space vectors (b_1 , b_2 , and b_3), the Fourier transform of lattice vectors. Miller

index (lmn) denotes the planes orthogonal to the k-space, and is the parameter commonly used to describe a lattice. A spinel lattice comprises at least eight AB_2O_4 molecules. The large oxygen anions form a face-centered cubic (*fcc*) arrangement. This creates two dissimilar crystallographic sites for cation occupancy, called tetrahedral (T-) having four surrounding oxygen ions and octahedral (O-) containing six oxygen ions.¹⁵ There are 64 such tetrahedral sites, and 32 octahedral sites in a spinel. Only 8 T- and 16 O- sites are occupied by the metal ions. Generally, the trivalent cations, being smaller prefer the smaller O- sites instead of the T- ones (Figure 2.3).

- In a **normal spinel** the T- sites are filled up by the divalent cations. The trivalent metal ions occupy the O- crystallographic sites. $MgAl_2O_4$ form the parent compound in this series containing $ZnAl_2O_4$, $FeAl_2O_4$, $CoAl_2O_4$, $MnAl_2O_4$, and $NiAl_2O_4$.
- An **inverse spinel** has divalent metal ions at the T- sites, but the trivalent cations are equally distributed at both T- and O- sites. Therefore, this class of spinels can be represented as $[B]^{tet} [A, B]^{oct} O_4$. The ferrites such as, $CoFe_2O_4$, $FeFe_2O_4$ (magnetite), $NiFe_2O_4$, and $MgFe_2O_4$ are the most important inverse spinels.^{16,17} Maghemite also possess an inverse spinel structure. Here, the Fe^{3+} ions are filled up at the O- sites leaving vacancies to minimize the lattice energy. In maghemite NPs smaller than 20 nm, the vacancy ordering is absent due to the small size of the particle.^{18,19}
- A **mixed spinel** is generated when the divalent and trivalent cations occupy T- and O- sites in a manner given by the formula $A_{1-\delta}^{2+}B_{\delta}^{3+}[A_{\delta}^{2+}B_{2-\delta}^{3+}]O_4^{2-}$, where δ is called the inversion factor. $MnFe_2O_4$ is a typical mixed spinel.

Most spinels, including magnetite and maghemite are ferrimagnetic.²⁰

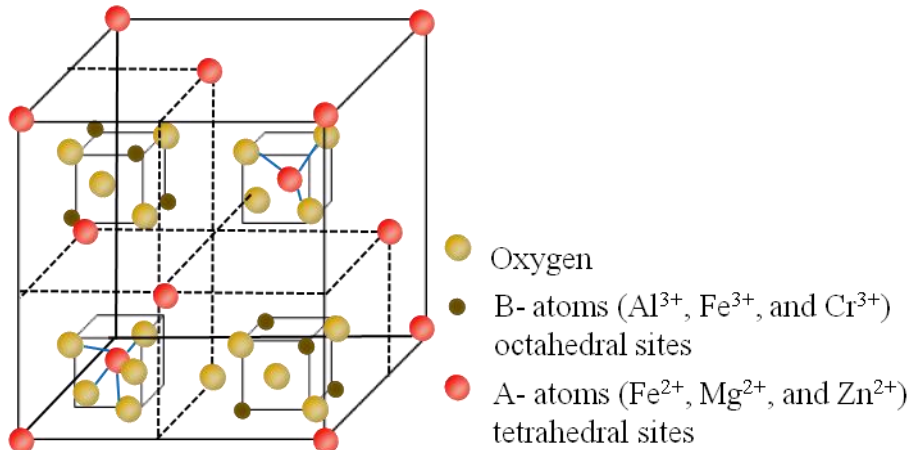


Figure 2.3. AB_2O_4 normal spinel structure.

2.2 Synthesis of Magnetic Iron Oxide Nanoparticles

2.2.1 Synthetic Approaches

The iron oxide NPs provided the platform for Pt NP attachments in our research. Therefore, synthesis of monodisperse iron oxide NPs was required. Literature review suggested both physical and chemical synthetic procedures for iron oxide NPs.^{21,22} The physical techniques such as gas phase deposition, electron beam lithography, mechanical grinding, and biomineralization lack the ability to control NP sizes. Alternatively, the wet chemical routes offer better size distribution, crystallinity, easy surface functionalization, and good scale-up.^{18,23} The reported chemical approaches for iron oxide NPs include co-precipitation, microemulsion, hydrothermal, sonochemical, electrochemical, pyrolysis, and thermal decomposition. Among these, the thermal decomposition and co-precipitation^{24,25} routes are most widely used for biomedical purposes.

Co-precipitation: The co-precipitation method is simple, cheap, and environment-friendly because only hydrophilic chemicals are used. Here, the Fe^{2+} and Fe^{3+} salts (1:2 molar ratio) are co-precipitated in an alkaline aqueous medium to form iron oxide NPs. The hydrophilic surface stabilizers are either added during or after the reaction.²⁶ This process is used in commercial

dextran-iron oxide based MRI contrast agents.²⁷ However, the iron oxide NP products obtained via co-precipitation are polydisperse, and less crystalline.

Recently, the thermal decomposition method has shown great progress (Figure 2.4).²⁸ This approach offers good control over iron oxide NP size, size distribution, yield, crystallinity, magnetic properties, and shape. Additionally, the process allows large scale synthesis of iron oxide NPs.²⁹ The two types of thermal decomposition method are elaborated as follows.

Hot-Injection: Alivisatos and co-workers first showed that “**hot-injection**” of Fe(N-nitrosophenylhydroxylamine)₃-octylamine solution into long-chain amine solvents at high temperatures (250 - 300 °C) could form maghemite NPs.³⁰ Hyeon *et. al.* extended this “hot-injection” thermal decomposition method to Fe(CO)₅ precursor with oleic acid surfactant.³¹ Here, the zerovalent iron precursor decomposed into iron NPs, prior to trimethylamine oxide induced oxidation to maghemite NPs. The process gave an improved size distribution. The NP size could also be controlled with different precursor: surfactant molar ratios.³² However, the hot injection method gave less control over the reaction parameters. For example, a seed-mediated growth was required for NP sizes above 16 nm. Additionally, the sudden burst injection could induce formation of intermediate species, and delayed nucleation.³³

Heat-Up: Therefore, Sun *et al.* introduced the second thermal decomposition approach, the “**heat-up**” method, to better control the reaction.³⁴ Here, the iron precursor, Fe(C₅H₇O₂)₃, was heated at a constant rate in phenyl ether with surfactants, hexadecanediol, oleic acid, and oleylamine. Monodisperse magnetite NPs of controllable sizes below 20 nm were synthesized in this one-pot reaction. However, the limitation of this procedure was a seed-mediated growth for larger NP sizes. Hyeon *et al.* used the “heat-up” method with an iron oleate precursor to produce large-scale monodisperse magnetite NPs of controllable size.³⁵ The advantage of the method was

the high reproducibility, one-step synthesis and use of a precursor much less toxic than Fe(CO)₅. The successful thermal decomposition technique is only limited by the organic chemicals used, and the hydrophobic nature of the NPs. To make the synthesis greener, inorganic iron salts such as, FeOOH and FeCl₃. 6H₂O were used as precursors for the thermal decomposition reactions. Additionally, the toxic organic solvents were replaced by strong polar solvents like 2-pyrrolidone,³⁶ PEG, and polyvinylpyrrolidone to synthesize water-soluble iron oxide NPs via thermal decomposition.^{37,38} However, the thermal decomposition of organometallic precursors in high boiling non-polar solvents gave better results in terms of size, size distribution, and crystallinity.³⁹

Formation of iron oxide NPs in the thermal decomposition method occurs via three stages: pre-nucleation, nucleation, and growth.⁴⁰ In the pre-nucleation stage, the precursor decomposes to produce monomers (intermediate complex) for the reaction. Supersaturated monomer concentrations cause nucleation. Nucleation can continue as long as the monomer concentration is above the critical nucleation limit. In the next step, the iron oxide nuclei grow via diffusion control⁴¹ or Ostwald-ripening,⁴² depending on the monomer availability. The nucleation and growth significantly affect iron oxide NP morphology.

Modified Heat-Up: A slightly modified “heat-up” method was used for the synthesis of iron oxide NPs in this research. Here an iron oleate precursor was heated in 1-octadecene in the presence of a weak and a strong binding ligand. This method formed iron oxide NPs of the desirable size (~ 12 nm) in a one-pot synthesis, and did not require a seed-mediated growth. Additionally, the iron oleate precursor was less toxic than Fe(CO)₅ used in other researches.

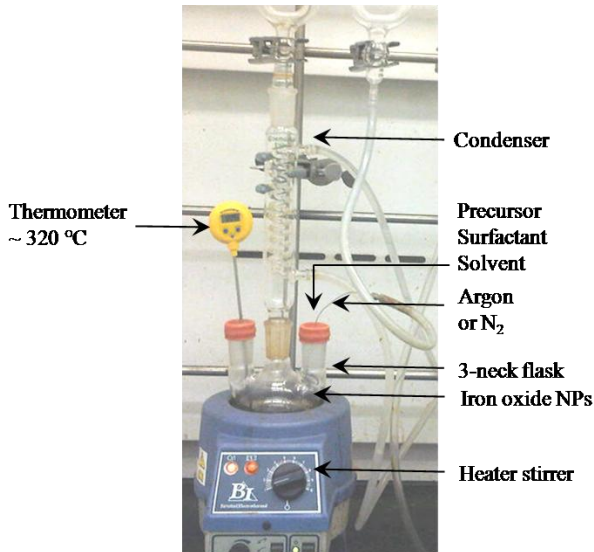


Figure 2.4. Synthesis of iron oxide NPs by thermal decomposition.

2.2.2 Shape Control of Iron Oxide Nanoparticles

Thermal decomposition method has proved promising for shape controlled synthesis of iron oxide NPs. Pure and crystalline NP shapes could be obtained using thermal decomposition, compared to the co-precipitation⁴³, hydrothermal^{44,45}, or flame reactor⁴⁶ approaches. The solvent, ligand, precursor to capping molecule molar ratio, reaction heating rate, and self-assembly of the NPs were tuned to achieve shape control in the thermal decomposition method. These approaches are elaborated as follows.

Solvent and Precursor: Recently, iron oxide NP shape control studies using thermal decomposition of fatty acid iron complexes were reported.^{47,48} Here, the higher boiling solvents were shown to induce larger sized NPs.⁴⁷ The NP formation was faster in the presence of an activating agent (alcohol or amine).⁴⁸ Additionally, ionic liquid solvents could also provide shape control. Iron oxide nanorods were synthesized via thermal decompositon of Fe(CO)₅ in ionic liquid.^{49,50} However, the above methods were limited by a wide size distribution.

Precursor: Capping Molecule Molar Ratio: Recently, Hyeon *et al.* reported a good control over the shape and size distribution of iron oxide NPs. Here, the thermal decomposition of $\text{Fe}(\text{C}_5\text{H}_7\text{O}_2)_3$ could form monodisperse, single domain iron oxide nanocubes (79 nm).⁵¹ It was concluded that a high monomer concentration induced fast growth along <111> directions in these oleic acid capped nanocubes. The nanocubes could be used in efficient separation of histidine-tagged proteins. Using a similar procedure, Guardia *et al.* could synthesize iron oxide nanocubes of tunable sizes (5-50 nm).⁵² Here, short carbon chain decanoic acid was used as the capping molecule during the thermal decomposition of $\text{Fe}(\text{C}_5\text{H}_7\text{O}_2)_3$. Decanoic acid provided a less stable system compared to oleic acid. Therefore, the nanocube morphology could be controlled by varying precursor to capping molecule ratios (p/c). At a low p/c (1:6), quasi-spherical iron oxide nanospheres formed. Intermediate shapes (between a sphere and a cube or pseudo-star-like) resulted at medium p/c (1:4 and 1:5). At higher p/c (1:3), well-defined iron oxide nanocubes were formed. This could be from faster growth of iron oxide nuclei in the presence of minimum capping molecules because the iron oxide unit cell also possesses a cubic symmetry.

Heating Rate: A similar evolution from initial spherical, to cubic, to final star-shaped NPs was observed for CoFe_2O_4 NPs.⁵³ Here, the heating rate and precursor concentration were found to be important shape control parameters.

Ligand: A popular shape control strategy in thermal decomposition is to induce crystal surface energy difference via surfactants.⁵⁴ For example, Shavel *et al.* formed iron oxide nanocubes with sodium oleate surfactant.⁵⁵ Here, the cubic morphology was facilitated by oleate anions from sodium oleate decomposition. Iron oxide nano-octahedrons were formed when surfactant, trioctylammonium bromide was used.⁵⁶ Similarly, selective binding of two capping molecules

(oleic acid and oleylamine) during thermal decomposition of $\text{Fe}(\text{C}_5\text{H}_7\text{O}_2)_3$ had induced magnetite nanocube shapes.⁵⁷ Recently, Hyeon *et al.* reported that the self-assembly of surfactant, 2,3-dihydroxy-naphthalene induced plate-like manganese oxide NPs.⁵⁸

Self-Assembly: Alternatively, self-assembly of small nanoclusters could facilitate shape anisotropy via thermal decomposition. In cobalt-ferrite NPs, periodic injection of hexane led to particle coalescence and assembly into flower-like nanostructures.⁵⁹ However, size-controlled synthesis of such nanostructures is yet to be reported for the case of iron oxide.

The above results reported few iron oxide NP shapes, mostly of cubic morphology. Other anisotropic shapes of iron oxide NPs remain unexplored. Therefore, our goal was to obtain various anisotropic iron oxide NP shapes that could facilitate Pt NP attachments.

2.3 Synthesis of Platinum Attached Iron Oxide Nanoparticles

Pt NP based heterostructures have been synthesized to potentially reduce the use of expensive Pt precursors, and stabilize the small Pt NPs. In these nanostructures, Pt NPs heterogeneously nucleated on support surfaces to reduce surface energy. Sun *et al.* followed an epitaxial growth of Fe on previously formed Pt NPs to obtain Pt-attached magnetite NPs.⁶⁰ However, this method could only form dimer NPs.⁶¹ They concluded that the electron transfer from Fe to Pt could make the Pt NP surfaces unsuitable for multiple nucleations. The possibility of multiple nucleations was investigated using Au and magnetite NPs.⁶² However, the strong interactions at the metal surfaces often detached the third NP component. Hyeon *et al.* synthesized oxide-metal heterostructures with metal-oleate and metal-oleylamine complexes to reduce the cost of the precursors.⁶³ However, this approach formed core-shell like nanostructures with less control over size and accessibility of Pt NPs.⁶⁴ Synthesis of metal oxide NPs prior to

the attachment reactions could potentially minimize the metal-metal surface interactions that inhibited multiple attachments. Hyeon *et al.* used this method for Pt NP attachment.⁶³ However, an uncontrolled reduction formed larger Pt nanoflowers in this case. Another interesting synthetic technique was to attach water soluble maghemite NPs to Pt NPs using lysine ($C_6H_{14}N_2O_2$) polymer linker.⁶⁵ However, the maghemite NPs used here showed wide size distributions. These results showed that multiple Pt NP attachments on iron oxide NP surfaces had proved challenging. Therefore, our attempt was to synthesize multiple Pt NP-attached monodisperse iron oxide NPs.

2.4 Interaction of Platinum with DNA Molecules

Recently DNA-guided synthesis and assembly of small metal NPs has been widely used. These studies reported possible NP-DNA interactions such as electrostatic attraction, hydrogen binding with DNA bases, and groove binding.⁶⁶ Cationic polymer-capped NPs showed electrostatic conjugations with negatively charged phosphate groups in the DNA backbone.^{67,68} However, tris(hydroxymethyl)phosphine coated anionic Au NPs could also bind to the DNA. A hydrogen bond formation with DNA bases was proposed to explain this result. The Au NPs showed strong binding affinity for nucleosides guanine (N1), adenine (N7), and cytosine (N3), compared to thymine.^{69,70} Such nucleobase binding was also observed for Pt NPs in interactions with peptide nucleic acids.⁷¹ Generally, Pt metal ions show a high affinity for DNA bases.⁷² A strong interaction with all DNA bases was recently reported for Au and Pt NPs.⁷³ The interaction was less strong for larger NPs. Affinity of DNA nitrogen bases for small metal NPs (< 5 nm) had resulted in hydrogen bond breaks between dissimilar bases.⁷⁴ This showed that the small NPs could induce DNA destruction via double strand dissociations. Recently, DNA groove binding

was also shown by Au nanoclusters (1.4 nm). Here, the Au NPs inside DNA grooves could shrink the groove size via interaction with phosphate and oxygen atoms.⁷⁵ These different NP-DNA conjugations could be efficiently detected using gel electrophoresis.⁷⁶ For example, Pt NP-DNA conjugation has been successfully investigated through electrophoresis.⁷⁷ These studies showed the probable DNA-NP interactions. However, most DNA interaction researches were focused on Au NPs.

Recently, small Pt NPs have been used in many promising therapeutic applications, such as DNA degradation, radiation therapy enhancement, and treatment of oxidative stress disease, as explained earlier. Therefore, the aim of this research was to investigate the DNA interaction ability of the Pt NPs supported on iron oxide NPs.

2.5 Characterization of Nanoparticles

Good characterization techniques are required to investigate NP properties such as DNA interaction, size, morphology, crystal structure, and magnetic behavior. NP characterization is important because human eye cannot resolve such small structures.

A transmission electron microscope (TEM) is used to determine the size, morphology, and qualitative chemical composition of the NPs.⁷⁸ The NP sample, dispersed in a volatile solvent (*e.g.*, hexane) is dropped on carbon-coated copper grids (3 mm) for viewing on the TEM.⁷⁹ In a TEM, an electron beam interacts with the specimen loaded on the TEM holder. The interacted beam contains specimen information that can be displayed through a charge coupled device camera or film negative. Bright field imaging (BF) is used for size and shape overview of the entire NP sample. The transmitted electron beam from the sample is the main contributor of this image. Here, the NPs appear as dark spots on a bright background. However, only high-

resolution transmission electron microscopy (HRTEM) can image NPs at the atomic resolution to show crystallographic planes (lattice fringes). Here, strongly diffracted electrons from the sample interfere with the transmitted electrons to give phase contrast. The TEM lenses must be properly aligned, and the objective stigmation adjusted for such high magnifications. The crystal phase of the sample can be determined using TEM electron diffraction (ED) patterns. Single-crystalline NP samples show well defined points in ED, compared to concentric rings and diffused concentric rings for polycrystalline and amorphous NPs, respectively. However, a high-angle annular dark field (HAADF) is required to detect very small NPs (< 5 nm). The HAADF operates at very high angles to detect slow secondary electrons that escaped from the sample. Therefore, the HAADF image is negligibly affected by defocus and sample thickness (Bragg's reflections), compared to BF images. The TEM also gives a rough chemical composition of the NP sample via energy-dispersive-spectrophotometry (EDS). The EDS plots the characteristic x-ray count versus x-ray energy to show sample chemical composition. In this research, a FEI Tecnai F-20 TEM operating at 200 keV was used for NP characterization. A JEOL-7000 scanning electron microscope (SEM) was also used in some cases for supporting data. SEM scans an electron beam across the entire sample, unlike the converged electron beam used in TEM. The signal created from electron-sample interaction gives the image in SEM.

X-ray diffraction (XRD) gives crystallographic information of the NPs. Here, the organic surface coating of the NPs is washed completely to form a well-dried NP sample. The collimated incident x-rays ($\sim 1 \text{ \AA}$) are scattered by the powdered NP sample.⁸⁰ The elastically scattered or Bragg diffracted x-rays are measured in the detector.⁸¹ The sample and the detector are rotated at θ and 2θ respectively to obtain diffraction data of the entire sample. A 2θ scan from 20° - 80° can identify the NP crystal phase, based on the reference data (International Center Diffraction Data,

ICDD).⁸² Here, a Bruker AXS D8 Advanced XRD was used to investigate the crystal phase of iron oxide NPs.

X-ray photoelectron spectroscopy (XPS) can be used to distinguish iron oxide NP crystal phases, $\gamma\text{-Fe}_2\text{O}_3$ and Fe_3O_4 . The XPS gives surface chemical composition (100 atom%- 0.1 atom% concentration) of the powdered NP sample within a 1-10 nm surface range.^{83,84} Here, the emitted photoelectron count is reported for corresponding binding energies. The peaks in the survey scan (0~1100 eV, 1 eV/point) spectrum indicate the presence of specific elements on the surface of the sample. A high resolution multiplex scan (20 eV window, 0.065 eV/point) gives a closer view into spin-orbit coupling and oxidation states of the surface elements. Atoms at a higher oxidation state show increased binding energies due to the extra Coulombic interaction of the photo-emitted electron with the nucleus. The XPS can also gradually remove the sample surface via ion sputtering to report elemental composition as a function of depth from the sample surface. A Kratos AXIS 165 Multitechnique Electron Spectrometer was used in this research.

The metal ion concentrations in NP solution can be measured using atomic absorption spectroscopy (AAS). The AAS can determine metal concentration from ultra trace to major constituent level in a wide variety of sample type including nanomaterials. All analytes are transferred to homogeneous solutions before analysis. AAS measures the decrease in light intensity from a source (hollow cathode lamp or electrode less discharge lamp) when it passes through a vapor layer of analyte element atoms.^{85,86} The ground state atom absorbs light energy of a specific wavelength as it enters the „excited state“. As the number of atoms in the light path increases, the amount of light absorbed also increases. A quantitative determination of the amount of the analyte can be made by measuring the „light absorbed“. Quantitative measurements in atomic absorption are based on Beer’s law (the concentration is proportional to

absorbance, $C = KA$). In an AAS, a light source emits the spectrum of the element of interest (*e.g.*, Pt, Fe hollow cathode lamps). The absorption cell or nebulizer-burner system produces the sample atoms using the air-acetylene flame. Here, the flame temperature should be more than 2100 °C. The monochromator controls the light dispersion. The AAS detector measures the light intensity, and amplifies the signal, prior to display. We used a Spectra 220 FS (Varian) AAS to detect ions of Pt and Fe in our NP samples. Specific wavelengths are recommended for Fe ions (248.3 nm), and Pt ions (265.9 nm). An air: acetylene flame is recommended for both Fe and Pt metal determination. AAS is a very specific technique, but contains some chemical and spectral interferences. Addition of 0.2% La in 1% HCl is necessary to eliminate other metal (Fe in this case) interferences for Pt ions. Interferences for Fe ions can be controlled by using a very lean flame.

Fourier transform infrared spectroscopy (FTIR) can analyze the chemical bonds and functional groups in the NP sample.⁸⁷ In FTIR, the incident infrared (IR) beam is first resolved into its individual frequency components via an interferometer. The resolved beam induces vibrational excitations in atoms of the sample.⁸⁸ Vibrations in the sample molecule causes symmetric or asymmetric changes in the inter-atomic distance along the bond axis (stretching), or changes in the bond angle (bending). Stretching induces higher vibrational frequencies than bending. The vibrational frequency increases with bond energy and atomic weight. The detector measures the IR signal after interaction with the sample. A Fourier transform or recombination of this signal gives the final IR spectrum in terms of transmission (or absorption). The spectrum shows the characteristic vibrational frequencies of the sample. Single bonds show peaks in the range of 3300 –2800 cm⁻¹. The double bond regime is 1750 -1500 cm⁻¹, and triple bonds fall within 2300 -2100 cm⁻¹. The fingerprint region of 1500 to 600 cm⁻¹ contains peaks characteristic

to the particular sample. The closely spaced peaks in this region are difficult to identify, but each compound gives a different peak pattern. This suggests the chemical composition of the NP. Additionally, the surface functional groups detected provides information about NP-ligand surface interactions. A PerkinElmer Spectrum 100 FT-IR spectrometer (Bucks, UK) was used in this study.

Raman spectroscopy gives a cleaner spectrum than the FTIR, and interferences from water and CO₂ are negligible. A monochromatic beam of photons from the laser source induces the weak Raman scattering in the NP sample (powder). Filters, diffraction gratings, and sensitive detectors used collect only the Raman scatterings. Finally, the Raman spectrum is plotted with respect to the laser frequency. A Raman spectrum shows sharp bands, detectable even below 400 cm⁻¹, and strong peaks for symmetric molecular stretches. A Bruker Senterra system (Bruker Optics Inc. Woodlands, TX) was used to analyze our NPs.

Thermogravimetric analysis (TGA) is useful for determining the surface coating of NPs.⁸⁹ In TGA, the powdered NP sample is heated at controlled temperatures less than 1000 °C to monitor the weight loss as a function of temperature and time.⁹⁰ A precision balance supports the sample pan inside the furnace. The balance records the loss or gain in weight of the sample, during controlled heating experiments. An inert or reactive purge gas flows over the sample to control the sample environment. The TGA provides quantitative measures of mass changes related to dissociation of bonds, oxidation, surfactant layer,⁹¹ or decomposition of the NP sample.^{92,53} It can also be used to estimate the volatile content in the sample. A quartz crystal microbalance also operates on the principles of TGA, but requires less sample (μg instead of a few mg). This is especially favorable for NP samples that are difficult to precipitate.⁹³ Our experiments were performed on a TA Instruments TGA 2950 thermogravimetric analyzer (New Castle, DE).

Dynamic light scattering (DLS) is widely used to measure the hydrodynamic diameter and surface charge of NPs. This technique is rapid and non-destructive. Here, light from a laser source is first incident on the NP solution. Random Brownian motions of the sample solution scatter the incident light. The diffusion rate of the NP molecules in solution controls the time-dependent fluctuations of scattered light. This diffusion rate is related to the hydrodynamic diameter of the NP. Therefore, the DLS can report the NP properties (hydrodynamic diameter, surface charge) from the detected light scatter.⁹⁴ The scattered light also shows randomness in phase, and can interfere constructively or destructively. A Zetasizer Nano (Malvern) DLS was used for this research.

An alternating gradient field magnetometer (AGM) allows fast magnetic measurement on powdered NP samples. A measured weight of the sample is mounted on a quartz extension rod. A large electromagnet is used to produce external magnetic field up to 15 kOe. Additionally, two small electromagnets generate an alternating magnetic field in the air gap across the sample. The alternating field exerts an oscillatory force proportional to the magnetic moment of the sample.^{95,96} This force causes the sample to deflect. A piezoelectric sensor detects the deflection, and generates a proportional voltage signal. The magnetic moment of the sample is reported as a function of the applied field using the voltage signal, and the alternating field gradient. The corresponding magnetizations can be calculated from the known sample weight. The AGM has a high sensitivity ($\sim 10^6$ emu), and is suitable even for less magnetic NP samples. A Princeton alternating gradient field magnetometer was used in our studies.

The NP-DNA interaction can be best measured using agarose gel electrophoresis.^{76,97} Here, the samples migrate through the pores in the gel under an electric field gradient. The gel is prepared by completely dissolving the agarose (GTG) in tris-acetate-ethylenediaminetetraacetate

(TAE) buffer solution via microwave (General Electric). The homogeneous solution is poured in the gel tray to solidify. The weight of agarose per volume of the buffer solution controls the pore size of the gel. In a uniform gel, the samples show different migration rates depending on their charge and molecular weight.⁹⁸ Negatively-charged DNA migrates towards the anode (positive charge). DNA interactions can be investigated from the different sample migrations. A Thermo Scientific agarose gel equipment was used for this research.

In summary, the recent researches and characterization techniques required for the experiments in this project were introduced in this chapter. The magnetic properties, spinel structure, and synthetic approaches were explained to better understand the properties and formation mechanism of iron oxide NPs used in this research. Here, the iron oxide NP surfaces formed the platform for attachment of multiple small Pt NPs. Therefore, recent reports of Pt NP attachments on iron oxide NPs were discussed. These methods were limited by a less controlled and a single Pt NP attachment. The goal of this research is to synthesize multiple Pt NP attached iron oxide NPs, and to show the NP-DNA interaction. Recently the free Pt NPs showed interesting DNA interactions that were described in this chapter. The hypothesis of this project was that the Pt NPs attached to the iron oxide surfaces will interact with the DNA like the free Pt NPs. The experiments designed and the results obtained to prove this hypothesis are detailed in the following section.

References

1. Spaldin, N., *Magnetic materials: fundamentals and device applications*. Cambridge University Press: Cambridge, 2003.
2. O' Handley, R., *Modern magnetic materials: principles and applications*. John Wiley & Sons Inc.: New York, 2000.
3. Sundaresan, A.; Rao, C. N. R., Ferromagnetism as a universal feature of inorganic nanoparticles. *Nano Today* **2009**, *4* (1), 96-106.
4. Gilleo, M., Superexchange interaction in ferrimagnetic garnets and spinels which contain randomly incomplete linkages. *Journal of Physics and Chemistry of Solids* **1960**, *13*, 33-39.
5. Laurent, S.; Forge, D.; Port, M.; Roch, A.; Robic, C.; Elst, L. V.; Muller, R. N., Magnetic iron oxide nanoparticles: synthesis, stabilization, vectorization, physicochemical characterizations, and biological applications. *Chemical Reviews* **2008**, *108* (6), 2064-2110.
6. Figuerola, A.; Di Corato, R.; Manna, L.; Pellegrino, T., From iron oxide nanoparticles towards advanced iron-based inorganic materials designed for biomedical applications. *Pharmacological Research* **2010**, *62* (2), 126-143.
7. Krishnan, K. M.; Pakhomov, A. B.; Bao, Y.; Blomqvist, P.; Chun, Y.; Gonzales, M.; Griffin, K.; Ji, X.; Roberts, B. K., Nanomagnetism and spin electronics: materials, microstructure and novel properties. *Journal of Materials Science* **2006**, *41*, 793-815.
8. Xie, J.; Huang, J.; Li, X.; Sun, S.; Chen, X., Iron oxide nanoparticle platform for biomedical applications. *Current Medicinal Chemistry* **2009**, *16* (10), 1278-1294.
9. Gangopadhyay, S.; Hadjipanayis, G. C.; Dale, B.; Sorensen, C. M.; Klabunde, K. J.; Papaefthymiou, V.; Kostikas, A., Magnetic-properties of ultrafine iron particles. *Physical Review B* **1992**, *45* (17), 9778-9787.

10. Chatterjee, J.; Haik, Y.; Chen, C. J., Size dependent magnetic properties of iron oxide nanoparticles. *Journal of Magnetism and Magnetic Materials* **2003**, 257 (1), 113-118.
11. Vollath, D.; Szabo, D. V.; Taylor, R. D.; Willis, J. O., Synthesis and magnetic properties of nanostructured maghemite. *Journal of Materials Research* **1997**, 12 (8), 2175-2182.
12. Siddiquah, M. Effect of doping of various metal cations on structural, electrical and magnetic properties of nano cobalt ferrites. Quaid-I-Azam-University, Islamabad, 2008.
13. Adams, D., *Inorganic Solids*. John Wiley: London, 1974.
14. Vestal, C. R.; Zhang, Z. J., Magnetic spinel ferrite nanoparticles from microemulsions. *International Journal of Nanotechnology* **2004**, 1 (1-2), 240-263.
15. Mathew, D. S.; Juang, R.-S., An overview of the structure and magnetism of spinel ferrite nanoparticles and their synthesis in microemulsions. *Chemical Engineering Journal* **2007**, 129 (1-3), 51-65.
16. Deguire, M. R.; Ohandley, R. C.; Kalonji, G., The cooling rate dependence of cation distributions in CoFe₂O₄. *Journal of Applied Physics* **1989**, 65 (8), 3167-3172.
17. King, R., Minerals explained 40: The spinels. *Geology Today* **2004**, 20, 194-200.
18. Teja, A. S.; Koh, P.-Y., Synthesis, properties, and applications of magnetic iron oxide nanoparticles. *Progress in Crystal Growth and Characterization of Materials* **2009**, 55 (1-2), 22-45.
19. Smyth, D., *The Defect Chemistry of Metal Oxides*. Oxford University Press: New York, 2000.
20. Smith, J.; Wijn, H., *Ferrites-Physical Properties of Ferrimagnetic Oxides in Relation to their Technical Applications*. John Wiley and Sons: Netherlands, 1959.

21. Lu, A.-H.; Salabas, E. L.; Schueth, F., Magnetic nanoparticles: synthesis, protection, functionalization, and application. *Angewandte Chemie-International Edition* **2007**, *46* (8), 1222-1244.
22. Gubin, S. P.; Koksharov, Y. A.; Khomutov, G. B.; Yurkov, G. Y., Magnetic nanoparticles: preparation methods, structure and properties. *Uspekhi Khimii* **2005**, *74* (6), 539-574.
23. McBain, S. C.; Yiu, H. H. P.; Dobson, J., Magnetic nanoparticles for gene and drug delivery. *International Journal of Nanomedicine* **2008**, *3* (2), 169-180.
24. Elmore, W., Ferromagnetic colloid for studying magnetic structures. *Physical Review* **1938**, *54*, 309.
25. Ricketts, C.; Cox, J.; Fitzmaur, C.; Moss, G., The iron dextran complex. *Nature* **1965**, *208*, 237.
26. Gupta, A. K.; Gupta, M., Synthesis and surface engineering of iron oxide nanoparticles for biomedical applications. *Biomaterials* **2005**, *26* (18), 3995-4021.
27. Bautista, M. C.; Bomati-Miguel, O.; Morales, M. D.; Serna, C. J.; Veintemillas-Verdaguer, S., Surface characterisation of dextran-coated iron oxide nanoparticles prepared by laser pyrolysis and coprecipitation. *Journal of Magnetism and Magnetic Materials* **2005**, *293* (1), 20-27.
28. Hyeon, T., Chemical synthesis of magnetic nanoparticles. *Chemical Communications* **2003**, (8), 927-934.
29. Park, J.; An, K. J.; Hwang, Y. S.; Park, J. G.; Noh, H. J.; Kim, J. Y.; Park, J. H.; Hwang, N. M.; Hyeon, T., Ultra-large-scale syntheses of monodisperse nanocrystals. *Nature Materials* **2004**, *3* (12), 891-895.

30. Rockenberger, J.; Scher, E. C.; Alivisatos, A. P., A new nonhydrolytic single-precursor approach to surfactant-capped nanocrystals of transition metal oxides. *Journal of the American Chemical Society* **1999**, *121* (49), 11595-11596.
31. Hyeon, T.; Lee, S. S.; Park, J.; Chung, Y.; Bin Na, H., Synthesis of highly crystalline and monodisperse maghemite nanocrystallites without a size-selection process. *Journal of the American Chemical Society* **2001**, *123* (51), 12798-12801.
32. Woo, K.; Hong, J.; Choi, S.; Lee, H. W.; Ahn, J. P.; Kim, C. S.; Lee, S. W., Easy synthesis and magnetic properties of iron oxide nanoparticles. *Chemistry of Materials* **2004**, *16* (14), 2814-2818.
33. Casula, M. F.; Jun, Y. W.; Zaziski, D. J.; Chan, E. M.; Corrias, A.; Alivisatos, A. P., The concept of delayed nucleation in nanocrystal growth demonstrated for the case of iron oxide nanodisks. *Journal of the American Chemical Society* **2006**, *128* (5), 1675-1682.
34. Sun, S. H.; Zeng, H., Size-controlled synthesis of magnetite nanoparticles. *Journal of the American Chemical Society* **2002**, *124* (28), 8204-8205.
35. Park, J.; An, K.; Hwang, Y.; Park, J.-G.; Noh, H.-J.; Kim, J.-Y.; Park, J.-H.; Hwang, N.-M.; Hyeon, T., Ultra-large-scale syntheses of monodisperse nanocrystals. *Nature Materials* **2004**, *3* (12), 891 - 895.
36. Qiao, R. R.; Yang, C. H.; Gao, M. Y., Superparamagnetic iron oxide nanoparticles: from preparations to *in vivo* MRI applications. *Journal of Materials Chemistry* **2009**, *19* (48), 6274-6293.
37. Li, Z.; Wei, L.; Gao, M. Y.; Lei, H., One-pot reaction to synthesize biocompatible magnetite nanoparticles. *Advanced Materials* **2005**, *17* (8), 1001-1002.

38. Hu, F.; Wei, L.; Zhou, Z.; Ran, Y.; Li, Z.; Gao, M., Preparation of biocompatible magnetite nanocrystals for in vivo magnetic resonance detection of cancer. *Advanced Materials* **2006**, *18* (19), 2553-2554.
39. Roca, A. G.; Morales, M. P.; Serna, C. J., Synthesis of monodispersed magnetite particles from different organometallic precursors. *IEEE Transactions on Magnetics* **2006**, *42* (10), 3025-3029.
40. Kwon, S. G.; Piao, Y.; Park, J.; Angappane, S.; Jo, Y.; Hwang, N. M.; Park, J. G.; Hyeon, T., Kinetics of monodisperse iron oxide nanocrystal formation by "heating-up" process. *Journal of the American Chemical Society* **2007**, *129* (41), 12571-12584.
41. Reiss, H., The growth of uniform colloidal dispersions. *Journal of Chemical Physics* **1951**, *19*, 482-487.
42. Cheon, J. W.; Kang, N. J.; Lee, S. M.; Lee, J. H.; Yoon, J. H.; Oh, S. J., Shape evolution of single-crystalline iron oxide nanocrystals. *Journal of the American Chemical Society* **2004**, *126* (7), 1950-1951.
43. Ruoslahti, E.; Bhatia, S. N.; Sailor, M. J., Targeting of drugs and nanoparticles to tumors. *Journal of Cell Biology* **2010**, *188* (6), 759-768.
44. Piao, Y.; Kim, J.; Bin Na, H.; Kim, D.; Baek, J. S.; Ko, M. K.; Lee, J. H.; Shokouhimehr, M.; Hyeon, T., Wrap-bake-peel process for nanostructural transformation from beta-FeOOH nanorods to biocompatible iron oxide nanocapsules. *Nature Materials* **2008**, *7* (3), 242-247.
45. Guo, X.; Zhong, S.; Zhang, J.; Wang, W.; Mao, J.; Xie, G., Synthesis, phase transition, and magnetic property of iron oxide materials: effect of sodium hydroxide concentrations. *Journal of Materials Science* **2010**, *45* (23), 6467-6473.

46. Xing, Y. C.; Kole, T. P.; Katz, J. L., Shape-controlled synthesis of iron oxide nanoparticles. *Journal of Materials Science Letters* **2003**, *22* (11), 787-790.
47. Chen, C. J.; Lai, H. Y.; Lin, C. C.; Wang, J. S.; Chiang, R. K., Preparation of monodisperse iron oxide nanoparticles via the synthesis and decomposition of iron fatty acid complexes. *Nanoscale Research Letters* **2009**, *4* (11), 1343-1350.
48. Jana, N. R.; Chen, Y. F.; Peng, X. G., Size- and shape-controlled magnetic (Cr, Mn, Fe, Co, Ni) oxide nanocrystals via a simple and general approach. *Chemistry of Materials* **2004**, *16* (20), 3931-3935.
49. Wang, Y.; Yang, H., Synthesis of iron oxide nanorods and nanocubes in an imidazolium ionic liquid. *Chemical Engineering Journal* **2009**, *147* (1), 71-78.
50. Lee, C. M.; Jeong, H. J.; Lim, S. T.; Sohn, M. H.; Kim, D. W., Synthesis of Iron Oxide Nanoparticles with Control over Shape Using Imidazolium-Based Ionic Liquids. *ACS Applied Materials & Interfaces* **2010**, *2* (3), 756-759.
51. Kim, D.; Lee, N.; Park, M.; Kim, B. H.; An, K.; Hyeon, T., Synthesis of uniform ferrimagnetic magnetite nanocubes. *Journal of the American Chemical Society* **2009**, *131* (2), 454-455.
52. Guardia, P.; Perez, N.; Labarta, A.; Batlle, X., Controlled synthesis of iron oxide nanoparticles over a wide size range. *Langmuir* **2010**, *26* (8), 5843-5847.
53. Bao, N. Z.; Shen, L. M.; An, W.; Padhan, P.; Turner, C. H.; Gupta, A., Formation mechanism and shape control of monodisperse magnetic CoFe_2O_4 nanocrystals. *Chemistry of Materials* **2009**, *21* (14), 3458-3468.
54. Yin, Y.; Alivisatos, A. P., Colloidal nanocrystal synthesis and the organic-inorganic interface. *Nature* **2005**, *437* (7059), 664-670.

55. Shavel, A.; Liz-Marzan, L. M., Shape control of iron oxide nanoparticles. *Physical Chemistry Chemical Physics* **2009**, *11* (19), 3762-3766.
56. Shavel, A.; Rodriguez-Gonzalez, B.; Pacifico, J.; Spasova, M.; Farle, M.; Liz-Marzan, L. M., Shape control in iron oxide nanocrystal synthesis, induced by trioctylammonium ions. *Chemistry of Materials* **2009**, *21* (7), 1326-1332.
57. Yang, H. T.; Ogawa, T.; Hasegawa, D.; Takahashi, M., Synthesis and magnetic properties of monodisperse magnetite nanocubes. *Journal of Applied Physics* **2008**, *103* (7).
58. Park, M.; Lee, N.; Choi, S. H.; An, K.; Yu, S.-H.; Kim, J. H.; Kwon, S.-H.; Kim, D.; Kim, H.; Baek, S.-I.; Ahn, T.-Y.; Park, O. K.; Son, J. S.; Sung, Y.-E.; Kim, Y.-W.; Wang, Z.; Pinna, N.; Hyeon, T., Large-scale synthesis of ultrathin manganese oxide nanoplates and their applications to T1 MRI contrast agents. *Chemistry of Materials* **2011**, *23* (14), 3318-3324.
59. Bao, N. Z.; Shen, L. M.; Wang, Y. H. A.; Ma, J. X.; Mazumdar, D.; Gupta, A., Controlled growth of monodisperse self-supported superparamagnetic nanostructures of spherical and rod-like CoFe₂O₄ nanocrystals. *Journal of the American Chemical Society* **2009**, *131* (36), 12900-12901.
60. Wang, C.; Daimon, H.; Sun, S. H., Dumbbell-like Pt-Fe₃O₄ nanoparticles and their enhanced catalysis for oxygen reduction reaction. *Nano Letters* **2009**, *9* (4), 1493-1496.
61. Wang, C.; Xu, C. J.; Zeng, H.; Sun, S. H., Recent progress in syntheses and applications of dumbbell-like nanoparticles. *Advanced Materials* **2009**, *21* (30), 3045-3052.
62. Wang, C.; Wei, Y.; Jiang, H.; Sun, S., Tug-of-war in nanoparticles: competitive growth of Au on Au-Fe(3)O(4) nanoparticles. *Nano Letters* **2009**, *9* (12), 4544-4547.
63. Choi, S. H.; Bin Na, H.; Park, Y. I.; An, K.; Kwon, S. G.; Jang, Y.; Park, M.; Moon, J.; Son, J. S.; Song, I. C.; Moon, W. K.; Hyeon, T., Simple and generalized synthesis of oxide-metal

heterostructured nanoparticles and their applications in multimodal biomedical probes. *Journal of the American Chemical Society* **2008**, *130* (46), 15573-15580.

64. Teng, X. W.; Black, D.; Watkins, N. J.; Gao, Y. L.; Yang, H., Platinum-maghemite core-shell nanoparticles using a sequential synthesis. *Nano Letters* **2003**, *3* (2), 261-264.
65. Zhang, J.; Liu, X.; Guo, X.; Wu, S.; Wang, S., A general approach to fabricate diverse noble-metal (Au, Pt, Ag, Pt/Au)/Fe(2)O(3) hybrid nanomaterials. *Chemistry-A European Journal* **2010**, *16* (27), 8108-8116.
66. De, M.; Ghosh, P. S.; Rotello, V. M., Applications of nanoparticles in biology. *Advanced Materials* **2008**, *20* (22), 4225-4241.
67. You, C. C.; Verma, A.; Rotello, V. M., Engineering the nanoparticle-biomacromolecule interface. *Soft Matter* **2006**, *2* (3), 190-204.
68. He, X. X.; Wang, K. M.; Tan, W. H.; Liu, B.; Lin, X.; He, C. M.; Li, D.; Huang, S. S.; Li, J., Bioconjugated nanoparticles for DNA protection from cleavage. *Journal of the American Chemical Society* **2003**, *125* (24), 7168-7169.
69. Storhoff, J. J.; Elghanian, R.; Mirkin, C. A.; Letsinger, R. L., Sequence-dependent stability of DNA-modified gold nanoparticles. *Langmuir* **2002**, *18* (17), 6666-6670.
70. Jang, N. H., The coordination chemistry of DNA nucleosides on gold nanoparticles as a probe by SERS. *Bulletin of the Korean Chemical Society* **2002**, *23* (12), 1790-1800.
71. Wang, X.; Pandey, R. R.; Singh, K. V.; Andavan, G. T. S.; Tsai, C.; Lake, R.; Ozkan, M.; Ozkan, C. S., Synthesis and characterization of peptide nucleic acid-platinum nanoclusters. *Nanotechnology* **2006**, *17* (5), 1177-1183.
72. Berti, L.; Burley, G. A., Nucleic acid and nucleotide-mediated synthesis of inorganic nanoparticles. *Nature Nanotechnology* **2008**, *3* (2), 81-87.

73. Yang, J.; Lee, J. Y.; Too, H. P.; Chow, G. M., Inhibition of DNA hybridization by small metal nanoparticles. *Biophysical Chemistry* **2006**, *120* (2), 87-95.
74. Yang, J.; Pong, B.-K.; Lee, J. Y.; Too, H.-P., Dissociation of double-stranded DNA by small metal nanoparticles. *Journal of Inorganic Biochemistry* **2007**, *101* (5), 824-830.
75. Liu, Y. P.; Meyer-Zaika, W.; Franzka, S.; Schmid, G.; Tsoli, M.; Kuhn, H., Gold-cluster degradation by the transition of B-DNA into A-DNA and the formation of nanowires. *Angewandte Chemie-International Edition* **2003**, *42* (25), 2853-2857.
76. Zanchet, D.; Micheel, C. M.; Parak, W. J.; Gerion, D.; Alivisatos, A. P., Electrophoretic isolation of discrete Au nanocrystal/DNA conjugates. *Nano Letters* **2001**, *1* (1), 32-35.
77. Li, Y.; Zheng, Y.; Gong, M.; Deng, Z., Pt nanoparticles decorated with a discrete number of DNA molecules for programmable assembly of Au-Pt bimetallic superstructures. *Chemical Communications* **2012**, *48* (31), 3727-3729.
78. Williams, D. B.; Carter, C. B., *Transmission electron microscopy*. Plenum Press: New York and London, Vol. 3 1996.
79. Wang, Z., In *Characterization of nanophase materials*, Wiley VCH Verlag GmbH: Weinheim, 2000.
80. Klug, H.; Alexander, L., *X-ray diffraction procedures*. 2 ed.; J. Wiley & Sons Inc.: New York, 1996.
81. Kittel, C., *Introduction to solid state physics*. 6 ed.; Wiley: New York, 1985.
82. Cullity, B.; Stock, S., *Elements of x-ray diffraction*. 2 ed.; Prentice Hall: New Jersey, 2001.

83. Baer, D. R.; Gaspar, D. J.; Nachimuthu, P.; Techane, S. D.; Castner, D. G., Application of surface chemical analysis tools for characterization of nanoparticles. *Analytical and Bioanalytical Chemistry* **2010**, 396 (3), 983-1002.
84. Katari, J. E. B.; Colvin, V. L.; Alivisatos, A. P., X-ray photoelectron-spectroscopy of cdse nanocrystals with applications to studies of the nanocrystal surface. *Journal of Physical Chemistry* **1994**, 98 (15), 4109-4117.
85. Mendham, J.; Denney, R. C.; Barnes, J. D.; Thomas, M. J. K., *Vogel's text book of quantitative chemical analysis*. 6 ed.; Pearson Education: India, 2002.
86. *Atomic absorption spectroscopy, analytical methods*. Perkin Elmer Corporation: USA, 1996.
87. Bronstein, L. M.; Huang, X.; Retrum, J.; Schmucker, A.; Pink, M.; Stein, B.; Dragnea, B., Influence of iron oleate complex structure on iron oxide nanoparticle formation. *Chemistry of Materials* **2007**, 19 (15), 3624-3632.
88. Sherman, C., Infrared Spectroscopy. In *Handbook of instrumental techniques for analytical chemistry*, Settle, F., Ed. Prentice Hall: New Jersey, 1997.
89. White, B.; Yin, M.; Hall, A.; Le, D.; Stolbov, S.; Rahman, T.; Turro, N.; O'Brien, S., Complete CO oxidation over Cu₂O nanoparticles supported on silica gel. *Nano Letters* **2006**, 6 (9), 2095-2098.
90. Brown, M., *Introduction to thermal analysis: techniques and applications*. Chapman and Hall: London, New York, 1988.
91. Sahoo, Y.; Goodarzi, A.; Swihart, M. T.; Ohulchanskyy, T. Y.; Kaur, N.; Furlani, E. P.; Prasad, P. N., Aqueous ferrofluid of magnetite nanoparticles: fluorescence labeling and magnetophoretic control. *Journal of Physical Chemistry B* **2005**, 109 (9), 3879-3885.

92. Wu, X. W.; Liu, C.; Li, L.; Jones, P.; Chantrell, R. W.; Weller, D., Nonmagnetic shell in surfactant-coated FePt nanoparticles. *Journal of Applied Physics* **2004**, 95 (11), 6810-6812.
93. Mansfield, E.; Kar, A.; Quinn, T. P.; Hooker, S. A., Quartz crystal microbalances for microscale thermogravimetric analysis. *Analytical Chemistry* **2010**, 82 (24), 9977-9982.
94. Tscharnuter, W., *Photon correlation spectroscopy in particle sizing (Encyclopedia of Analytical Chemistry)*. John Wiley & Sons Ltd.: Chichester, 2000.
95. Flanders, P. J., An alternating-gradient magnetometer. *Journal of Applied Physics* **1988**, 63 (8), 3940-3945.
96. Harrell, J. W., Effect of AC gradient field on magnetic measurements with an alternating gradient magnetometer. *Journal of Magnetism and Magnetic Materials* **1999**, 205 (1), 121-129.
97. Tabassum, S.; Sharma, G. C.; Arjmand, F.; Azam, A., DNA interaction studies of new nano metal based anticancer agent: validation by spectroscopic methods. *Nanotechnology* **2010**, 21 (19), 195102 (1-10).
98. Bier, M., *Electrophoresis: theory, methods, and applications*. Academic Press: New York, 1959.

CHAPTER 3

EXPERIMENTS, RESULTS, AND DISCUSSION

The goal of this research was to prove the effective DNA interaction of the Pt NPs supported on iron oxide carriers. The specific research tasks to achieve this goal involved reproducible synthesis of the iron oxide NPs, attachment of Pt NPs to the iron oxide seeds, an aqueous phase transfer of the NPs, and DNA interaction of the Pt-iron oxide NPs. This chapter will elaborate each of these methods. The first section describes the synthesis of monodisperse iron oxide nanospheres (Section 3.1). Subsequently, the Pt NPs were attached to the iron oxide seeds via an organic route (Section 3.2). Interestingly, modifying the shape of the iron oxide NPs facilitated Pt NP attachments in an organic solvent (Section 3.3). Here, iron oxide nanowhiskers (Section 3.3.1), nanoworms (Section 3.3.2), nanoplates, and nanoflowers (Section 3.3.3) were reproducibly synthesized. The NPs in organic solution were made biocompatible via an aqueous phase transfer using ligand exchange (Section 3.4). Subsequently, the water-soluble iron oxide NPs were used for Pt NP attachments via an aqueous route (Section 3.5). This facile approach provided better accessibility of the Pt NPs for the DNA interactions. Therefore, this integrated NP was used as a model for the proof-of-concept DNA interaction experiments (Section 3.6).

3.1 Iron Oxide Nanospheres

The hypothesis of this research was that the small Pt NPs attached to iron oxide NP carriers will interact with the DNA like the free Pt NPs. The iron oxide NPs will provide stability to small Pt NPs, and could potentially act as MRI contrast agents. Multiple Pt NP- attached iron

oxide NPs were first synthesized to prove the hypothesis. Attaching the Pt NPs to pre-formed iron oxide NPs could provide better control over Pt NP sizes, as suggested by literature review. Therefore, the first step was to synthesize monodisperse iron oxide NP seeds. Here, the synthesis of crystalline and monodisperse iron oxide NPs is reported via a modified “heat-up” method.

Experiment

Synthesis of the precursor, iron oleate complex

The iron oleate complex was prepared by mixing ferric chloride (13 g), potassium salt of oleic acid (192.4 g) in a solvent mixture (hexane, 280 mL and ethanol, 160 mL) at 65 °C for 4 h. The mixture was phase-separated. The top organic phase contained the iron oleate complex. This was washed with de-ionized (DI) water (3 times) to remove by-products such as KCl. The paste-like iron oleate complex product was dried overnight in a chemical hood to remove volatile solvents. The precursor complex was used for further synthesis of iron oxide NPs.

Synthesis of the iron oxide nanoparticles

The iron oleate complex (1.8 g) was heated at 320 °C for 2.5 h in the presence of different capping molecules in 1-octadecene (13 mL). The precursor to capping molecule ratio (p/c) was kept the same in these reactions. Oleic acid (OA), OA/oleylamine (ON, 1:3 OA:ON molar ratio), and OA/trioctylphosphine oxide (TOPO, 0.6:1 OA:TOPO molar ratio) were the different surfactants used.

Using a OA/TOPO surfactant mixture, the amount of iron oleate complex was varied (1.8 g, 4 g, 6 g, and 8 g) to tune the surfactant packing density on iron oxide surfaces. The corresponding p/c were 2:1, 5:1, 8:1, and 10:1, respectively. All other reaction parameters were kept the same.

For transmission electron microscopy (TEM) analysis, the NPs were centrifuged out of the solution using a 1:1 volume ratio of ethanol and hexane, re-dispersed in hexane, and dropped on the TEM grid. In contrast, dry powder samples for crystal structure and magnetic property measurements were prepared by magnetically separating the NPs from solution using acetone and chloroform, followed by drying under vacuum.

Characterization

The size and morphology of the iron oxide NPs were examined on a FEI Tecnai F-20 TEM. The crystal structure of the NPs in dry powder form was studied on a Bruker AXSD8-Advanced XRD using a Co source (K_{α} , $\lambda = 1.79 \text{ \AA}$). The magnetic properties of these NPs in powder form were measured using a Princeton AGM at room temperature.

Results and Discussion

Monodisperse iron oxide NPs were synthesized via thermal decomposition of the iron oleate precursor in an organic solvent (1-octadecene) at 320 °C for 2.5 h using OA/TOPO surfactant mixture (OA:TOPO molar ratio 0.6:1, p/c = 8:1). The bright-field image suggested a 12 nm size of the NPs (Figure 3.1.1a). The high-resolution transmission electron microscopy (HRTEM) could show a single iron oxide NP (Figure 3.1.1b). The size of the NP in HRTEM was consistent with the bright-field data. This size is suitable for the potential use of the iron oxide NPs as carriers for small Pt NPs in the body. Generally, particles < 100 nm could evade clearance via macrophages. However, small NPs (< 5 nm) were rapidly removed by the reticuloendothelial system (RES). Therefore, the 12 nm iron oxide NPs could potentially have a long blood circulation time. They could also be conjugated to a targeting biomolecule without exceeding the 100 nm limit. The iron oxide NPs are crystalline, as suggested by the clear lattice fringes in the HRTEM. The crystal structure of the NPs was investigated using XRD (Figure 3.1.1c). For a

good XRD data, the organic ligand coating on the iron oxide surface was washed off via magnetic separation. Additionally, the vertical height (Z) of the powder sample was adjusted to focus the x-ray. The 2θ peaks at 35.1° , 41.4° , 50.4° , 63.1° , 67.5° , and 74.4° matched well with the (220), (311), (400), (422), (511), and (440) crystal planes of the maghemite structure. A maghemite structure was suggested, based on the (220) peak that is not seen in magnetite.¹ Since this peak is small, the possibility of a magnetite structure cannot be completely excluded. The measurement of magnetization of the sample versus applied magnetic field (M - H curve) is shown in Figure 3.1.1d. The M - H curve showed zero coercivity at zero magnetic field, or superparamagnetic behavior. The data also suggested no aggregation in the NP sample because the large aggregates would give a ferromagnetic loop. The saturation magnetization is lower (50 emu/g) than bulk iron oxides (maghemite = 78 emu/g, magnetite = 92 emu/g),² likely due to the surfactant coating.

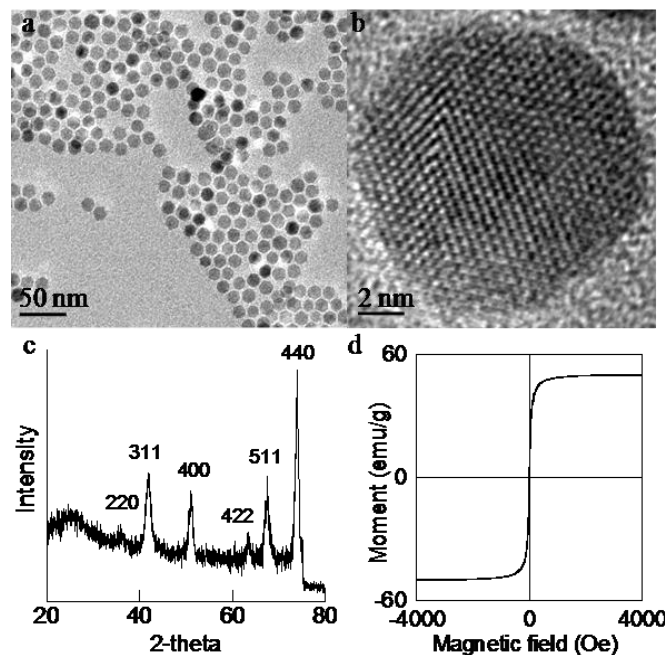


Figure 3.1.1. Iron oxide NPs with 8:1 p/c using OA/TOPO: (a) bright-field TEM, (b) HRTEM, (c) XRD scan, and (d) M - H curve.

The surfactant packing density on the iron oxide NP surface was tuned by using different amounts of the precursor ($p/c = 2:1, 5:1, 8:1$, and $10:1$), keeping all other parameters constant. The OA/TOPO surfactant mixture (OA:TOPO molar ratio 0.6:1) was used for the investigation. Monodisperse iron oxide NPs formed with 1.8 g iron oleate complex ($p/c 2:1$, Figure 3.1.2a). Based on the HRTEM image, the NPs were 15 nm in size, and highly crystalline (Figure 3.1.2a, inset). Figure 3.1.2b shows the uniform iron oxide NPs synthesized with $5:1$ p/c . The HRTEM image suggested ~ 13 nm size of the NPs (Figure 3.1.2b, inset). The NPs showed good crystallinity, as seen from the clearly visible lattice fringes in the HRTEM. The iron oxide NPs using 6 g iron oleate precursor ($p/c = 8:1$) showed good quality in terms of size, size distribution, and crystallinity (Figure 3.1.1a and b). These results suggested that uniform iron oxide NPs could be synthesized using different packing density of surfactant, OA/TOPO. However, at very high precursor amounts ($p/c = 10:1$) slight aggregation was observed, likely from insufficient surface coating.

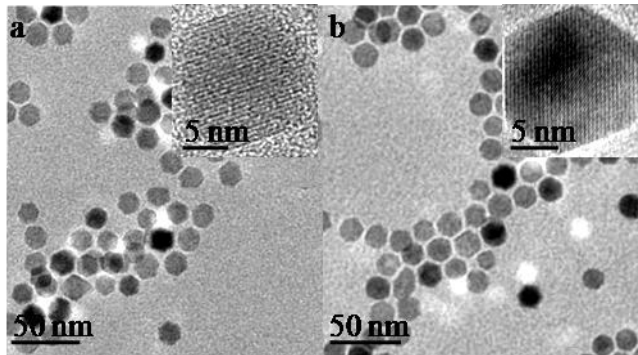


Figure 3.1.2. Iron oxide NPs using OA/TOPO surfactant with p/c : (a) $2:1$, HRTEM (inset), and (b) $5:1$, HRTEM (inset).

To investigate the effect of capping molecules on iron oxide NP synthesis, different surfactants were used, keeping the precursor to surfactant ratio constant. Monodisperse iron oxide NPs of size ~ 12 nm could be synthesized with only OA (Figure 3.1.3a) OA was used in

the traditional iron oleate based “heat-up” method, and is known to prevent NP aggregation through a strong surface protection.^{3,1} During the high temperature synthesis, the conformation of the OA is irreversibly changed to form a strong binding to the iron oxide surface.^{4,5} The result with OA was consistent with earlier reports. However, OA/ON surfactant mixture (OA:ON molar ratio = 1:3) induced an irregular morphology in iron oxide NPs (Figure 3.1.3b). This is likely due to the competing surface binding forces of OA and ON. ON has a slightly stronger attraction for the iron oxide surface.¹ The strong preferential binding of both ligands to the iron oxide surface could facilitate the irregular NP shape. Therefore, the OA/ON ligand mixture suggested a significant role of ligand binding energies on the NP size and shape. Interestingly, the OA/TOPO surfactant mixture could form monodisperse NPs because TOPO had a much lower binding energy, compared to OA (Figure 3.1.1 and 3.1.2).

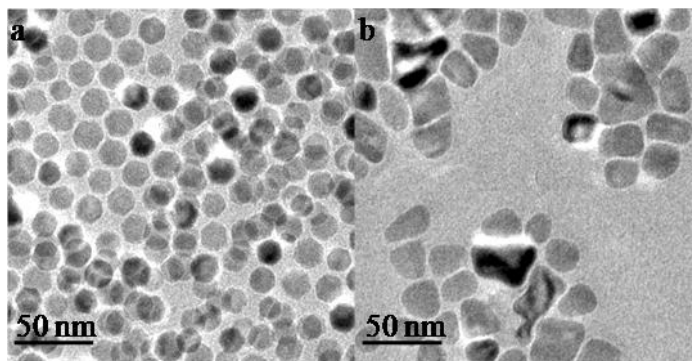


Figure 3.1.3. Bright-field TEM image of iron oxide NPs with other capping molecules: (a) only OA, (b) OA/ON mixture.

The synthesis of iron oxide NPs showed good reproducibility. Figure 3.1.4 is a column plot of the sizes of NPs obtained from 10 reactions using OA/TOPO surfactant (OA: TOPO molar ratio, 0.6:1). The NP size variation was small (12-15 nm). The error bars showed low standard deviation (± 2 nm).

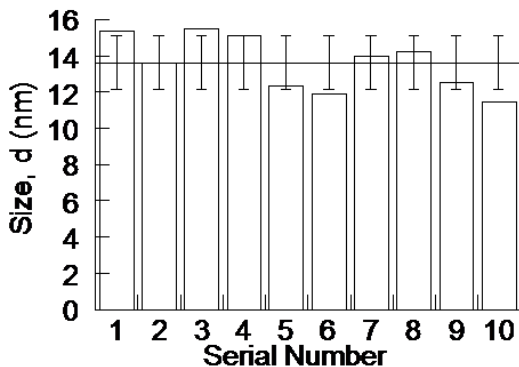


Figure 3.1.4. Column graph showing repeatability of iron oxide NPs.

Conclusion

Monodisperse iron oxide NPs of good crystallinity were successfully synthesized using thermal decomposition of the iron oleate complex. The surfactant binding energy played a significant role in size and shape of the iron oxide NPs. Good spherical iron oxide NPs could be obtained using OA, and OA/TOPO. However, irregular shaped iron oxide NPs formed with OA/ON, likely due to the high binding affinity of both ligands to the iron oxide surfaces. The effect of surfactant packing density on NP size distribution was investigated using OA/TOPO. It was concluded that monodisperse iron oxide NPs could be formed up to 8:1 precursor/surfactant molar ratios. The NPs with different surfactant packing density were similar in size.

3.2 Platinum Attached Iron Oxide Nanoparticles via Organic Route

Multiple Pt NP attachment was first investigated in an organic solvent (organic route) using the iron oxide NP seeds. In this method, heterogeneous nucleation of small Pt NPs was induced on iron oxide surfaces, prior to an aqueous phase transfer of the whole integrated NP (Figure 3.2.1). The advantage of this route for our purpose was that the biocompatible coating could protect the therapeutic Pt NP components from non-target interactions.

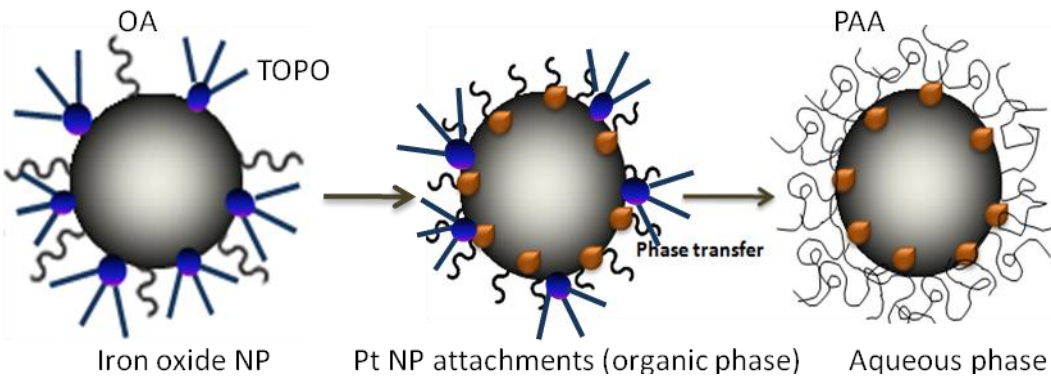


Figure 3.2.1. Pt NP attachments via organic route

Experiment

The powder Pt precursor, K_2PtCl_4 (5 mg) was dissolved in 1-octadecene (10 mL) with 1:1 molar ratio of the reducing agent, dodecanediol, until a clear yellow solution was formed at 70 °C. The homogeneous solution was cooled to 30 °C. Next, an iron oxide NP seed solution (5 mL) and reducing agent, oleylamine (1 mL) was injected, and the solution was allowed to mix for 0.5 h. The reactants were heated at 140 °C for 4 h.

Different ligand (*e.g.*, OA/TOPO, OA, and OA/ON) capped iron oxide NP seeds were used to study the effect of ligand coating on Pt attachment reaction, keeping all other parameters constant. The effect of surfactant packing density on Pt NP attachments in organic solvent was investigated using OA/TOPO coated iron oxide seeds with different p/c (2:1, 5:1, 8:1, and 10:1). The desired reaction temperature was varied (110 °C, 140 °C, and 180 °C) using OA/TOPO iron oxide seeds to tune the Pt attachments. To study the influence of the Pt precursor, the molar ratio of the Pt precursor to iron oxide seeds was changed (*e.g.*, 120:1, 240:1, 360:1, and 540:1), keeping all other reaction parameters constant.

Characterization

The NPs were imaged on a FEI Tecnai F-20 TEM. The magnetic properties of the powdered NPs were measured using a Princeton AGM at room temperature. Samples for the TEM and

AGM were prepared as described earlier.

Results and Discussion

Iron oxide seeds were injected into Pt precursor solution at 140 °C, in the presence of a reducing agent to grow Pt NPs on iron oxide NP surfaces. K₂PtCl₄, the powder Pt precursor, can be reduced with more control, compared to other Pt salts (*e.g.*, Pt(acetylacetonate)₂). Additionally, Pt complexes are known to reduce easily at 140 °C.⁶ According to classical nucleation theory, the seed size can greatly influence heterogeneous nucleation.⁷ Therefore, iron oxide NPs of similar size (~ 12 nm) were used for reference. Figure 3.2.2 shows the influence of capping molecules on the Pt attachment reaction, keeping all other parameters constant (140 °C, 5 h). The higher atomic number (Z) Pt NPs appear as small, darker dots compared to the iron oxide seeds. With OA coated iron oxide NPs, many free small Pt NPs were observed (Figure 3.2.2a). Since the iron oxide seeds were very uniform, the small NPs could be assigned to Pt NPs. The challenge in obtaining Pt attachments using OA surfactant was likely due to the strong binding of OA.¹ The compact coating on the iron oxide seeds prevented heterogeneous nucleation of Pt NPs. However, single Pt NP attachments were seen in the OA/TOPO coated seeds (Figure 3.2.2b). Higher atomic number (Z) Pt NPs appear darker in the bright field image, compared to the iron oxide NPs. This dark dot is clearly visible in the HRTEM image (Figure 3.2.2c) that suggests single Pt NP attachment. Here, the size of the Pt NP is ~ 4 nm. The weak binding ligand, TOPO likely facilitated Pt NP attachments via a less compact surface coating on iron oxide seeds. Interestingly, increased Pt attachments were also observed in OA/ON coated seeds (Figure 3.2.2d). The size of Pt NPs was slightly larger (~ 5 nm) than the OA/TOPO seeds (Figure 3.2.2e). Here, the irregular NP shape with sharp edges and corners could have induced the Pt attachments.⁸

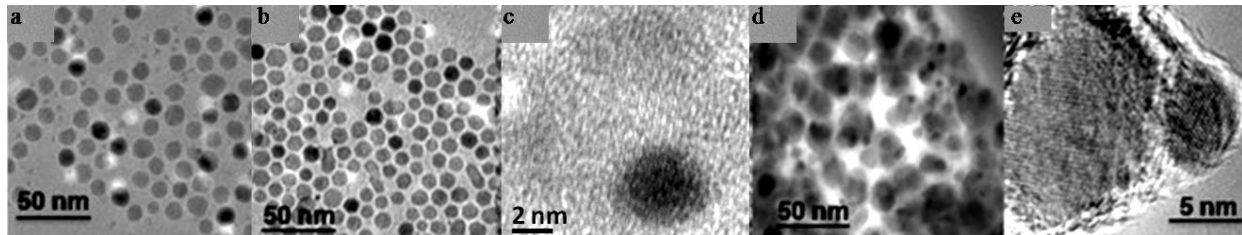


Figure 3.2.2. Single Pt attached iron oxide NPs: (a) OA coated seeds, (b) OA/TOPO coated seeds, (c) HRTEM image of sample b, (d) OA/ON coated seeds, and (e) HRTEM of sample d.

Using the more reproducible OA/TOPO seeds, the Pt NP attachment was investigated at different reaction temperatures ($110\text{ }^{\circ}\text{C}$, $140\text{ }^{\circ}\text{C}$, and $180\text{ }^{\circ}\text{C}$). The observed results at $110\text{ }^{\circ}\text{C}$ (Figure 3.2.3a) were similar to the attachments at $140\text{ }^{\circ}\text{C}$ (Figure 3.2.3b). However, free Pt nanowires resulted at $180\text{ }^{\circ}\text{C}$ from self-nucleation because the Pt self-nucleation rate increases with temperature (Figure 3.2.3c). These results suggested that the OA/TOPO surfactant coating and a $140\text{ }^{\circ}\text{C}$ reaction temperature could best induce single Pt attachments. These reaction parameters were further used for the multiple Pt attachment studies.

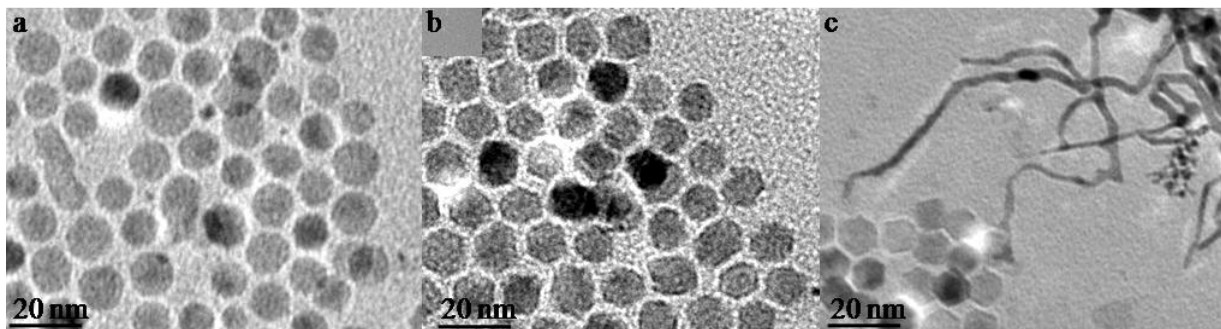


Figure 3.2.3. Pt attachments at different temperatures, using OA/TOPO coated iron oxide seeds: (a) $110\text{ }^{\circ}\text{C}$, (b) $140\text{ }^{\circ}\text{C}$, and (c) $180\text{ }^{\circ}\text{C}$.

The influence of surfactant packing density was investigated to obtain multiple Pt attachments on iron oxide NP seeds. Here, OA/TOPO coated iron oxide NPs seeds with different surface packing (p/c 2:1, 5:1, 8:1, and 10:1) were heated with the Pt precursor (molar ratio of Pt precursor: iron oxide NPs, 120:1) at $140\text{ }^{\circ}\text{C}$ for 5h. Figure 3.2.4 shows the Pt attachments

obtained with the different iron oxide NPs. Few Pt attachments were observed using 2:1 p/c seeds (Figure 3.2.4a). The 5:1 p/c iron oxide seeds also did not show much improvement (Figure 3.2.4b). However, significant Pt NP attachments were achieved using iron oxide seeds with 8:1 p/c (Figure 3.2.4c). Multiple Pt NPs were attached on iron oxide surfaces of this seed, as suggested by the dark dots surrounding the iron oxide NPs. The unprotected sites available for nucleation of Pt NPs likely increased with reduced surfactant packing on the iron oxide surface. The iron oxide seeds with 10:1 p/c showed slight aggregation from insufficient capping molecules (Figure 3.2.4d), and were not suitable for uniform Pt attachments.

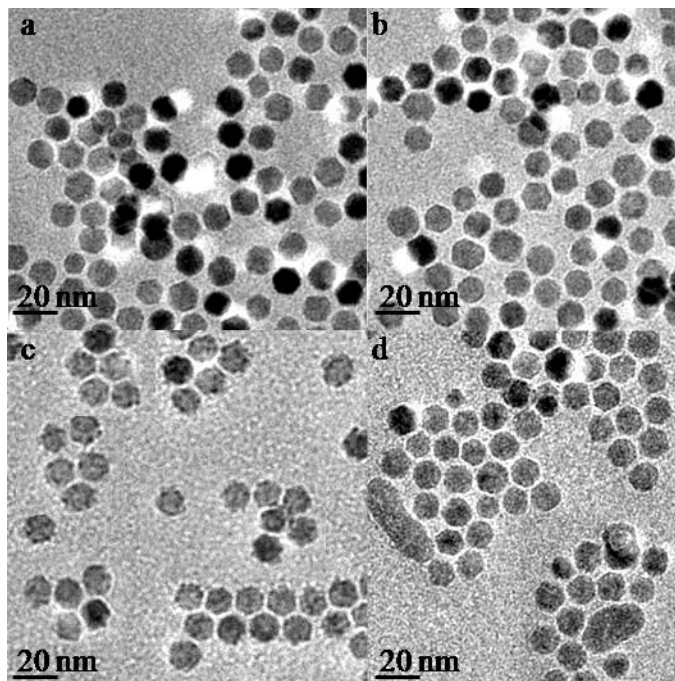


Figure 3.2.4. Bright-field TEM images of multiple Pt attachments using iron oxide NPs seeds with P/C: (a) 2:1, (b) 4:1, (c) 8:1, and (d) 10:1.

The molar ratio of Pt precursor to iron oxide seeds was increased to 240:1, 360:1, and 540:1 to further increase the density of Pt NPs on the iron oxide surfaces. Although the experiments were performed using all four iron oxide seeds, the 8:1 ratio seeds were found to be most suitable as seen earlier. At Pt precursor to iron oxide molar ratio 540:1, Pt NPs showed considerable self

nucleation due to the presence of excess Pt precursor. Figure 3.2.5 shows a representative TEM image of the multiple attachments of Pt NPs obtained at a ratio of 360:1, which gave the best results. Multiple Pt attachment was apparent from the rough edges of the iron oxide surfaces that were relatively smooth prior to attachment reactions (Figure 3.2.5a). Additionally, the HRTEM image (Figure 3.2.5a, inset) showed several Pt NPs of size 2 nm attached to the surface of the iron oxide NP seed. However, it was challenging to identify the Pt NPs in a XRD scan due to the significant size broadening of the small Pt NPs. Alternatively, EDX and HAADF imaging of the TEM was used to confirm the presence of Pt NPs on the iron oxide seeds. The high angle annular detector used to record HAADF images minimizes Bragg's reflections. The major contributor in HAADF imaging is the thermal diffused scattering, which is negligibly affected by the sample thickness and defocus. Consequently, even though the Pt NPs on the iron oxide surface were small in size, they were effectively captured in a HAADF image (Figure 3.2.5b). The contrast in a HAADF image depends on the atomic number (Z) of the element such that the heavier elements appear brighter. Hence, the scattered bright dots on the darker iron oxide suggested the presence of Pt attachments on iron oxide surfaces. The EDX spectrum provides useful information about the chemical composition of the sample. Here, the characteristic x-rays scattered by the individual elements in the sample are recognized. The EDX spectrum of this sample was obtained by focusing the nanoprobe on the surface of the iron oxide NPs. The elements, Fe, O, and Pt were clearly visible in the spectrum (Figure 3.2.5c). The high Cu peak came from the TEM grid, while the K was likely from the trace amounts of remaining by-product (KCl) formed during the synthesis of the iron oleate precursor. Therefore, the EDX spectrum supported the presence of attached Pt NPs on the iron oxide NP surfaces. However, the addition of Pt NPs on the surface did not cause any significant change in the magnetic

characteristics of the iron oxide seeds, according to the room temperature M - H curve (Figure 3.2.5d).

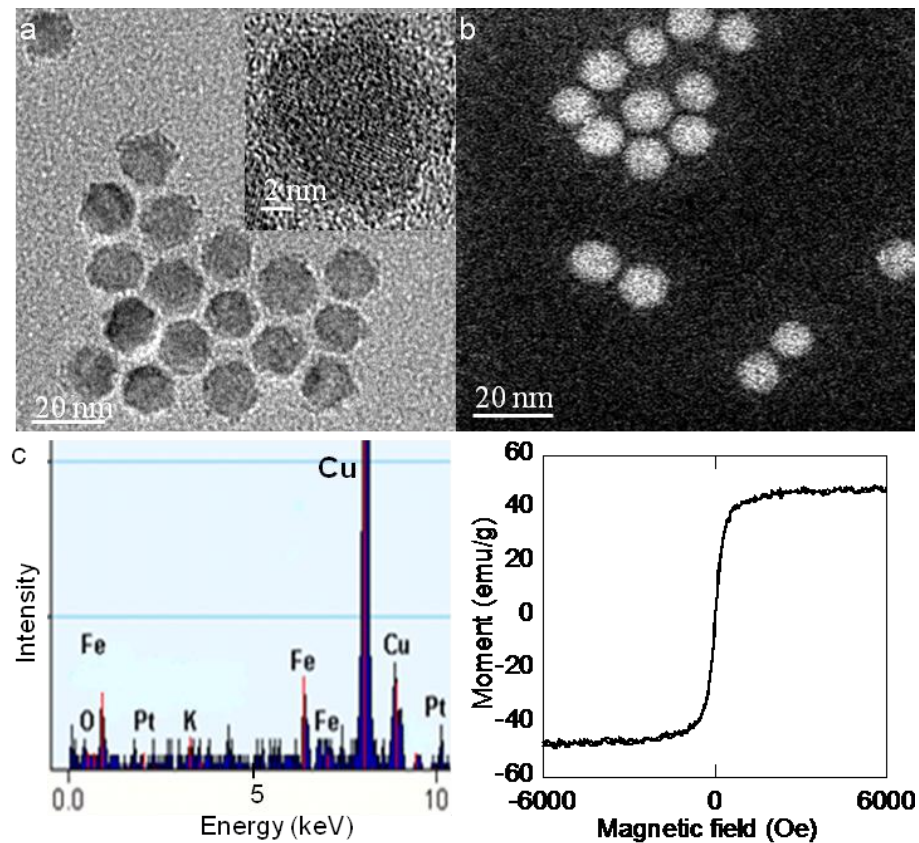


Figure 3.2.5. Multiple Pt-attached spherical iron oxide NPs. (a) TEM image, HRTEM image (inset), (b) HAADF images, (c) EDX spectrum, and (d) M - H curve.

Conclusion

In conclusion, the reaction parameters suitable for Pt NP attachments onto iron oxide surfaces were investigated via an organic route. Capping molecule binding to the iron oxide surface played a key role in Pt NP attachment. The OA/TOPO capped iron oxide NPs gave the most reproducible single Pt NP attachments. The attachment reactions were favorable at 140 °C, the temperature known for easy Pt reduction. At higher reaction temperatures, the Pt showed self-nucleation. It was concluded that a low surface packing density of OA/TOPO on iron oxide

NPs (p/c 8:1) could facilitate multiple Pt NP attachment. An increase in the molar ratio of Pt precursor to iron oxide NPs (360:1) also induced high quality Pt NP attachments.

3.3 Shape Controlled Iron Oxide Nanoparticles

Shape controlled iron oxide NPs were synthesized with the aim to improve attachment density of small Pt NPs on iron oxide seed surfaces. Heterogeneous nucleations, such as Pt NPs on iron oxide surfaces are known to prefer irregular surfaces with sharp edges and corners.^{7,8} Here, the synthesis of iron oxide nanowhiskers, nanoworms, nanoplates, and nanoflowers via thermal decomposition of iron oleate precursor is reported. Multiple Pt NP attachments were investigated using each of these shapes. The attachments were performed with 360:1 molar ratio of Pt precursor to iron oxide seeds, using the organic route described in Section 3.2.

3.3.1 Iron Oxide Nanowhiskers

Experiment

Synthesis of the Fe (III) oleate complex

The iron oleate complex was prepared by mixing ferric chloride (13 g), potassium salt of oleic acid (192.4 g) in a solvent mixture (hexane, 280 mL and ethanol, 160 mL) at 60 °C for 4 h. The mixture was phase-separated and washed with de-ionized (DI) water to remove by-products. The paste-like iron oleate complex was dried overnight in a chemical hood to remove volatile solvents. The precursor complex was subsequently used for nanowhisker synthesis.

Synthesis of the Fe (III) laurate complex

Typically, iron laurate complex was prepared by mixing ferric chloride (13 g), potassium salt of lauric acid (192.4 g) in a solvent mixture (hexane, 280 mL and ethanol, 160 mL) at 60 °C for

4 h. The mixture was phase separated, washed with de-ionized (DI) water, and dried as described earlier. The complex was subsequently used for nanowhisker synthesis.

Synthesis of the Fe (II) oleate and Fe (III)/Fe (II) oleate complexes

The Fe (II) oleate and the Fe (III)/Fe (II) oleate complex mixtures were prepared to better understand nanowhisker formation. Typically, Fe (III) chloride (4.3 g) and Fe (II) chloride (1.69 g, $\text{Fe}^{3+}/\text{Fe}^{2+} = 2:1$) or Fe(II) chloride (5.07 g) were reacted with the sodium oleate (36.5 g) in a solvent mixture (hexane-140 mL, ethanol-80 mL, and DI water-60 mL) at 60 °C for 4 h. The mixture was processed like the Fe (III) oleate complex. The entire preparation was performed under an argon atmosphere to prevent oxidation of Fe (II).

Synthesis of iron oxide nanowhiskers

Typically, iron oxide nanowhiskers were synthesized by heating the iron oleate complex (1.8 g) in 1-octadecene (13 mL) at 150 °C in the presence of surfactants (0.3 mL OA, 0.1 OA mL/0.2 g TOPO, or 0.1 mL OA/0.2 mL ON) for 2.5 hours. A time-dependent study was performed at different reaction times (*e.g.*, 0.5 h, 1.5 h, 2.5 h, 6 h, and 22 h), keeping all the other parameters same. The Fe (III) oleate nanowhiskers were also synthesized in toluene (13 mL) using OA/TOPO as the surfactant. NP syntheses using Fe (II) oleate, Fe (II)/Fe (III) oleate mixture, Fe(II) stearate (purchased), Fe (III) stearate (purchased), and Fe (III) laurate as precursors were performed under the same conditions. Samples for TEM were prepared as described earlier. Powder samples were prepared for XRD, XPS, Raman spectroscopy, TGA, AGM and FTIR.

Characterization

The size and morphology of the iron oxide nanowhiskers were studied using a FEI Tecnai F-20 TEM. The crystal structure of the nanowhiskers in dry powder form was investigated by a Bruker AXSD8-Advanced XRD using a Co source (K_{α} , $\lambda = 1.79 \text{ \AA}$). We used a Kratos AXIS 165

Multitechnique Electron Spectrometer to confirm the nanowhisker crystal phase. The Raman analysis was performed on a Bruker Senterra system (Bruker Optics Inc. Woodlands, TX). The TGA of the nanowhiskers was performed on a TA Instruments TGA 2950 thermogravimetric analyzer (New Castle, DE). The magnetic properties of the powdered nanowhiskers were measured using a Princeton AGM at room temperature. PerkinElmer Spectrum 100 FT-IR spectrometer (Bucks, UK) was used to investigate the surface functional groups of the nanowhiskers.

Results and Discussion

Iron oxide nanowhiskers were formed by heating the iron oleate precursor in octadecene at 150 °C using the usual surfactant mixture of OA/TOPO (0.6:1 molar ratio of OA:TOPO, p/c = 2:1). The nanowhiskers, approximately 2 x 50 nm in dimension were repeatedly observed at the above reaction conditions (Figure 3.3.1.1a). Due to the high aspect ratio of the thin nanowhiskers, it was difficult to focus them for HRTEM imaging. Even then, the lattice fringes were clearly visible, suggesting a crystalline morphology of the nanowhiskers (Figure 3.3.1.1b). Additionally, the calculated interfringe distance of 0.298 nm was approximately equal to the d-spacing of (220) crystal plane in a cubic iron oxide spinel structure. Figure 3.3.1.1c shows a plot of magnetization versus applied field for the iron oxide nanowhiskers. A combination of superparamagnetism and paramagnetism was observed with no saturation magnetization. The nanowhiskers had a large number of surface atoms due to their high surface-to-volume ratio. Therefore, the large number of paramagnetic ligand molecules on the surface of the iron oxide nanowhiskers could generate a magnetic “dead-layer” via enhanced surface spin disorder. This dead-layer accounts for the paramagnetic region in the *M-H* curve.⁹ Increased ligand molecules on the surface of the iron oxide nanowhiskers made it difficult to obtain crystal structure

information of the powdered sample via XRD. However, the XRD scan using a Co source showed peaks for (220), (311), and (411) crystal planes of maghemite (Figure 3.3.1.1d). This led us to believe that the nanowhiskers could belong to a maghemite crystal phase.

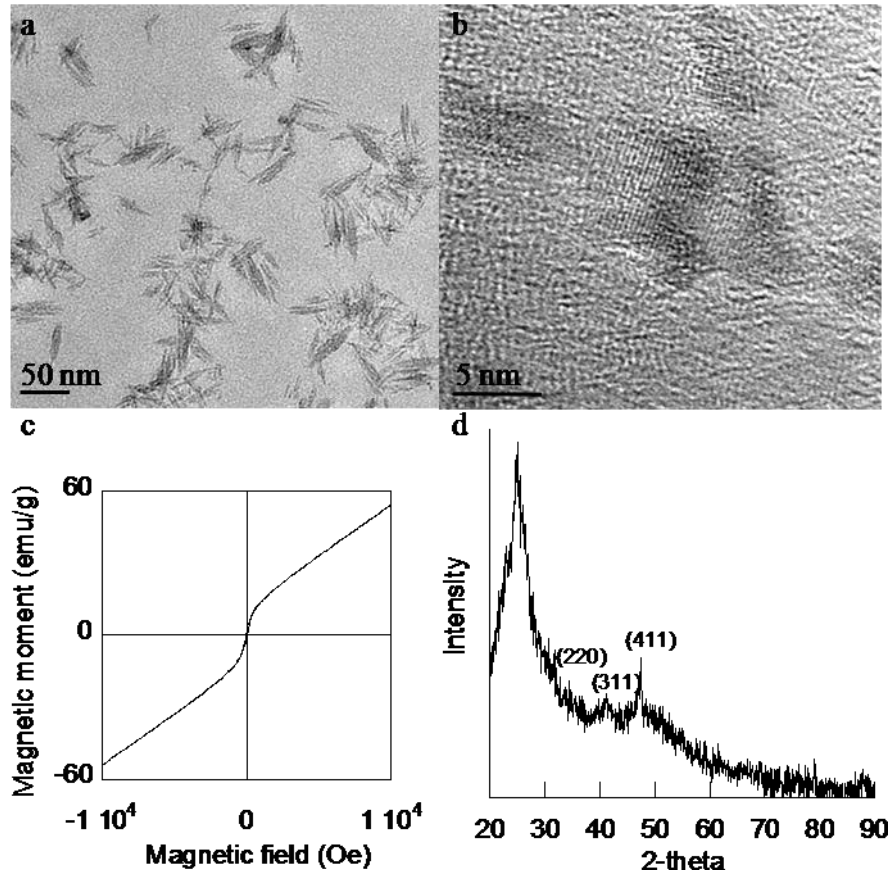


Figure 3.3.1.1. Iron oxide nanowhiskers: (a) bright-field TEM image, (b) HRTEM, (c) *M-H* curve, and (d) XRD scan.

Since, only three peaks were visible in the XRD scan, additional characterization was performed on the iron oxide nanowhiskers to remove any doubt about its crystal phase. Figure 3.3.1.2a shows the Raman spectrum obtained from a Bruker Senterra system. The main peaks of the spectrum at 725, 1295, and 1430 cm^{-1} could be assigned to iron oxide.¹⁰ However, the characteristic peak of magnetite at 670 cm^{-1} was absent, excluding the possibility of a magnetite crystal phase. Although, bulk maghemite is metastable and undergoes a phase transition to

hematite above 300 °C, nanoscale maghemite is known to be thermodynamically stable. Hematite shows sharper peaks in the Raman spectrum, especially in the interval 200 cm⁻¹- 400 cm⁻¹. It is unlikely that the nanowhiskers were hematite because they showed no sharp peaks in this range. This strengthened our belief that the nanowhiskers showed a maghemite crystal structure. The broad peak at 1610 cm⁻¹ can be assigned to adsorbed moisture on the surface or – OH groups. Further, a core-level XPS plot in the Fe 2p region was obtained to determine the atomic ratio of iron and oxygen in the nanowhiskers (Figure 3.3.1.2b).¹¹ This method has been effectively used to distinguish between the maghemite and magnetite phases. The two major peaks at 710 eV and 725 eV matched perfectly with the 2p_{3/2} and 2p_{1/2} core-levels of iron oxide. Hematite crystal phase shows two distinct 2p_{3/2} peaks in the XPS pattern. A single 2p_{3/2} peak was observed in our sample, ruling out the possibility of a hematite phase. Small shoulder peaks at 718 eV, 730 eV, and 745 eV, which are characteristic of maghemite indicated the presence of a maghemite crystal structure, not magnetite.^{12,13} Additionally, an electron diffraction pattern (ED) from the TEM also supported the maghemite phase (Figure 3.3.1.2c). From the ED pattern, the d-spacing of the crystal planes (d) can be calculated as follows:

$$L\lambda = Rd$$

7

where L (= 680 mm for the TEM used) is the distance between the film and the sample known as the camera constant, λ (= 0.0251 Å) is the wavelength of the electron beam, and R is the radius of the diffraction rings.¹⁴ The diffraction pattern indexed using equation 7 corresponded well to the (220), (311), (400), (511), (440), and (533) crystal planes of maghemite. The small dots in the ED, instead of the rings showed that the nanowhiskers were single-crystalline.

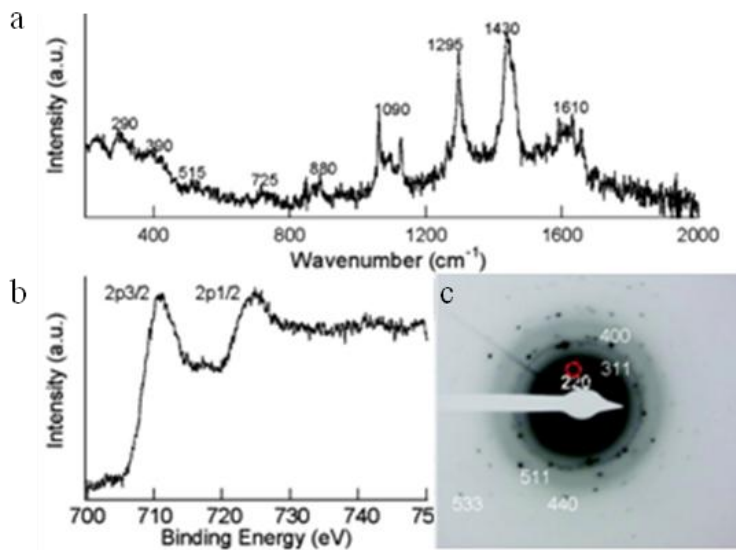


Figure 3.3.1.2. Additional characterizations confirming the maghemite crystal structure of nanowhiskers: (a) Raman spectrum, (b) Fe 2p core-level spectrum, and (c) electron diffraction pattern.

A TGA analysis was performed on the synthesized iron (III) oleate precursor. The TGA gave an indirect estimation of the ligand binding strengths by recording the weight loss of the precursor under thermal decomposition (Figure 3.3.1.3). The initial weight loss around 100 °C could be assigned to the evaporation of volatile solvents used to synthesize the iron (III) oleate complex (3.3.1.3). The second major weight loss from 150 – 230 °C was correlated to the dissociation of the two symmetric oleate ligand molecules from the iron oleate (Figure 3.3.1.3-a). These two ligands had lower binding energies compared to the third oleate ligand, according to theoretical calculations.¹⁵ The small percentage loss in weight in the range 230 – 295 °C was from the dissociation of the third ligand with higher binding energy (Figure 3.3.1.3-b). In these two decompositions, release of CO₂ was responsible for the weight loss. Therefore, the dissociation process is best explained by the ketonic decarboxylation reaction suggested in many other studies on iron carboxylate complexes (equation 8).^{16,17}



8

A continuous loss in weight was observed from 295 – 345 °C due to desorption of the dissociated ligands (Figure 3.3.1.3-c). When the complex was heated above 350 °C, all the organic components evaporated, which accounted for the final weight loss (Figure 3.3.1.3-d). The results from the TGA and DFT calculations suggested a difference in the binding strengths of the three ligands in the iron oleate complex. In our synthesis at 150 °C, the symmetrically attached ligand arms having lower binding energies could decompose, leaving the strongly bound third ligand to direct the crystal growth of the iron oxide nanowhiskers. At higher temperatures, however, the third ligand gradually decomposed, causing the nanowhiskers to break down.

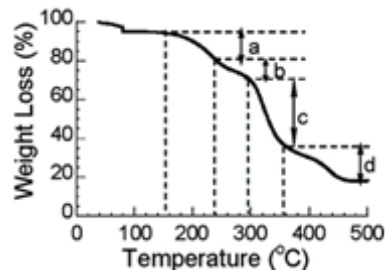


Figure 3.3.1.3. TGA plot of iron oleate complex.

The morphology of the nanowhiskers was studied at different reaction times (*e.g.*, 0.5, 1.5, 2.5, 6, and 22 h) to understand the growth mechanism. The samples were directly observed in the TEM without further treatment. No nanowhiskers were visible at 0.5 h, and the paste-like structure indicated the presence of an un-decomposed precursor complex (Figure 3.3.1.4a). Nanowhisker formation began after 1.5 h, but the product was not pure and crystalline. Fully-formed crystalline, maghemite nanowhiskers resulted at the normal reaction time, 2.5 h (Figure 3.3.1.1a). The nanowhisker morphology was retained after 6 h (Figure 3.3.1.4b). These nanowhiskers showed improved crystallinity, and were easier to focus in the TEM. However,

some aggregation was observed. Unfortunately, the nanowhiskers formed bundles or aggregated assemblies with increased reaction time (22 h), likely to reduce their surface energy (Figure 3.3.1.4c). However, the nanowhisker morphology could still be distinguished, suggesting good structural stability under prolonged heating. The nanowhisker bundles did not show a combination of paramagnetism and superparamagnetism like the isolated nanowhiskers. A ferromagnetic loop was seen on measuring the magnetization of the nanowhisker bundles against the applied magnetic field (Figure 3.3.1.4d).

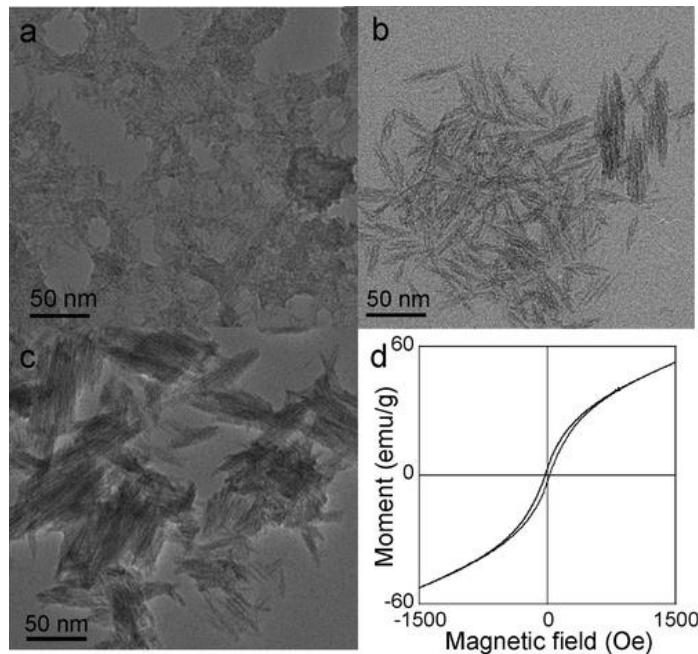


Figure 3.3.1.4. Time-dependent morphology evolution of the nanowhiskers: (a) 0.5 h, (b) 6 h, (c) 22 h, and (d) the M - H curve of assembled nanowhisker bundles.

Other precursors with iron oleate-like chemical structures (*e.g.*, Fe (III) stearate and Fe (III) laurate) were investigated for nanowhisker reactions. All these precursors had three ligand molecules (oleate, stearate, or laurate) binding to the Fe^{3+} cation. The only difference came from the chain length or saturation of the anion C-chain. Interestingly, the Fe (III) stearate formed crystalline, high aspect ratio nanowhiskers (Figure 3.3.1.5a). The Fe (III) laurate gave

nanowhiskers with a porous morphology (Figure 3.3.1.5b). Further investigations are required to understand the porous nature of these nanowhiskers. Incidentally, iron laurate had been used in an earlier report to synthesize nanoporous frameworks.¹⁸ These results further supported the possible role of the different binding energies of the three ligands in nanowhisker synthesis. Additionally, the Fe (III) stearate was a stable commercially available precursor. Therefore, artifacts during the precursor synthesis could not be responsible for these nanostructures.

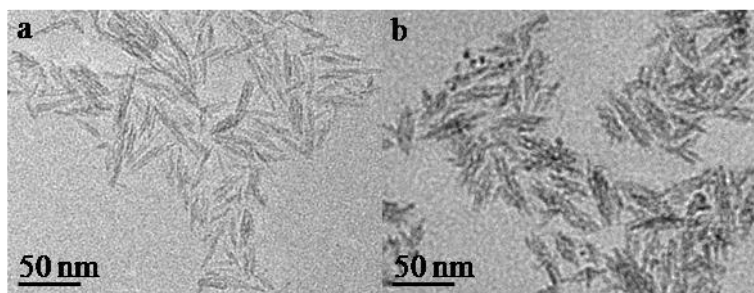


Figure 3.3.1.5. Bright-field TEM images of iron oxide nanowhiskers using different precursors: (a) iron stearate, and (b) iron laurate.

Selective adhesion of capping molecules is known to influence the NP morphology. In nanowhisker synthesis, a mixture of strong binding ligand, OA, and weak binding ligand, TOPO, was used as the surfactant. The morphology of the product was also investigated under the influence of OA/ON and only OA, keeping the same overall molar ratio of precursor to capping molecules (2:1). ON, being a stronger binding ligand than TOPO competes with OA for surface adhesion, but the overall morphology of the nanowhiskers remained the same (Figure 3.3.1.6a). Slightly aggregated nanowhiskers were observed with a single strong binding capping molecule, OA (Figure 3.3.1.6b). However, all the surfactant combinations showed nanowhisker-like morphologies. Therefore, the selective adhesion of the surfactant molecules could not be the primary cause of the nanowhiskers. Additionally, nanowhiskers could be synthesized with a different solvent (toluene), keeping all the other parameters same (Figure 3.3.1.6c). Toluene had

a low boiling temperature (110 °C). This ruled out the influence of the solvent in nanowhisker morphology.

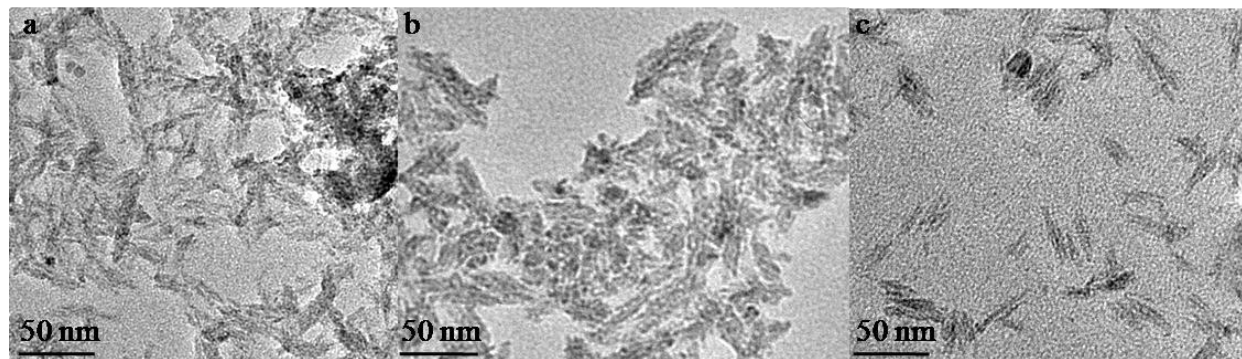


Figure 3.3.1.6. Influence of capping molecules and solvent on the nanowhisker morphology, using: (a) surfactant mixture of OA/ON, (b) surfactant OA, and (c) solvent toluene.

A temperature-dependent study was performed to understand the growth mechanism of the nanowhiskers. At 100 °C, the dark paste-like product suggested incomplete decomposition of the precursor (Figure 3.3.1.7a). Pure iron oxide nanowhiskers formed between 110 °C and 160 °C. A reaction temperature of 150 °C was found to be most suitable (Figure 3.3.1.1a). Decomposition of the two oleate ligands in the precursor occurred in this temperature range, and could be responsible for the nanowhiskers. However, at 180 °C, cavities began to form within the nanowhiskers (Figure 3.3.1.7b). On further increasing the temperature to 230 °C, irregular shapes were observed (Figure 3.3.1.7c). The nanowhiskers became porous and finally broke down at high temperatures, forming normal iron oxide NPs at 300 °C. This suggested that the decomposition of the third oleate ligand at higher temperatures damaged the surface stability of the nanowhiskers. The result was consistent with our TGA analysis.

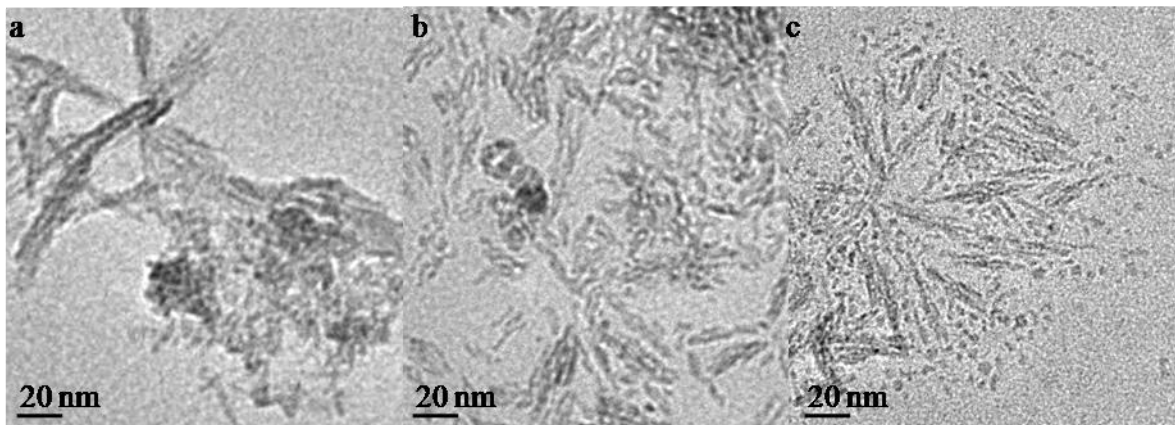


Figure 3.3.1.7. Temperature-dependent nanowhisker morphology at: (a) 100 °C, (b) 180 °C, and (c) 230 °C.

A FTIR analysis could give information about the surface coordination of the iron oleate complex and the nanowhiskers to confirm the proposed ligand-directed growth mechanism (Figure 3.3.1.8). The coordination bonds in a metal carboxylate can be estimated from the difference between their symmetric and asymmetric COO⁻ vibrations (Δ). The bonds could be monodentate ($\Delta = 200 - 300 \text{ cm}^{-1}$), bridging bidentate or ionic ($\Delta = 110 - 200 \text{ cm}^{-1}$), and chelating bidentate ($\Delta < 110 \text{ cm}^{-1}$).¹⁹ The iron (III) oleate complex showed characteristic FTIR bands of metal carboxylates at 1176, 1418, 1580, and 1710 cm^{-1} . The band at 1710 cm^{-1} could be from free OA²⁰ or asymmetric unidentate carboxylate.²¹ The Δ was 162 cm^{-1} , calculated from the two characteristic bands of iron (III) oleate at 1580 cm^{-1} and 1418 cm^{-1} . This suggested a bridging coordination of the ligand molecules with two low-dissociation symmetric ligands and one strongly bound ligand. The band at 1710 cm^{-1} was not seen for the iron oxide nanowhiskers, suggesting that the remaining ligands were directly attached to the iron oxide surface. The nanowhiskers also showed a bridging coordination ($\Delta = 128 \text{ cm}^{-1}$), much like the iron oleate precursor.

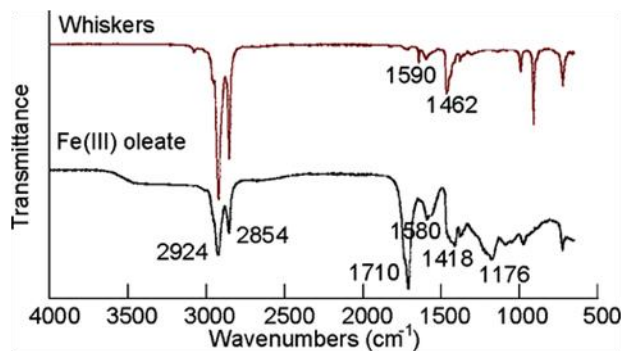


Figure 3.3.1.8. FTIR spectra of the iron oleate complex (bottom), and iron oxide nanowhiskers synthesized with OA (top).

Finally, the role of the third ligand was indirectly confirmed using Fe (II) oleate and Fe (II)/Fe (III) oleate precursor complexes for the nanowhisker synthesis reaction. These complexes were prepared carefully under inert gas protection to prevent oxidation. The Fe (II) precursor gave irregular and somewhat aggregated NPs, significantly different from the nanowhiskers (Figure 3.3.1.9a). This could be explained from the absence of the growth-directing third ligand in the Fe (II) oleate. A mixture of nanowhiskers and sphere-like NPs were formed with the Fe (II)/Fe (III) oleate complex, likely due to the presence of oleate structures both with and without the third ligand (Figure 3.3.1.9b).

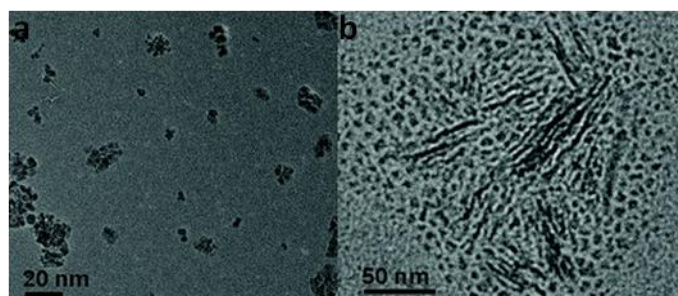


Figure 3.3.1.9. (a) Irregular particles from decomposition of Fe(II) oleate, and (b) a mixture of sphere-like NPs and nanowhiskers from the decomposition of the Fe(II) and Fe(III) oleate complex mixture.

Conclusion

Iron oxide nanowhiskers of dimension 2 x 50 nm were synthesized by selectively heating the iron oleate complex at 150 °C. So far, the formation of thin, one-dimensional iron oxide NPs has not been reported. Based on XRD, XPS, and Raman analyses, the nanowhiskers belonged to a maghemite crystal phase. TGA analysis and electronic structure calculations suggested an important role of ligand coordination microenvironments in nanowhisker formation. We proposed a ligand-directed growth of the nanowhiskers, based on time-dependent reactions. The result obtained from decomposition of Fe (II) and Fe (III) oleate complexes, and FTIR analysis was consistent with the hypothesis.

3.3.2 Iron Oxide Nanoworms

Experiment

The iron oxide nanoworms (NWs) were synthesized using a modified “heat-up” method. The iron oleate complex (1.8 g) was heated in 1-octadecene (13 mL) in presence of OA (0.1 mL). During the reaction, a solution of TOPO (0.8 g) in 1-octadecene (7 mL) was injected in the reaction mixture at 290 °C. The reactants were then heated at 320 °C for a total reaction time of 2.5 h. The growth mechanism of the NWs was investigated through different reaction times (1 h, 2.5 h, and 5 h), keeping all the other parameters constant.

Characterization

FEI Tecnai F-20 TEM was used to examine the size and morphology of iron oxide NWs. The crystal structure of the powdered NW sample was investigated with a Bruker AXSD8-Advanced XRD (Co K_α source, $\lambda = 1.79 \text{ \AA}$). The magnetic behavior of NWs was studied on a Princeton AGM at room temperature.

Results and Discussion

Iron oxide NWs were synthesized via thermal decomposition of the iron oleate precursor in the presence of TOPO/OA (TOPO: OA molar ratio, 6.3:1) surfactant mixture. The surfactant, OA, is known to form iron oxide spheres with good size distribution via a compact surface coating.³ We had used TOPO/OA surfactant mixtures to synthesize uniform iron oxide NPs in earlier reactions. Here, the modification was the increased percentage coating of TOPO, and the injection of TOPO at 290 °C. The injection was designed to tune NP growth only, not nucleation. The injection temperature was chosen based on earlier reports of a burst nucleation event around 250 °C.^{22,23} Interestingly, these modifications induced a NW morphology (Figure 3.3.2.1a). Clearly visible lattice fringes in the HRTEM image suggested good crystallinity of the NWs (Figure 3.3.2.1b). The calculated interfringe distance was closely related to (400) crystal plane of maghemite crystal structure. The XRD scan showed 2θ peaks at 35.1°, 41.4°, 50.4°, 63.1°, 67.5°, 74.4°, and 88.7°. The peaks corresponded closely to (220), (311), (400), (422), (511), (440), and (533) maghemite crystal planes. A magnetization versus applied magnetic field measurement (*M-H*) showed ferromagnetic behavior of the NWs. The lower saturation magnetization of the NWs (60 emu/g), compared to bulk maghemite (78 emu/g) was likely caused by the surfactant coating.

Curiously, a few spherical NPs are also present in the NWs prepared by the above method. To obtain pure NWs and to understand their growth mechanism, we conducted a time dependent study at different reaction times (1, 2.5, and 5 h), keeping all other parameters constant. Mostly spherical NPs (diameter, 12 nm) with a few 50 nm long NWs were observed at 1 h reaction time (Figure 3.3.2.2a). At the normal reaction time of 2.5 h, many NWs (100 nm long) were formed, but a few spherical NPs remained (Figure 3.3.2.2b). When the reaction time was increased to 5 h,

spherical NPs almost disappeared, while the NWs grew significantly longer (200 nm, Figure 3.3.2.2c).

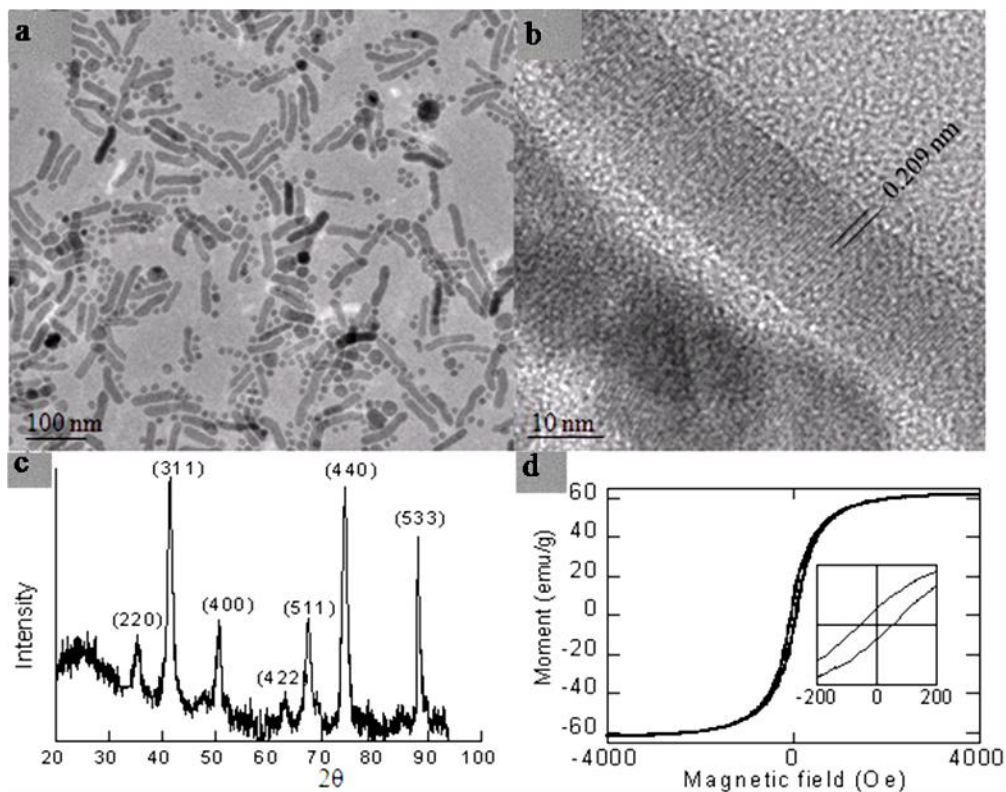


Figure 3.3.2.1. Iron oxide NWs: (a) bright-field TEM, (b) HRTEM, (c) XRD, and (d) M - H curve.

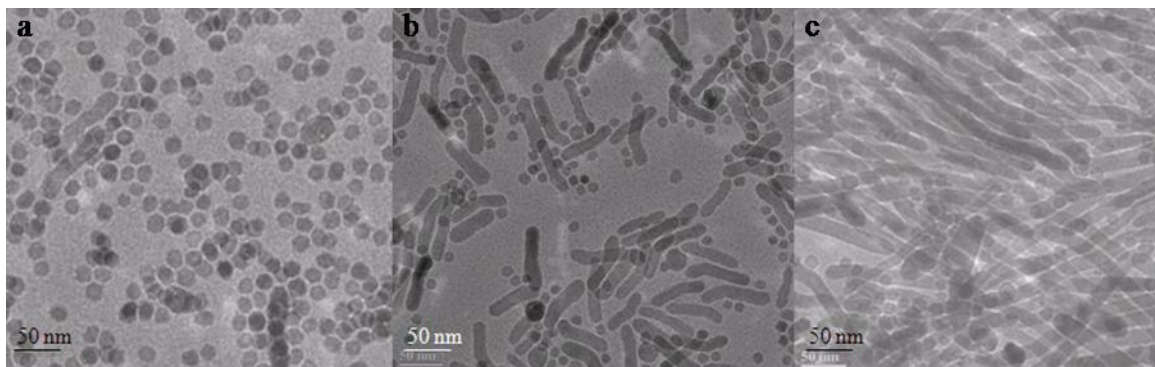


Figure 3.3.2.2. TEM image of iron oxide NWs at different reaction times: (a) 1 h, (b) 2.5 h, and (c) 5 h

The results suggested aggregation of spherical iron oxide NPs to finally form the highly crystalline NWs (Figure 3.3.2.3). Figure 3.3.2.3a shows superparamagnetic iron oxide NPs

during early reaction stage. The spherical NPs aggregated in a linear chain with reaction time, as seen from the TEM image of a NW in the intermediate stage of formation (Figure 3.3.2.3b). Aggregation of the spherical NPs was supported by similar diameters of the NWs and the NPs. An increased amount of the weak binding ligand, TOPO, played an active role in the one-dimensional aggregation. The dynamic behavior (constant attachment-detachment) of TOPO at the elevated reaction temperatures, facilitated aggregation of the neighboring spherical NPs. Additionally, the three bulky arms of TOPO prevent it from forming a compact surface coating, which leaves open spots for aggregation on the NP surfaces.^{24,25} The aggregated structures transformed into the crystalline, ferromagnetic NWs with reaction time (Figure 3.3.2.3c).

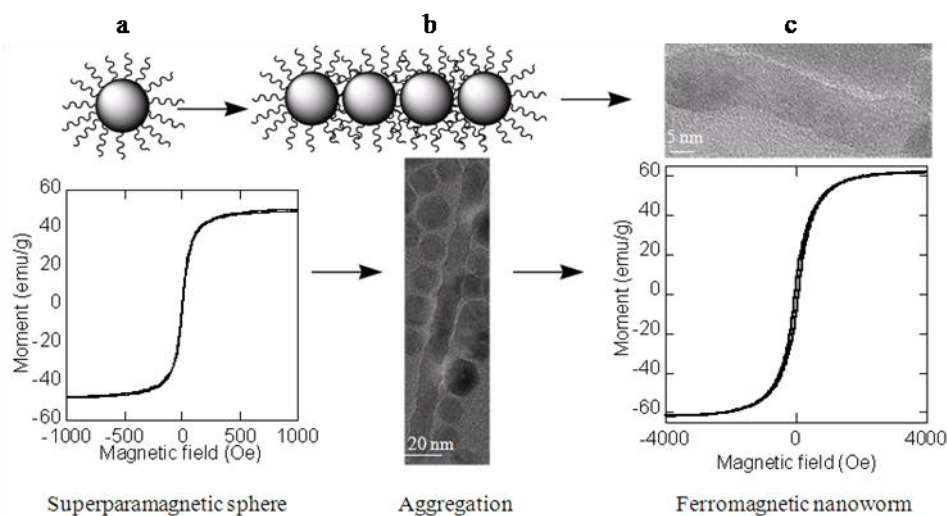


Figure 3.3.2.3. Formation mechanism of iron oxide NWs: (a) superparamagnetic iron oxide NPs, (b) aggregation of spherical NPs, and (c) ferromagnetic iron oxide NWs.

Conclusion

In summary, crystalline iron oxide NWs with tunable length were synthesized using a modified “heat-up” method. Based on our time-dependent studies, the NWs formed from aggregation of individual iron oxide NPs. The weak binding ligand, TOPO played a key role in

the aggregation process. Ongoing efforts are directed to synthesize thin, superparamagnetic NWs with smaller sized NP seeds.

3.3.3 Iron Oxide Nanoplates and Nanoflowers

Experiment

Synthesis of the precursor, iron oleate complex

The iron oleate complex was prepared by interacting ferric chloride (6.5 g) and potassium oleate (96.2 g) in a solvent mixture (hexane/water/ethanol) following a similar procedure reported elsewhere.¹ After phase separation, the hexane phase containing the iron oleate complex was washed with de-ionized water to remove the by-products, and stored as a precursor, where the hexane accounted for 6.5 wt%. Here, the iron oleate hexane solution was used as a precursor for easy operation, instead of well-dried iron oleate waxy paste. The presence of hexane, a low-boiling temperature solvent, allows for controlling the reaction temperature at 290 °C, instead of above 317 °C for nanosphere synthesis.

Synthesis of the iron oxide nanoplates and nanoflowers

The iron oxide nanoplates and nanoflowers were synthesized via a similar procedure with the only difference in the amount of TOPO, a weak bound ligand to iron. Specifically, iron oleate precursor (1.82 g) in 1-octadecene (13 mL) was heated at 290 °C for an hour in the presence of oleic acid (0.1 mL) and TOPO (0.2 g-nanoplates or 1 g-nanoflowers). After synthesis, the nanoparticles were centrifuged out of solution for further characterization.

Mechanistic study of the nanoplate and nanoflower formation

First, time-dependent growth studies for both samples were conducted by taking samples out of reaction solution at various time intervals (20 min, 30 min, 40 min, and 1h). Further, to

elucidate the growth mechanism of nanoplate, potassium ethoxide was prepared and injected into the reaction to understand the role of $\text{CH}_3\text{CH}_2\text{O}^-$. In contrast, for nanoflower formation, hexane, extra precursor, or additional TOPO were injected into the reaction.

Characterization

The size and morphology of the iron oxide nanoplates and nanoflowers were examined on a FEI Tecnai F-20 TEM. The nanoplate thickness was determined by the TEM tilting experiment. The x-ray diffraction patterns of the nanoplates and nanoflowers were collected on a Bruker AXSD8-Advanced XRD using a Co source (K_α , $\lambda = 1.79 \text{ \AA}$). The magnetic properties of these nanoplates and nanoflowers were measured using an AGM at room temperature.

Results and Discussion

We have shown that the weakly-bound ligand, TOPO, played an important role in the shape control of iron oxide NPs and subsequent surface modification. For instance, introducing a weak ligand molecule facilitated aggregation of iron oxide nanospheres into NWs.²⁶ It was also shown that the reaction temperature provided another effective means to tune the shape of iron oxide NPs based on the iron oleate decomposition behavior, as shown in the study of nanowhisker formation.¹⁵ Here, the importance of TOPO in controlling the nucleation event was further demonstrated. The presence of hexane, a low boiling temperature solution, allowed for controlling the reaction temperature at 290 °C, a temperature above the decomposition of all three oleate ligands, but below the burst nucleation event (310 °C). When TOPO/OA (1.67/1) was used, plate-like nanostructures about 18 nm in size were observed (Figure 3.3.3.1a). The nanoplate was highly crystalline as seen in the HRTEM image (Figure 3.3.3.1b), which was also supported by a dot pattern in the fast Fourier transformation (FFT) image (Figure 3.3.3.1b, inset). The interspacing shown in the HRTEM image corresponds to the (111) plane of the iron oxide

spinel structure. The inter-fringe distance was measured to be 0.483 nm, and closely corresponds to the (111) lattice plane of both maghemite and magnetite. The thickness of the thin plate was confirmed by a TEM tilting experiment ($30^\circ \alpha$ -tilt) to be about 3 nm (Figure 3.3.3.1c). Because of the thin morphology, these nanoplates have very large surface area, leading to a large component of the paramagnetic signal in the magnetic measurement (Figure 3.3.3.1d). Unfortunately, the XRD pattern could not provide a conclusive confirmation of the crystal phases of the iron oxide NPs due to size broadening and the similarity between magnetite and maghemite (Figure 3.3.3.1e).

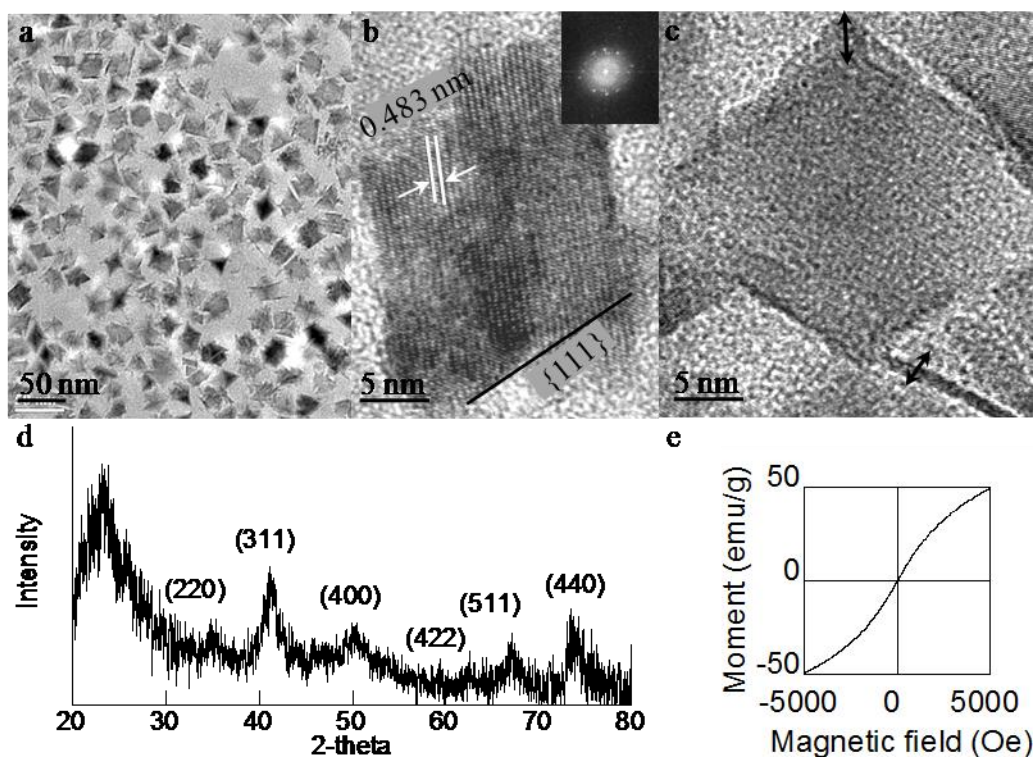


Figure 3.3.3.1. Iron oxide nanoplates: (a) TEM image, (b) HRTEM, fast Fourier transformation (FFT) image (inset), (c) HRTEM after $30^\circ \alpha$ -tilt (d) XRD, and (e) M - H curve.

Interestingly, under a similar reaction condition, nanoflowers (~ 20 nm) were produced by simply increasing the TOPO to OA ratio 5 times (Figure 3.3.3.2a). The HRTEM clearly indicated that the nanoflowers consisted of many small (~ 5 nm), single crystalline iron oxide

nanocrystals (Figure 3.3.3.2b). This single crystalline structure was also supported by the dot pattern of the FFT image (Figure 3.3.3.2b, inset). The magnetic properties of these nanoflowers showed very similar M - H curves to small magnetic NPs with high saturation field (Figure 3.3.3.2c). Similar to the nanoplates, the XRD pattern of the nanoflowers exhibited typical peaks of iron oxide, but it was difficult to confirm magnetite or maghemite due to their similar crystal structures (Figure 3.3.3.2d).

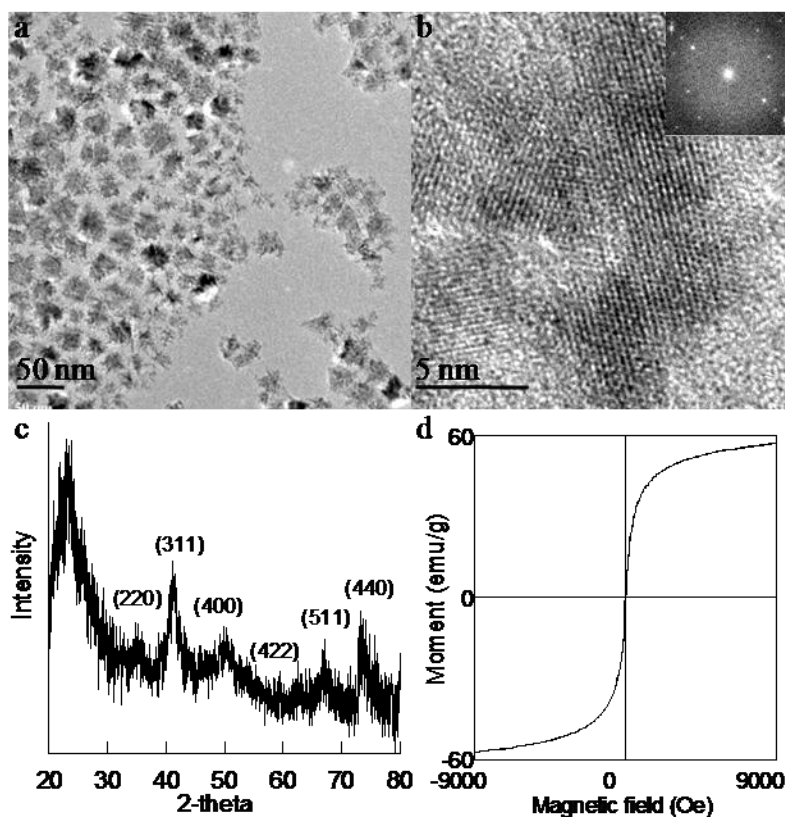


Figure 3.3.3.2. Iron oxide nanoflowers: (a) TEM image, (b) HRTEM, fast Fourier transformation (FFT) image (inset), (c) XRD scan, and (d) M - H curve.

To understand the growth mechanism of nanoplates and nanoflowers, time-dependent growth studies for both samples were conducted by taking samples out of the reaction solution at various time intervals (20 min, 30 min, 40 min, and 1h). For the nanoplate reaction, small, non-spherical iron oxide nuclei (4 nm) were observed after 20 min (Figure 3.3.3.3a). After 30 min,

plate-like nanostructures with a wide size distribution appeared, indicating the onset of a particle growth phase to reduce surface energy (Figure 3.3.3.3b). The uniform iron oxide nanoplates were the major product after a 40 min reaction (Figure 3.3.3.3c). Monodisperse iron oxide nanoplates of size 18 nm were formed (Figure 3.3.3.3d) after 1 h reaction. It was hypothesized that the nanoplates were formed through a diffusion-controlled growth and size focusing process based on the time-dependent study.

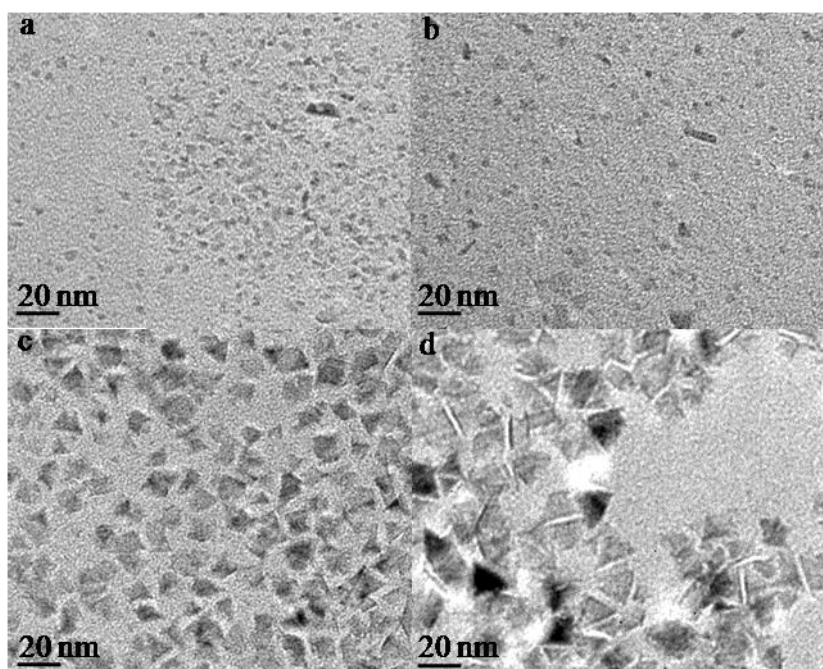


Figure 3.3.3.3. Time-dependent nanoplates: (a) 20 min, (b) 30 min, (c) 40 min, and (d) 1 h.

The additional ligands in the system played a key role for the formation of the plate morphology. Several reactions were performed with an additional ligand (hexane, potassium ethoxide, and sodium oleate) and a well-dried precursor that is known to produce iron oxide spheres to confirm the ligands that influence the growth process. The three components, hexane, potassium ethoxide, and sodium oleate could be present, according to the precursor preparation process. Figure 3.3.3.4 shows the nanostructures produced with the injection of hexane (Figure 3.3.3.4a), potassium ethoxide (3.3.3.4b), and sodium oleate (3.3.3.4c). The nanostructure

morphology suggested that the presence of a small amount of potassium ethoxide as the third ligand facilitated the formation of nanoplates.

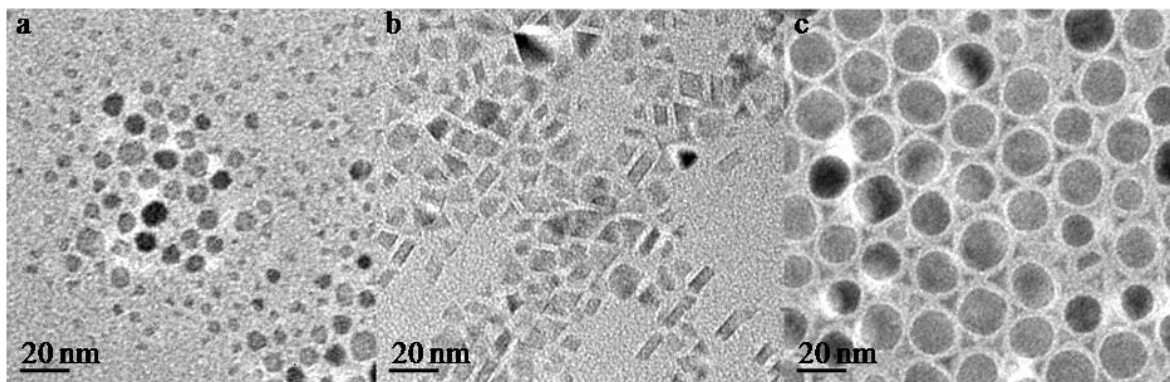


Figure 3.3.3.4. TEM image of iron oxide NPs formed after injections of: (a) hexane, (b) potassium ethoxide, and (c) sodium oleate.

Interestingly, the time-dependent studies of the nanoflowers showed a totally different growth pathway, as shown in Figure 3.3.3.5. Very small iron oxide nuclei (< 2 nm) appeared at 20 min (Figure 3.3.3.5a). As the reaction proceeded to 30 min (~ 285 °C), only a few nanoflowers (~ 20 nm) were formed. The sample mostly consisted of low crystalline aggregates of small NPs (Figure 3.3.3.5b). Iron oxide nanoflowers were the main product after a 40 min reaction, although a few small NPs were present (Figure 3.3.3.5c). Nanoflowers of size ~ 25 nm with good crystallinity, and size distribution were obtained at 1 h reaction time (Figure 3.3.3.5d).

The nanoflower formation could result from the high concentration of nuclei, induced by the high percentage of the weakly-bound ligands. This has been observed in other systems. The high concentration of nuclei only allowed the nuclei to grow to a certain size, and the monomers were used up. Subsequently, the high energy of the small nanocrystals led to aggregation to minimize the surface energy. Three reactions were designed to further confirm this growth mechanism (Figure 3.3.3.6): (1) TOPO injection to a typical nanosphere reaction to confirm that the TOPO will cause high concentration of nuclei and subsequent aggregation growth process, (2) injection

of hexane, which has been shown to induce nuclei aggregation due to local concentration increase from the evaporation of hexane,²⁷ and (3) injection of excess precursor to induce multiple nucleation events. Injection of TOPO induced a large number of nuclei in the reaction, suggested by the small NPs seen in the bright field image (Figure 3.3.3.6a). However, aggregated flower-like NPs formed with hexane (Figure 3.3.3.6b). The evaporation of hexane during the synthesis could facilitate multiple nucleation events, followed by aggregation of the small nuclei. When multiple nucleations were forced with iron oleate injections, the flower-like NP morphology was clearly visible, although the size of the NPs was larger (Figure 3.3.3.6c).

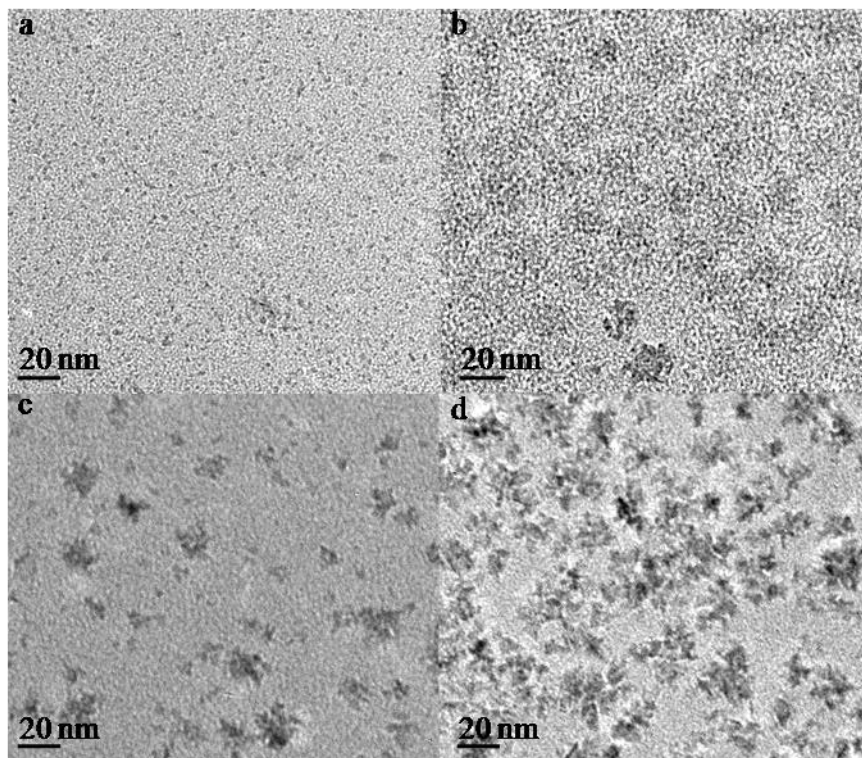


Figure 3.3.3.5. Time-dependent nanoflowers: (a) 20 min, (b) 30 min, (c) 40 min, and (d) 1 h.

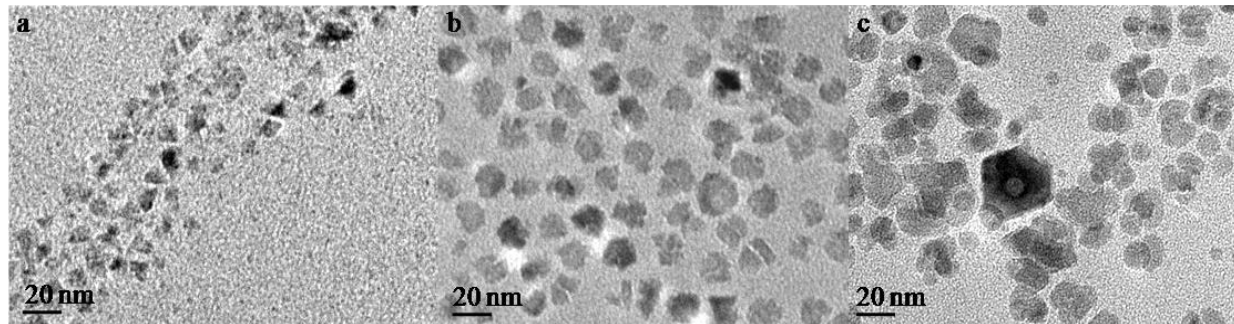


Figure 3.3.3.6. TEM image of iron oxide NPs formed after injections of: (a) TOPO, (b) hexane, and (c) iron oleate.

The above results indicated that although the same precursor as that of the nanoplates was used for the synthesis of nanoflowers, a very different reaction mechanism was observed. The nanoplates followed a surfactant controlled growth, characteristic of systems with low nuclei concentration. In the nanoflower reaction, more nuclei were formed using a higher percentage coverage of weak binding ligand, TOPO.

Two different growth pathways were rationalized for the nanoplates and nanoflowers based on the detailed mechanistic studies. The nanoplate morphology was induced by the $\text{C}_2\text{H}_5\text{O}^-$ anion, which provided different surface stabilization compared to OA/TOPO. The nanoflowers did not show a surfactant controlled growth because a higher percentage of TOPO led to more nuclei. The iron oxide nanoflowers resulted from multiple nucleation events, and oriented attachment of the small NPs. The reflux of volatiles induced changes in local monomer concentrations that led to multiple nucleations. Additionally, inadequate surface stabilization provided by TOPO facilitated the oriented attachment in nanoflowers.

The reproducibility of iron oxide nanoplate and nanoflower syntheses was investigated over a batch of repeat reactions. Figure 3.3.3.7a plots the average size of the nanoplates over ten repeating reactions, with ± 2 nm standard deviation error bars. The longest edge of the nanoplate was considered for measurement. Almost each reaction fell within this range of standard

deviation. Figure 3.3.3.7b shows the average size of the iron oxide nanoflowers (22 nm) for five synthetic reactions repeated under similar conditions. The reactions showed ± 2 nm standard deviation, proving good repeatability. The synthesis of both the iron oxide nanoplates and nanoflowers, described above were reproducible in terms of NP size and shape, based on these results.

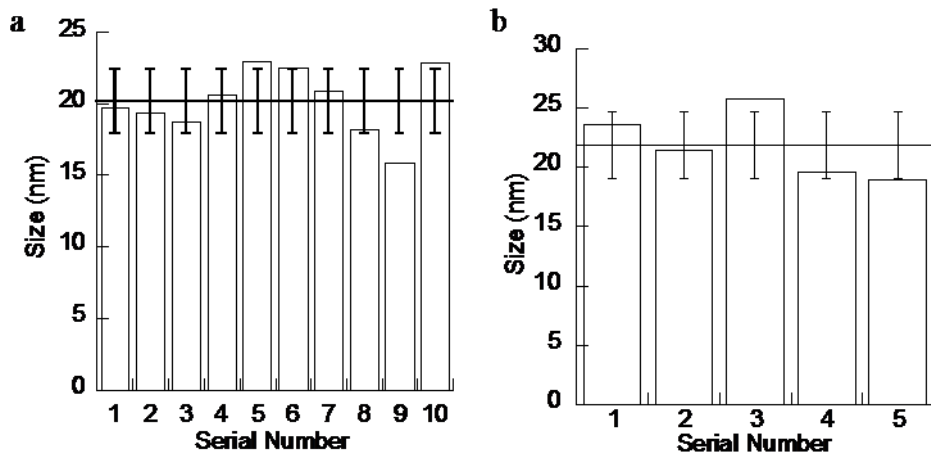


Figure 3.3.3.7. Column graphs showing reproducibility: (a) nanoplate reactions, and (b) nanoflower reactions.

The nanoplates, nanoflowers, NWs, and nanowiskers were used for multiple Pt attachment reactions in organic solvent, using 360:1 Pt precursor to iron oxide NP molar ratio. The iron oxide nanoplates were most suitable for the multiple Pt NP attachments (Figure 3.3.3.8a). The attachments were visible from the dark image contrast on the nanoplate surfaces. The Pt NPs of size ~ 2 nm attached to the corners and sharp edges of the nanoplates (Figure 3.3.3.8b) based on the HRTEM. The reaction was more reproducible, compared to the organic route attachment reactions on spherical NP surfaces. The sharp corners of the nanoplates likely provide more active surfaces for heterogeneous nucleation of Pt NPs.

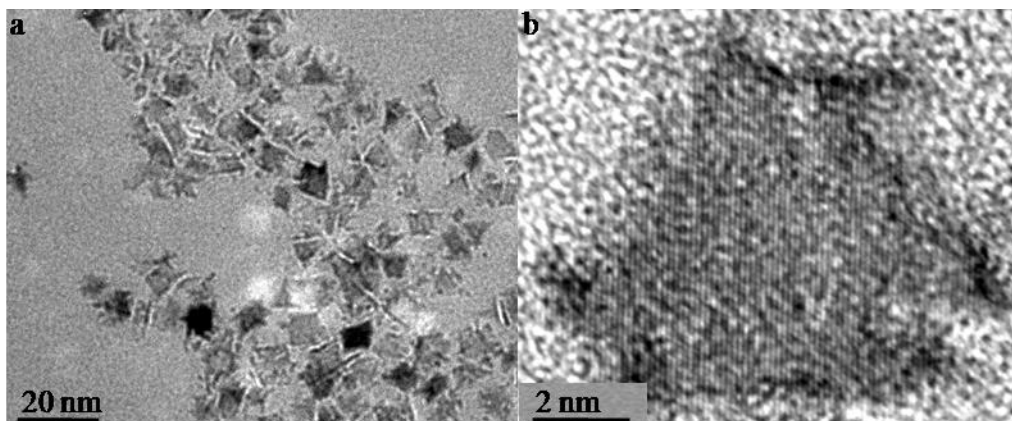


Figure 3.3.3.8. Multiple Pt-attached plate-like iron oxide NPs synthesized in an organic solvent: (a) TEM image, and (b) HRTEM image.

Conclusion

Highly crystalline iron oxide nanoplates and nanoflowers were synthesized with excellent reproducibility following a slightly modified “heat-up” method. The time-dependent studies and control experiments indicated that the nanoplates were formed from preferential surfactant binding. Here, $\text{C}_2\text{H}_5\text{O}^-$ played a significant role as a third ligand molecule along with OA/TOPO. However, the nanoflowers were facilitated by multiple nucleations from volatile reflux, followed by oriented-attachment of the iron oxide NPs. Here, a high nuclei count induced by the higher percentage coverage of weakly-bound TOPO prevented surfactant controlled growth. In conclusion, this study provided a simple, repeatable synthesis of iron oxide nanoplates and nanoflowers, and insights into their detailed mechanistic pathways. The iron oxide nanoplates facilitated easy Pt NP attachments via an organic route. The sharp corners of the nanoplates could likely provide active nucleation sites for small the Pt NPs.

3.4 Water Soluble Iron Oxide Nanoparticles

The iron oxide NPs with toxic organic surfactant coating cannot be used for bio-applications.

Therefore, the Pt attached NPs in the organic solvent were transferred to an aqueous phase via a ligand exchange process. The reaction parameters for effective phase exchange were investigated with iron oxide NPs. The multiple Pt attached NPs were then transferred to the aqueous phase using these reaction conditions.

Experiment

The as-synthesized NPs were precipitated out of solution and vacuum-dried to completely wash off the organic surfactant layer. The dried powder sample was dissolved well in chloroform under sonication to form the stock solution (5 mg/mL).²⁸ The biocompatible polymer solution, freshly prepared polyacrylic acid (PAA, M_w, 100,000) in dimethylsulfoxide (DMSO, 4 mL) was mixed with the NP stock solution and DMSO (45 mL) under sonication (15 min). The homogeneous solution containing the NPs and PAA was reacted at 20 °C in the shaker (24 h) for phase exchange. The iron oxide NPs in solution were magnetically separated and redispersed in DI water. The pH was adjusted to ~ 7-8 using one drop of NaOH solution to stabilize the anionic PAA polymer.

Characterization

FEI Tecnai F-20 TEM was used to study the size and morphology of the NPs. The hydrodynamic diameter of NPs was investigated on a Malvern Zetasizer Nano DLS.

Results and Discussion

The iron oxide NPs capped with OA/TOPO were mixed with the biocompatible polymer, PAA for phase transfer. In a typical synthesis, the organic surfactants were removed in several washes with chloroform and acetone, prior to mixing (24 h) with PAA and DMSO. The dipolar solvent, DMSO can dissolve both the organic NPs and the hydrophilic ligand molecules, and facilitates good phase transfer. During mixing, the hydrophilic PAA gradually capped the iron

oxide surfaces (molar ratio of exchanged ligand-to- NP surface Fe atoms = 5:1). The carboxylic groups of PAA bound to the iron oxide surface. The remaining functional groups at the other end of the polymer protruded out from the NP surface to make them water soluble. A good wash of the exchanged NPs in DI water could prevent aggregation caused by hydrogen bonding between the polymer coatings of adjacent NPs. Figure 3.4.1a is a TEM image of ligand exchanged iron oxide NPs coated with PAA. The NPs showed negligible aggregation. However, the electron beam transparent polymer coating could not be viewed in the TEM. Therefore, the hydrodynamic diameter of the phase exchanged NPs were investigated with a DLS. The DLS measurements suggested an increase in the hydrodynamic diameter of the NPs from 12 nm in the organic phase to 40 nm in water solution ($\text{pH} \sim 7$) (Figure 3.4.1b). This is likely from the long-chain PAA polymer coating. However, the NPs were still well below the macrophage clearance limit. The aqueous phase iron oxide NPs showed good stability because no precipitation from NP aggregation was observed even after 30 days (Figure 3.4.1c).

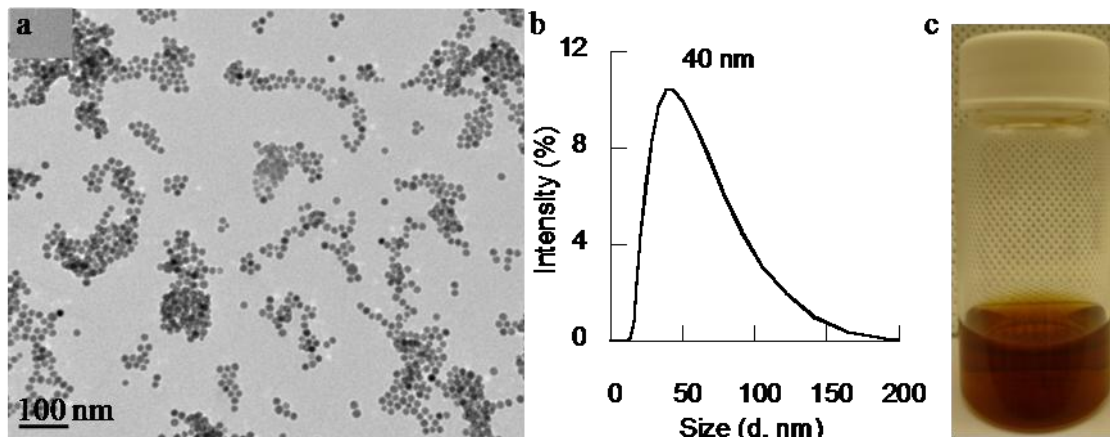


Figure 3.4.1. PAA capped water soluble iron oxide NPs: (a) bright-field TEM, (b) DLS plot, and (c) aqueous NP solution after 30 days.

A ligand exchange was performed on the multiple Pt attached iron oxide NPs from organic route to make them water soluble for bio-applications. Figure 3.4.2a shows a bright-field image

of the NPs after phase transfer. The NPs showed minimum aggregation based on this image. In the HRTEM, the small dark spots on the iron oxide surface suggested no loss of attached Pt NPs after phase exchange (Figure 3.4.2a, inset). This showed good integrity of the NPs because they could withstand the long periods of sonication involved in the surfactant exchange. The hydrodynamic diameter of the aqueous phase NPs was 60 nm, likely from slight aggregation (Figure 3.4.2b).

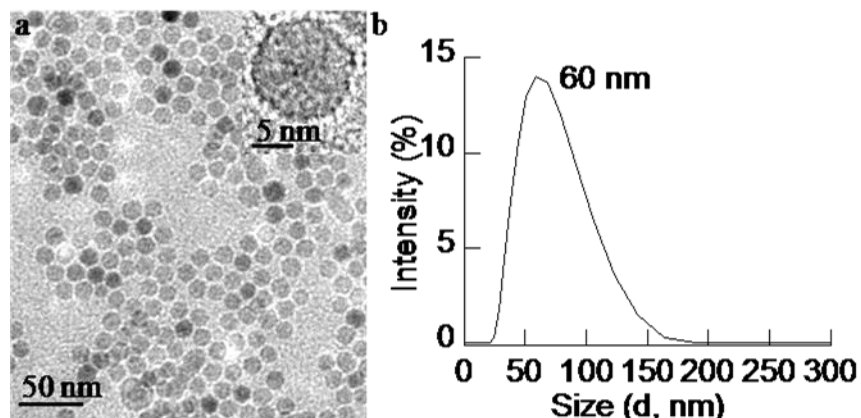


Figure 3.4.2. Multiple Pt-attached iron oxide NPs (organic route) after surfactant exchange: (a) TEM image, HRTEM (inset), and (b) DLS plot.

Conclusion

Iron oxide NPs from the modified “heat-up” method could be successfully transferred to an aqueous phase via a ligand exchange with biocompatible polymer, PAA. The same process could make the multiple Pt-attached NPs water soluble. The water soluble NPs could now be used for potential bio-applications.

3.5 Platinum Attached Iron Oxide Nanoparticles via Aqueous Route

The organic route for Pt attachments formed small Pt NPs well protected inside the biocompatible polymer surrounding the whole NP. An aqueous synthetic route was designed for

better accessibility of the small Pt NPs for *in vitro* DNA interaction studies (Figure 3.5.1).²⁹

First, the iron oxide NPs were transferred to an aqueous phase via a ligand exchange process (Section 3.4). Next, the small Pt NPs were deposited on the biocompatible polymer capping the iron oxide seeds. The surface Pt NPs could easily interact with the therapeutic target, such as DNA.

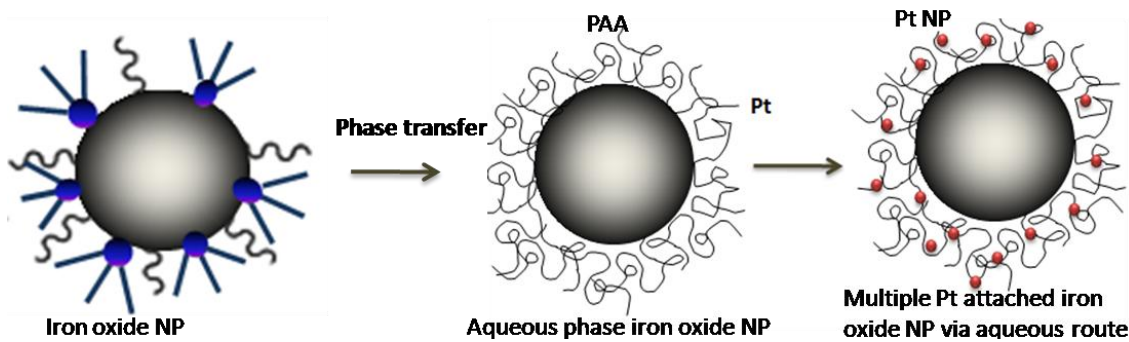


Figure 3.5.1. Multiple Pt NP attachments via an aqueous route.

Experiment

In a typical room temperature synthesis, iron oxide NPs (PAA coated, 3 µg/mL) in water were mixed with H₂PtCl₆ water solution (pH 7, 0.5 mg/mL) at 1:5000 molar ratio. The well mixed solution was subjected to UV radiation for 0.5, 1, 1.5, and 2 h, respectively, to deposit the Pt NPs on PAA-coated iron oxide seeds. A UVGL-55 handheld UV lamp (6 watt, 365 nm) was the UV radiation source. The resultant solution was centrifuged for 5 min at 15,000 rpm to remove the free Pt NPs.

Characterization

The size and morphology of the integrated NPs were examined on a FEI Tecnai F-20 TEM. High-angle annular dark-field (HAADF) imaging was used to confirm the Pt attachments as shown in earlier sections. The Pt-iron oxide NPs in aqueous solution were directly dropped on the TEM grids without any treatment.

Results and Discussion

The PAA coated iron oxide seeds were used for growing multiple Pt NPs via an aqueous route. PAA ligand is known to provide an effective surface capping for both iron oxide³⁰ and Pt NPs³¹. H₂PtCl₆, the liquid Pt precursor, was chosen because it could form a homogeneous mixture with the iron oxide NP solution. However, the pH of H₂PtCl₆ must be adjusted (pH 7) to prevent the iron oxide NPs from dissolving in the highly acidic Pt precursor. Here, a UV reduction source could control Pt NP growth through different exposure times. The metal salts are reduced to metallic NPs by solvated electrons and free radicals under irradiation.³² A radiation time-dependent study suggested the optimal exposure time (1 h) for 2 nm sized Pt NPs. Few Pt NPs were formed at 0.5 h, but heavy aggregation of Pt NPs was observed for longer UV exposures. A 5000:1 molar ratio of Pt precursor to iron oxide seeds was used for all these reactions to obtain a high density of Pt attachments on iron oxide seeds.

Figure 3.5.2a shows a representative Pt attached iron oxide NP sample using 5000:1 Pt precursor to seed molar ratio at 1 h UV exposure. The bright field image shows thickness or atomic number (Z) based contrast. Therefore, the higher Z Pt NPs appear darker than the iron oxide seeds. Based on our bright-field results, a high density of Pt NPs were deposited on the iron oxide seeds. The HRTEM image suggested good crystallinity and uniform size (2 nm) of the Pt NPs (Figure 3.5.2b). Additionally, the gap between the Pt and iron oxide NPs showed that the Pt NPs nucleated on the polymer surrounding the iron oxide seeds, rather than the iron oxide surfaces. High angle annular dark-field (HAADF) imaging was used to investigate if free Pt NPs were present in the sample. The annular detector for HAADF is negligibly affected by defocus and sample size (Bragg's reflections) because it operates at very high angles to detect primarily

the incoherent thermal diffused scatterings. The HAADF image of Pt-iron oxide NPs (Figure 3.5.2c) clearly shows the absence of any unattached Pt NPs.

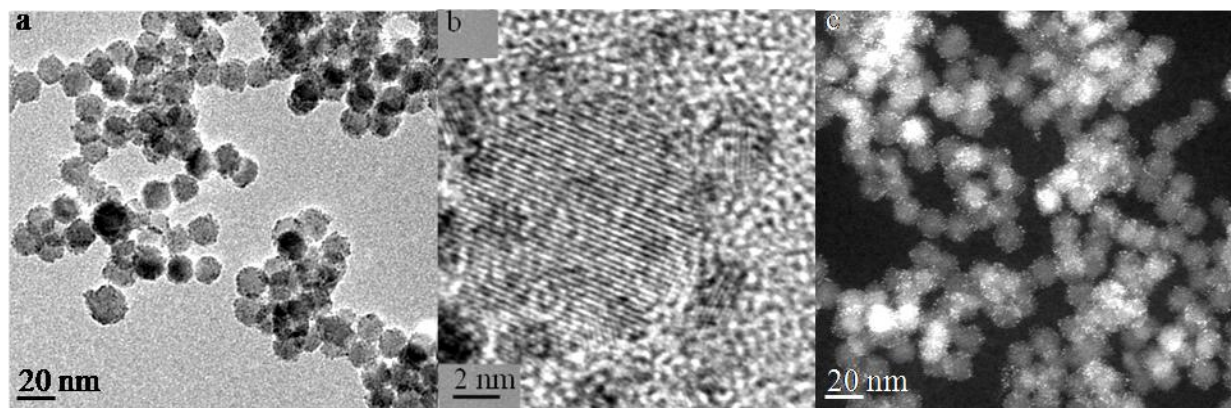


Figure 3.5.2. Aqueous phase Pt-iron oxide NPs: (a) TEM image, (b) HRTEM image, and (c) HAADF image.

Conclusion

In conclusion, a simple and reproducible synthesis of multiple Pt attached iron oxide NPs in aqueous phase was reported. The HRTEM and HAADF image confirmed high quality Pt attachments on the polymer coating surrounding the iron oxide seeds. Additionally, the size of Pt NPs could be controlled to 2 nm using different UV reduction times.

3.6 DNA Interaction of Platinum Attached Iron Oxide Nanoparticles

DNA interaction of the NPs was investigated to prove the research hypothesis that small Pt NPs attached to iron oxide surfaces could interact with the DNA. The multiple Pt attached NPs synthesized via an aqueous route and plasmid DNA were used as models for the DNA interaction studies.

Experiment

Plasmid DNA (63 µg/mL) was extracted from K91 bacteria via a standard protocol using a

miniprep DNA extraction kit (Invitrogen). The plasmid (4 μ L) was incubated with 8 μ L of Pt-iron oxide NPs at 37 °C for 0.5, 4, and 24 h, keeping all other parameters constant. The non-specific interaction of the Pt-iron oxide NPs was studied by incubating 8 μ L NPs with bovine serum albumin (BSA, 4 μ L) and glutathione (GSH, 4 μ L) at 37 °C for 4 h.

Characterization

The size, morphology, and chemical composition of the Pt-iron oxide NPs before and after DNA interaction were examined on a FEI Tecnai F-20 TEM and a JEOL-7000 SEM. The hydrodynamic diameter of the NPs was measured using a Zetasizer Nano (Malvern) DLS.

Spectra 220 FS (Varian) AAS was used to analyze Pt and Fe concentration changes in the NP solution after DNA interaction. The NP solution was magnetically separated after 4 h of DNA interaction, to remove any free Pt NPs. All unknowns were prepared in 10 mL nanopure water containing one drop (0.01 mL) HCl (1%). The Pt standards used contained freshly prepared solutions of 0.8 mg/mL, 0.16 mg/mL, 0.11 mg/mL, and 0.08 mg/mL H_2PtCl_6 in nanopure water. The Fe standards (0.005 mg/mL and 0.0025 mg/mL) were freshly prepared by serial dilutions of Fe atomic spectroscopy standard stock solution. Calibration curves for both Pt and Fe ions were linear with $R > 0.98$. The AAS was operated at 345-450 kPa compressed air flow, and an acetylene output pressure of 85-100 kPa.

The interaction of the plasmid with Pt-iron oxide NPs was compared with control plasmid using agarose gel electrophoresis (Thermo Scientific). The electrophoresis was performed at 110 V. The gel was viewed under short wavelength UV light, and photographed subsequently.

Results and Discussion

The NP-DNA interaction was studied using agarose gel electrophoresis. Gel electrophoresis

has been shown to effectively isolate Au and Pt NP-conjugated DNA.^{33,34} Here, the gel electrophoresis studies suggested two types of interactions between the DNA (plasmid) and the Pt-iron oxide NPs when compared with the control DNA (Figure 3.6.1a). One band that ran slower (circled, lane 3 and 4) than the control DNA could be assigned to the plasmid directly interacted with the Pt NPs on the iron oxide seeds, where the integrity of the NP remained. The bright band (lane 3 and 4) migrated slightly faster compared to the supercoiled control plasmid, likely due to the added negative charge from the anionic polymer-coated iron oxide NPs. Therefore, the bright band could belong to the supercoiled DNA. The other band moving slightly faster (circled, lane 3 and 4) than the control was likely related to the DNA attached to the small Pt NPs. Figure 3.6.1b shows the two forms of NP-DNA interactions. Some of the plasmids covered the surface of the Pt-iron oxide NPs. This ligand-like behavior of the DNA has been reported earlier for single strand DNA mediated growth of Pt NPs.³⁵ In the second type of interaction, the small Pt NPs could fit perfectly into the DNA grooves. Earlier, small Au nanoclusters were reported to fit inside DNA grooves.³⁶ The strong affinity of the plasmid was sufficient to detach the small Pt NPs from the iron oxide seeds. The plasmid then stabilized the surface of the Pt NPs.

The DNA interactions at different incubation times (*e.g.*, 0.5, 4, and 24 h) were analyzed using TEM. Some Pt NPs were found to detach from the iron oxide seeds after a 0.5 h incubation with the plasmid (Figure 3.6.2a). Figure 3.6.2b shows the Pt-iron oxide NPs after 4 h DNA interaction. Here, the majority of the Pt NPs detached from the iron oxide NPs. The detached Pt NPs were barely seen in the bright field TEM image because of their small size. However, these small Pt NPs became visible under HAADF imaging (Figure 3.6.2c). The annular detector for HAADF is less affected by defocus and sample size (Bragg's reflections) because it operates at

very high angles to detect the incoherent thermal diffused scatterings. The free Pt NPs observed under HAADF were well dispersed with no signs of aggregation. In the absence of a capping molecule, the high surface energy of such small NPs (2 nm) induce heavy aggregation. Therefore, the well dispersed Pt NPs suggested possible surface stabilization by the DNA.

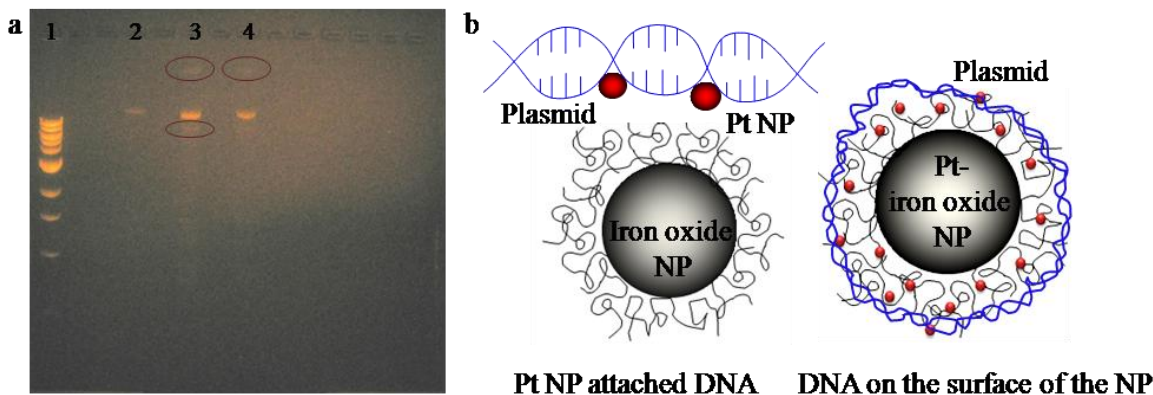


Figure 3.6.1. Pt-iron oxide NP-DNA interaction: (a) Gel electrophoresis; (lane 1) ladder, (lane 2) control plasmid, (lane 3) plasmid-NP interacted for 4 h, and (lane 4) plasmid-NP interacted for 0.5 h, and (b) DNA interaction mechanisms.

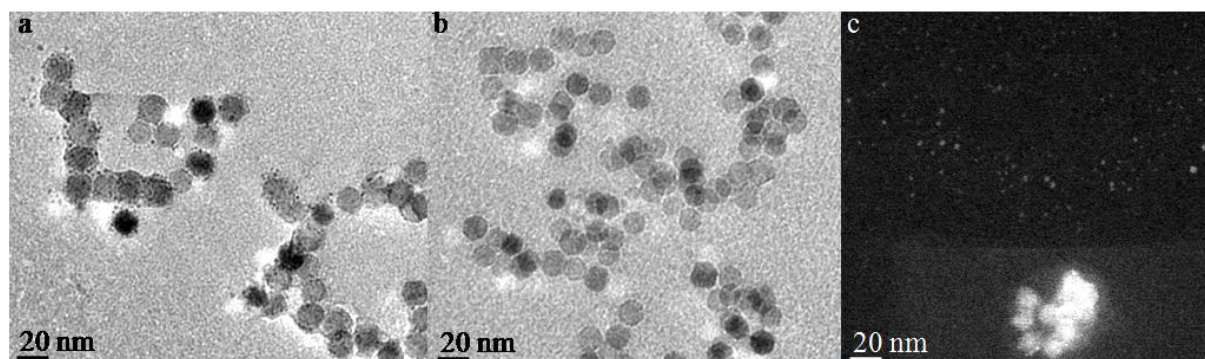


Figure 3.6.2. TEM images of Pt-iron oxide NPs incubated with plasmid for different times: (a) 0.5 h, (b) 4 h, and (c) HAADF image of sample b.

The hydrodynamic diameter of the Pt-iron oxide NPs before and after DNA interaction was monitored using DLS (Figure 3.6.3a).³⁷ The NP size was 40 nm before incubation with the plasmid. The size increased to 65 nm after DNA interaction, and a broad tail in the measurement

suggested DNA interaction on the NP surfaces. However, the free Pt NPs (~ 2 nm) were not detected by the DLS, likely due to their low percentage in the solution. The plasmid DNA used for the NP interactions showed a hydrodynamic diameter of 7 nm (Figure 3.6.3b). This observation suggested the conjugation of approximately 3 plasmids to the Pt-iron oxide NP surfaces based on the size increase of the NPs (~ 25 nm) after DNA interaction.

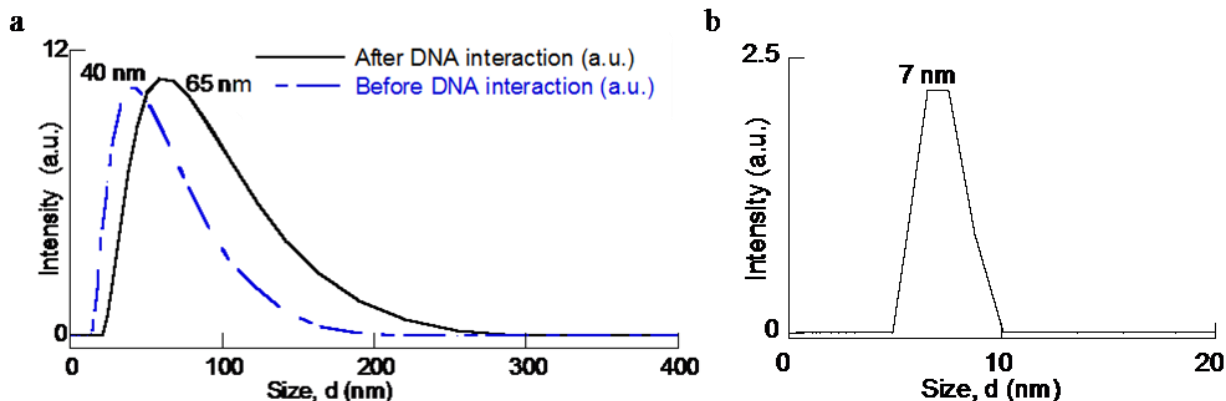


Figure 3.6.3. DLS plots of: (a) Pt-iron oxide NPs before and after DNA interaction and (b) plasmid DNA.

The energy dispersive x-ray (EDX) analysis was performed on the Pt-attached iron oxide NPs to estimate how much Pt was attached to the iron oxide seeds. First, TEM was used for the analysis. The atomic ratio of Pt:Fe was 5.4:1 before interaction with the DNA (Figure 3.6.4a). After DNA interaction this ratio reduced to 0.815:1 suggesting loss of Pt NPs from the iron oxide seed surfaces (Figure 3.6.4b). Additionally, phosphorus and nitrogen were detected on the NP surface after DNA interaction. This suggested presence of DNA on the NP surfaces because DNA consists of nitrogen bases on a phosphodiester backbone. The EDX was also performed using a SEM to support the TEM results. Here, the atomic ratio of Pt:Fe decreased from 0.17:1 before DNA interaction (Figure 3.6.5a) to 0.076:1 after interaction (Figure 3.6.5b). The decrease

in Pt was consistent with the loss of Pt from iron oxide seeds observed earlier. However, the low Pt percentage was likely because the small Pt (~ 2 nm) NPs were difficult to detect in the SEM.

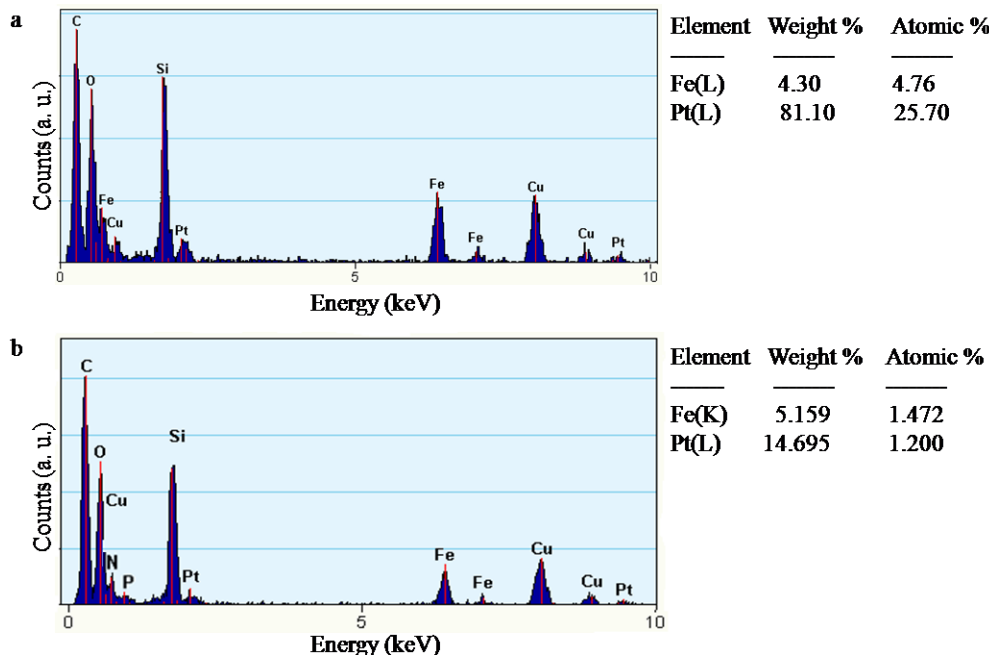


Figure 3.6.4. EDX of Pt-iron oxide NPs before and after DNA interaction using TEM: (a) before, and (b) after.

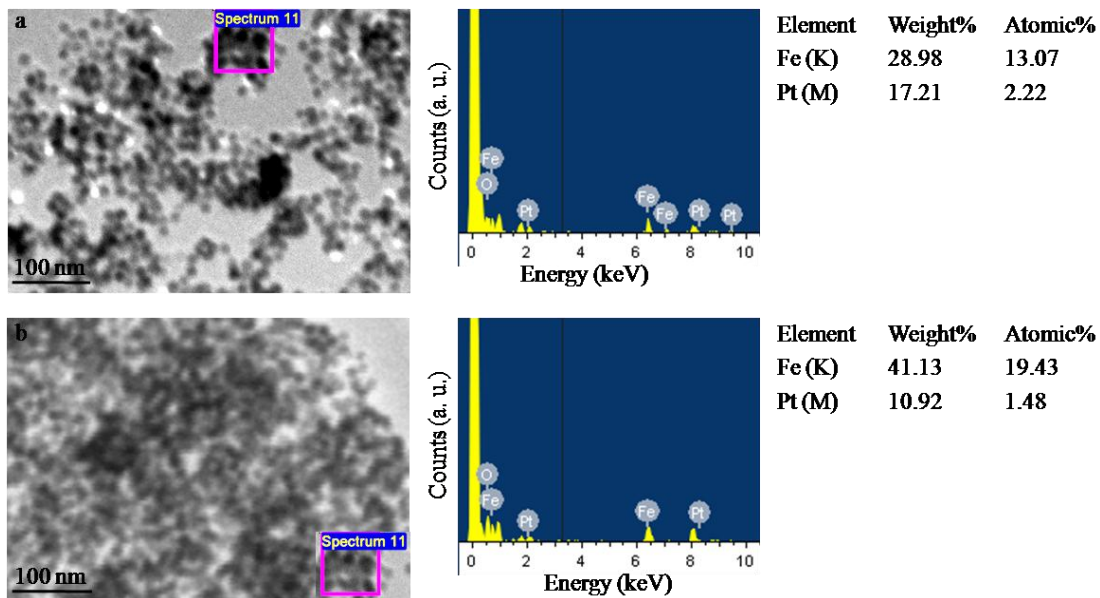


Figure 3.6.5. EDX of Pt-iron oxide NPs before and after DNA interaction using SEM: (a) before, and (b) after.

A quantitative estimate of the Pt NPs detached from the iron oxide seeds after DNA interaction was obtained using AAS. The AAS was used to measure the Pt ion and Fe ion concentrations in the sample solution before and after DNA interaction. Figure 3.6.6 shows the calibration curves for Pt ions (Figure 3.6.6a) and Fe ions (Figure 3.6.6b). 0.036 mg/mL Pt ion was present in the Pt-iron oxide NP sample before incubation with the DNA. The sample contained 0.00109 mg/mL of Fe ion. Therefore, the molar ratio of Pt ion to Fe ion was 10:1 before DNA interaction. Next, the sample was incubated with the plasmid (4 h), followed by a magnetic separation to remove the detached Pt NPs (supernatant solution). The Pt ion concentration of the magnetically-separated NPs, as obtained from the AAS was 0.039 mg/mL. The Fe ion concentration of this solution was 0.00273 mg/mL. Therefore, the molar ratio of Pt ion to Fe ion was 4:1 after DNA interaction. The results suggested decrease in the Pt concentration, following DNA interaction. Alternatively, the DNA extracted nearly half the Pt NPs attached to the iron oxide seeds. However, the rest of the Pt NPs remained attached to the seed surfaces.

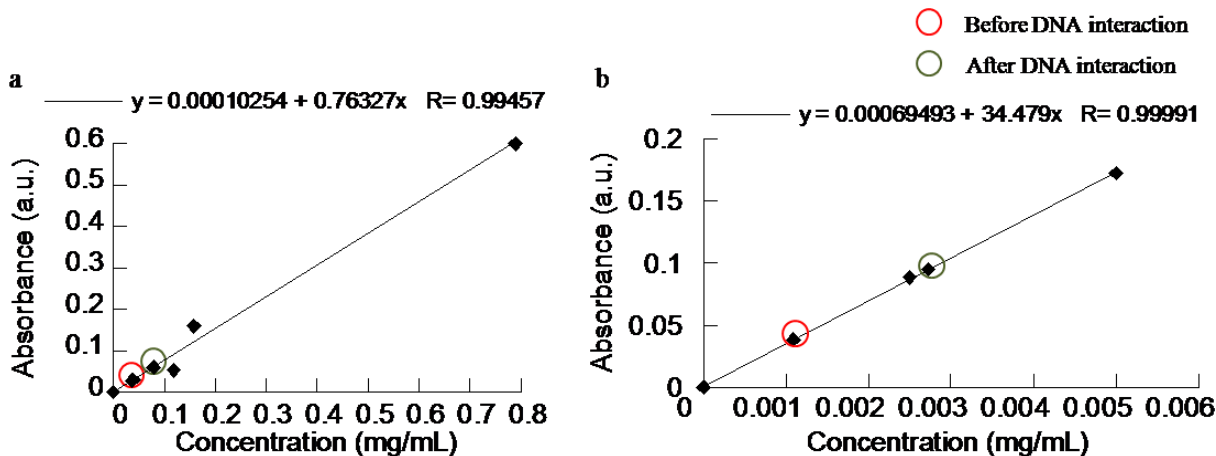


Figure 3.6.6. AAS calibration curves for ions: (a) Pt, and (b) Fe.

A major concern with these integrated nanostructures is the possibility of losing Pt NPs before reacting with the target (DNA). Therefore two model biological molecules were used to

interact with Pt-iron oxide NPs: GSH and BSA. GSH is a major antioxidant in the human body with concentrations up to 100 mM at certain locations.³⁸ It has a high affinity for Pt²⁺, and can limit the interaction of Pt complex anticancer drugs with tumor DNA.³⁹ Loss of Pt NPs from iron oxide surfaces was observed after 4 h incubation with GSH (Figure 3.6.7a). Serum albumin is the most abundant blood plasma protein in the human body. BSA is an easily available serum albumin derived from cows. Therefore, interaction of Pt-iron oxide NPs with serum albumin was investigated using BSA as a model. The loss of Pt NPs from iron oxide surfaces was observed following BSA interaction (Figure 3.6.7b). These results suggest that the interaction of Pt-iron oxide NPs is not specific to DNA. The high binding affinity of Pt NPs with DNA and GSH is consistent with earlier reports.⁴⁰ Non-target interactions of the NPs should be prevented for the potential therapeutic applications. The future efforts will focus on polymer encapsulation (*e.g.*, liposome) of the integrated NPs for effective surface protection, or utilizing the NPs synthesized via an organic route. These potential solutions are elaborated in Chapter 4.

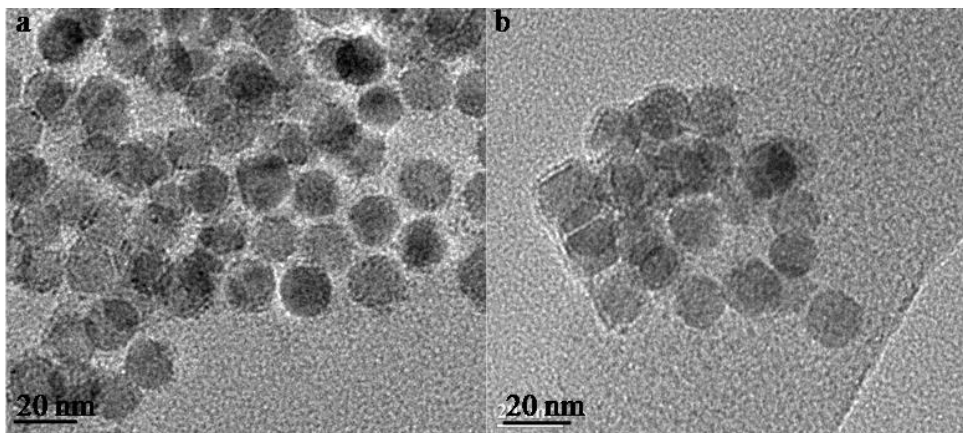


Figure 3.6.7. Interaction of Pt-iron oxide NPs with biomolecules: (a) GSH, and (b) BSA.

To reach the DNA molecules, the NPs have to be effectively internalized by cells. One of the most common cell internalization mechanisms is endocytosis. Depending on the ultimate localization of the NPs, the surrounding pHs can be totally different, such as 7.2 in cytosol and

4.6 in lysosome. Therefore, pH dependent stability experiments were performed to study the behavior of the NPs. The integrity of the Pt-iron oxide NPs was analyzed at different pH (*e.g.*, pH 4, pH 5, and pH 6). pH 4 was chosen because the stabilizing polymer for iron oxide seeds, PAA has a pK_a value of 4-4.5.⁴¹ PAA prevents aggregation of the iron oxide NPs via repulsion from adjacent charges. However, below the pK_a , protonation of the carboxylic acid groups of PAA could reduce the surface charge and stabilization capacity. The Pt-iron oxide NPs showed aggregation at pH 4, likely from the reduced surface charge of PAA (Figure 3.6.8a). However, no loss of Pt NPs from the iron oxide surface was observed. The Pt-iron oxide NPs was also observed at pH 5 and pH 6 because the pH range varies from ~ 6 for early endosomes to ~ 4.6 for lysosomes.⁴² NP aggregation observed at pH 5 and pH 6 suggested low surface protection by PAA in acidic pH (Figure 3.6.8b and c). However, there was no loss of surface Pt NPs. These results showed good pH stability of the Pt attachments.

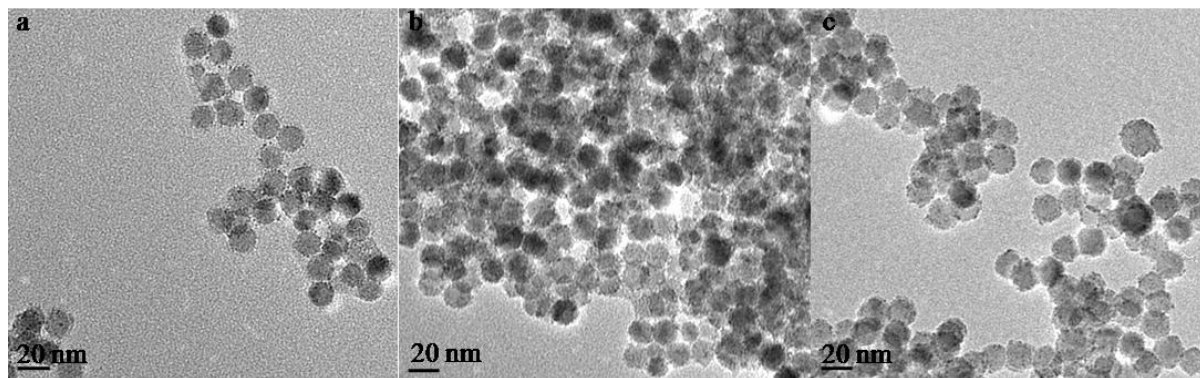


Figure 3.6.8. Aqueous Pt-iron oxide NPs in different pH: (a) pH 4, (b) pH 5, and (c) pH 6.

Conclusion

The DNA and NP interactions were studied using an agarose gel electrophoresis of the interacted plasmids. The Pt attachments were not lost in acidic pH. Two types of DNA-NP interactions were observed based on the electrophoresis. First, the DNA could detach Pt NPs from the iron oxide support. Second, the DNA directly linked to the integrated nanostructure

(Figure 3.6.9). DLS, TEM, SEM, and AAS analyses supported both types of DNA-NP interactions. We also demonstrated that the Pt NPs could interact with other biomolecules, such as GSH and BSA. In conclusion, our proof-of-concept experiments showed that Pt NPs on iron oxide surfaces were able to interact with the DNA.

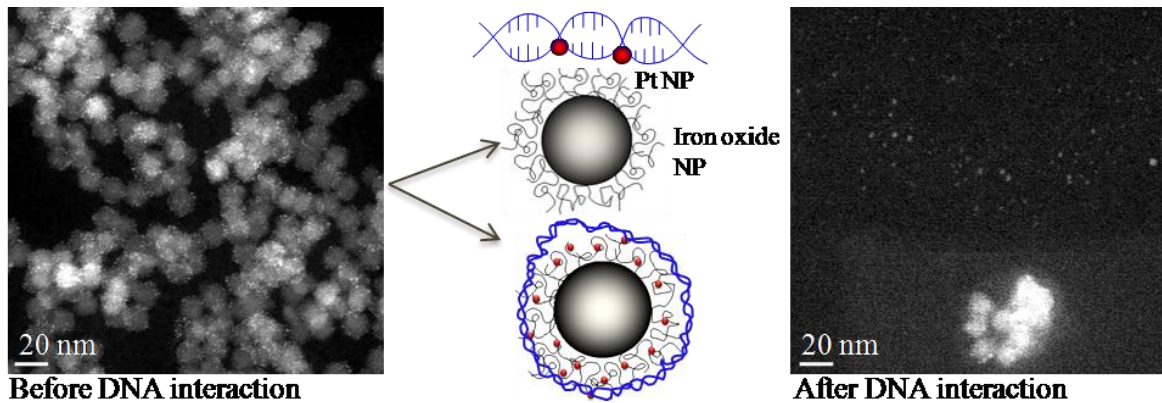


Figure 3.6.9. DNA interactions of Pt-iron oxide NP.

References

1. Palchoudhury, S.; Xu, Y. L.; An, W.; Turner, C. H.; Bao, Y. P., Platinum attachments on iron oxide nanoparticle surfaces. *Journal of Applied Physics* **2010**, *107* (9), 09B311 (1-3).
2. Gangopadhyay, S.; Hadjipanayis, G. C.; Dale, B.; Sorensen, C. M.; Klabunde, K. J.; Papaefthymiou, V.; Kostikas, A., Magnetic-properties of ultrafine iron particles. *Physical Review B* **1992**, *45* (17), 9778-9787.
3. Park, J.; An, K. J.; Hwang, Y. S.; Park, J. G.; Noh, H. J.; Kim, J. Y.; Park, J. H.; Hwang, N. M.; Hyeon, T., Ultra-large-scale syntheses of monodisperse nanocrystals. *Nature Materials* **2004**, *3* (12), 891-895.
4. Willis, A. L.; Turro, N. J.; O'Brien, S., Spectroscopic characterization of the surface of iron oxide nanocrystals. *Chemistry of Materials* **2005**, *17* (24), 5970-5975.
5. Yin, M.; Willis, A.; Redl, F.; Turro, N. J.; O'Brien, S. P., Influence of capping groups on the synthesis of gamma- Fe_2O_3 nanocrystals. *Journal of Materials Research* **2004**, *19* (4), 1208-1215.
6. Xu, Z. C.; Shen, C. M.; Hou, Y. L.; Gao, H. J.; Sun, S. S., Oleylamine as both reducing agent and stabilizer in a facile synthesis of magnetite nanoparticles. *Chemistry of Materials* **2009**, *21* (9), 1778-1780.
7. Kashchiev, D.; van Rosmalen, G. M., Review: nucleation in solutions revisited. *Crystal Research and Technology* **2003**, *38* (7-8), 555-574.
8. Balluffi, R. W.; Allen, S. M.; Carter, W. C., *Kinetic processes in materials*. John Wiley& Sons: New York, 2002.

9. Guardia, P.; Batlle-Brugal, B.; Roca, A. G.; Iglesias, O.; Morales, M. P.; Serna, C. J.; Labarta, A.; Batlle, X., Surfactant effects in magnetite nanoparticles of controlled size. *Journal of Magnetism and Magnetic Materials* **2007**, *316* (2), E756-E759.
10. Thunemann, A. F.; Schutt, D.; Kaufner, L.; Pison, U.; Mohwald, H., Maghemite nanoparticles protectively coated with poly(ethylene imine) and poly(ethylene oxide)-block-poly(glutamic acid). *Langmuir* **2006**, *22* (5), 2351-2357.
11. Park, H.; Ayala, P.; Deshusses, M. A.; Mulchandani, A.; Choi, H.; Myung, N. V., Electrodeposition of maghemite (γ -Fe₂O₃) nanoparticles. *Chemical Engineering Journal* **2008**, *139* (1), 208-212.
12. Jia, C.-J.; Sun, L.-D.; Luo, F.; Han, X.-D.; Heyderman, L. J.; Yan, Z.-G.; Yan, C.-H.; Zheng, K.; Zhang, Z.; Takano, M.; Hayashi, N.; Eltschka, M.; Klaeui, M.; Ruediger, U.; Kasama, T.; Cervera-Gontard, L.; Dunin-Borkowski, R. E.; Tzvetkov, G.; Raabe, J., Large-scale synthesis of single-crystalline iron oxide magnetic nanorings. *Journal of the American Chemical Society* **2008**, *130* (50), 16968-16977.
13. Teng, X. W.; Yang, H., Effects of surfactants and synthetic conditions on the sizes and self-assembly of monodisperse iron oxide nanoparticles. *Journal of Materials Chemistry* **2004**, *14* (4), 774-779.
14. Sun, Y. K.; Ma, M.; Zhang, Y.; Gu, N., Synthesis of nanometer-size maghemite particles from magnetite. *Colloids and Surfaces A-Physicochemical and Engineering Aspects* **2004**, *245* (1-3), 15-19.
15. Palchoudhury, S.; An, W.; Xu, Y.; Qin, Y.; Zhang, Z.; Chopra, N.; Holler, R. A.; Turner, C. H.; Bao, Y., Synthesis and growth mechanism of iron oxide nanowhiskers. *Nano Letters* **2011**, *11* (3), 1141-1146.

16. Ganguly, A.; Kundu, R.; Ramanujachary, K. V.; Lofland, S. E.; Das, D.; Vasanthacharya, N. Y.; Ahmad, T.; Ganguli, A. K., Role of carboxylate ion and metal oxidation state on the morphology and magnetic properties of nanostructured metal carboxylates and their decomposition products. *Journal of Chemical Sciences* **2008**, *120* (6), 521-528.
17. Garg, A. N.; Lanjewar, R. B., Mossbauer spectroscopic identification of thermal-decomposition products in iron(III) carboxylates. *Journal of Radioanalytical and Nuclear Chemistry-Letters* **1995**, *199* (6), 443-452.
18. Garcia-bennet, A. Method for manufacturing a nanoporous framework and a nanoporous framework thus produced. PCT/EP2005/009047, 2009.
19. Abrahamson, H. B.; Lukaski, H. C., Synthesis and characterization of iron stearate compounds. *Journal of Inorganic Biochemistry* **1994**, *54* (2), 115-130.
20. Lu, Y. Q.; Miller, J. D., Carboxyl stretching vibrations of spontaneously adsorbed and LB-transferred calcium carboxylates as determined by FTIR internal reflection spectroscopy. *Journal of Colloid and Interface Science* **2002**, *256* (1), 41-52.
21. Hyeon, T., Chemical synthesis of magnetic nanoparticles. *Chemical Communications* **2003**, (8), 927-934.
22. Kwon, S. G.; Piao, Y.; Park, J.; Angappane, S.; Jo, Y.; Hwang, N. M.; Park, J. G.; Hyeon, T., Kinetics of monodisperse iron oxide nanocrystal formation by "heating-up" process. *Journal of the American Chemical Society* **2007**, *129* (41), 12571-12584.
23. Bao, N. Z.; Shen, L. M.; An, W.; Padhan, P.; Turner, C. H.; Gupta, A., Formation mechanism and shape control of monodisperse magnetic CoFe₂O₄ nanocrystals. *Chemistry of Materials* **2009**, *21* (14), 3458-3468.

24. Bao, Y.; Beerman, M.; Pakhomov, A. B.; Krishnan, K. M., Controlled crystalline structure and surface stability of cobalt nanocrystals. *Journal of Physical Chemistry B* **2005**, *109* (15), 7220-7222.
25. Bao, Y.; An, W.; Turner, C. H.; Krishnan, K. M., The critical role of surfactants in the growth of cobalt nanoparticles. *Langmuir* **2010**, *26* (1), 478-483.
26. Palchoudhury, S.; Xu, Y.; Goodwin, J.; Bao, Y., Synthesis of iron oxide nanoworms. *Journal of Applied Physics* **2011**, *109* (7), 07E314 (1-3).
27. Bao, N. Z.; Shen, L. M.; Wang, Y. H. A.; Ma, J. X.; Mazumdar, D.; Gupta, A., Controlled growth of monodisperse self-supported superparamagnetic nanostructures of spherical and rod-like CoFe₂O₄ nanocrystals. *Journal of the American Chemical Society* **2009**, *131* (36), 12900-12901.
28. Xu, Y.; Qin, Y.; Palchoudhury, S.; Bao, Y., Water soluble iron oxide nanoparticles with high stability and selective surface functionality. *Langmuir* **2011**, *27* (14), 8990-8997.
29. Zhang, J.; Liu, X.; Guo, X.; Wu, S.; Wang, S., A general approach to fabricate diverse noble-metal (Au, Pt, Ag, Pt/Au)/Fe(2)O(3) hybrid nanomaterials. *Chemistry-A European Journal* **2010**, *16* (27), 8108-8116.
30. Ge, J.; Hu, Y.; Biasini, M.; Dong, C.; Guo, J.; Beyermann, W. P.; Yin, Y., One-step synthesis of highly water-soluble magnetite colloidal nanocrystals. *Chemistry-A European Journal* **2007**, *13* (25), 7153-7161.
31. Peng, Z.; Yang, H., Designer platinum nanoparticles: Control of shape, composition in alloy, nanostructure and electrocatalytic property. *Nano Today* **2009**, *4* (2), 143-164.
32. Bradley, J. S., *Clusters and Colloids*. Weinheim, Germany, 1994.

33. Zanchet, D.; Micheel, C. M.; Parak, W. J.; Gerion, D.; Alivisatos, A. P., Electrophoretic isolation of discrete Au nanocrystal/DNA conjugates. *Nano Letters* **2001**, *1* (1), 32-35.
34. Li, Y.; Zheng, Y.; Gong, M.; Deng, Z., Pt nanoparticles decorated with a discrete number of DNA molecules for programmable assembly of Au-Pt bimetallic superstructures. *Chemical Communications* **2012**, *48* (31), 3727-3729.
35. Yang, J.; Lee, J. Y.; Too, H.-P.; Chow, G.-M.; Gan, L. M., Stabilization of Pt nanoparticles by single stranded DNA and the binary assembly of Au and Pt nanoparticles without hybridization. *Journal of Nanoparticle Research* **2006**, *8* (6), 1017-1026.
36. Liu, Y. P.; Meyer-Zaika, W.; Franzka, S.; Schmid, G.; Tsoli, M.; Kuhn, H., Gold-cluster degradation by the transition of B-DNA into A-DNA and the formation of nanowires. *Angewandte Chemie-International Edition* **2003**, *42* (25), 2853-2857.
37. De, M.; Ghosh, P. S.; Rotello, V. M., Applications of nanoparticles in biology. *Advanced Materials* **2008**, *20* (22), 4225-4241.
38. Townsend, D. M.; Tew, K. D.; Tapiero, H., The importance of glutathione in human disease. *Biomedicine & Pharmacotherapy* **2003**, *57* (3-4), 145-155.
39. Sadowitz, P. D.; Hubbard, B. A.; Dabrowiak, J. C.; Goodisman, J.; Tacka, K. A.; Aktas, M. K.; Cunningham, M. J.; Dubowy, R. L.; Souid, A. K., Kinetics of cisplatin binding to cellular DNA and modulations by thiol-blocking agents and thiol drugs. *Drug Metabolism and Disposition* **2002**, *30* (2), 183-190.
40. Pelka, J.; Gehrke, H.; Esselen, M.; Tuerk, M.; Crone, M.; Braese, S.; Muller, T.; Blank, H.; Send, W.; Zibat, V.; Brenner, P.; Schneider, R.; Gerthsen, D.; Marko, D., Cellular uptake of platinum nanoparticles in human colon carcinoma cells and their impact on cellular redox systems and DNA integrity. *Chemical Research in Toxicology* **2009**, *22* (4), 649-659.

41. Fujiwara, M.; Grubbs, R. H.; Baldeschwieler, J. D., Characterization of pH-dependent poly(acrylic acid) complexation with phospholipid vesicles. *Journal of Colloid and Interface Science* **1997**, *185* (1), 210-216.
42. Scott, C.; Gruenberg, J., Ion flux and the function of endosomes and lysosomes: pH is just the start. *Bioessays* **2010**, *33*, 103-110.

CHAPTER 4

FUTURE WORK

The Pt NPs on iron oxide support showed effective DNA interactions in this research. The future work would involve further synthesis, characterization and *in vitro* biological studies to consolidate the research hypothesis. The potential applications of the Pt-attached iron oxide NPs would also be investigated. These studies are elaborated as follows.

4.1 Synthesis

The prospective future syntheses would include formation of new iron oxide NP morphologies such as NWs and nanofishes, multiple Pt NP attachments on other iron oxide NP shapes, a phase transfer of the Pt attached non-spherical iron oxide NPs, and a protective polymer encapsulation of the integrated NPs in aqueous solution.

4.1.1 Iron Oxide Nanoworms and Nanofishes

The first synthetic goal would be to reproducibly form pure NWs and nanofishes in an organic solvent. Superparamagnetic iron oxide NWs (Figure 4.1a and b) and nanofishes (Figure 4.1c) were developed in this research using a thermal decomposition technique (iron oleate precursor). However, the formation mechanisms of these nanostructures were unclear. Therefore, future experiments would attempt to discover the growth mechanism of these morphologies for good reproducibility. It would be interesting to study the magnetic properties of these iron oxide nanostructures because they could potentially be used for drug delivery and imaging.

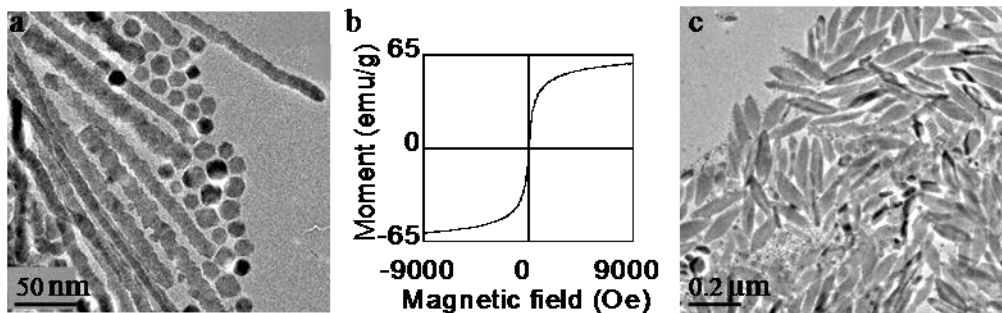


Figure 4.1. Different shapes of iron oxide NPs to be reproducibly synthesized in the future: (a) superparamagnetic NWs, (b) M - H curve of sample a, and (c) nanofishes.

4.1.2 *Platinum Attachments on Iron Oxide Nanoparticles of Other Shapes*

The Pt NP attachments in an organic solvent would be investigated with other shapes of iron oxide NPs, such as nanocubes and superparamagnetic NWs. This would give a complete understanding of the influence of NP shapes on the Pt attachments via an organic route. These results would help predict the most suitable morphology of the support for general heterogeneous nucleations of small NPs.

4.1.3 *Phase Transfer of the Integrated Nanoparticles Synthesized via Organic Route*

The iron oxide nanoplates provided good Pt NP attachments using the organic route. However, it was challenging to bring the nanoplates in an aqueous solution due to the heavy organic surfactant coating. Therefore, a ligand exchange technique would be developed to transfer the multiple Pt NP-attached nanoplates to an aqueous phase for the future DNA interaction studies. The method would also be extended to other organic phase nanostructures with good Pt attachments.

4.1.4 Polymer Encapsulation of the Platinum-Iron Oxide Integrated Nanoparticle

The interaction of Pt attached iron oxide NPs with biomolecules was not specific to DNA. Common biomolecules found in the body, such as glutathione (mitochondria) and serum albumin (blood plasma), also showed interaction with these NPs (Chapter 3). The integrated NPs can reach their therapeutic target efficiently if these non-target interactions are minimized. Easy accessibility of the Pt NPs in these aqueous route based NP samples could possibly facilitate the non-target interactions.

One solution would be to use the NPs synthesized via an organic approach. Here, Pt NPs were directly attached to the iron oxide surface, and the polymer surrounding the integrated NP could minimize non-specific interaction. Tumor targeting agents, such as peptides, antibodies, or proteins could be conjugated to the biocompatible polymer for more specific interaction. Peptide conjugation is more economic and favorable because antibodies and proteins, cause a large increase in the hydrodynamic diameter of NPs.¹ These targeted NPs will likely be endocytosed by the cancer cells.^{2,3} The protective polymer will possibly degrade in the acidic environment of endosomes.⁴ The released NPs can then potentially interact with the DNA.

Alternatively, biocompatible polymers such as lipids⁵⁻⁷ or micelles^{8,9} could be used to encapsulate the Pt attached iron oxide NPs made via an aqueous route (Figure 4.2). Recently, amphiphilic block copolymer encapsulated iron oxide NPs showed a promising blood circulation time and drug carrying capacity.¹⁰ Such polymer encapsulated NPs show easy uptake by cancer cells via enhanced permeability and retention.¹¹ The release of NPs can be controlled via proper choice of the encapsulating polymer. These simple approaches could potentially reduce the loss of Pt NPs from the integrated nanostructures.

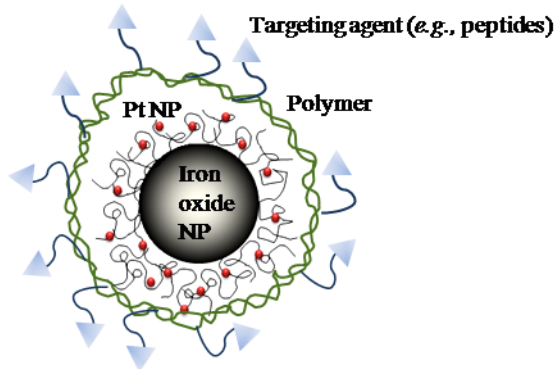


Figure 4.2. Polymer encapsulation of the Pt-iron oxide NPs to minimize non-target interaction

4.2 Characterization

The future characterizations would serve to better understand the DNA interaction mechanism of the Pt-iron oxide NPs. The DNA interaction of the Pt-iron oxide NPs would be characterized by local electrode atom probe (LEAP), XPS, and FTIR. The interactions would also be investigated in detail via simulation.

4.2.1 Quantification

The NP-DNA interaction could be further quantified via XPS, Imago LEAP and FTIR.

FTIR: The chemical bonds on the NP surfaces can be detected in an FTIR analysis. Therefore, the FTIR on a powder sample of Pt-iron oxide NPs interacted with DNA would effectively identify the DNA on the NP surface.

XPS: The powdered sample would also be used for the XPS analysis. The XPS detects all the principal elements of the DNA (N, P, C, and O), except H. Therefore, the XPS could be used to quantify the adsorbed DNA on the NP surfaces.¹² The quantification based on N and P detections would be most accurate because these elements are less affected by the contaminations during sample preparation.

LEAP: The LEAP allows three-dimentional mapping of the atoms in a conducting sample. The DNA-NP sample would be deposited on a conducting probe for analysis on the Imago LEAP. This would provide a good quantitative estimate of the DNA interacted with the NPs.

4.2.2 *Simulation*

Small, heavy metal NPs, such as Au and Pt, showed strong interaction with DNA bases according to previous theoretical reports. These reports used Becke, 3-parameter, Lee-Yang-Parr (B3LYP) density functional theory calculations to predict DNA-NP binding energies.^{1,2} Based on binding energy, formation enthalpy, and formation free energy calculations, Au NPs showed preferable binding to the free N atoms of guanine (G), cytosine (C), adenine (A), and the O atom of thymine (T).¹³ However, the complexation was strongest with G bases. This study had used size expanded DNA bases (y-bases) as a model system. Pt NP binding was studied using a peptide nucleic acid (PNA) model system.¹⁴ PNA contains DNA bases, but has a peptide backbone instead of phosphodiesters. Based on relative energy calculations with respect to highest occupied molecular orbital (HOMO), it was concluded that G-binding was most energy efficient for Pt NPs. However, the close energy gap between the nucleobases suggested nearly equal complexation capacity of all four bases. The affinity of DNA nucleobases and the phosphodiester backbone for Pt attached iron oxide NPs could be calculated, using similar methods. This could predict the accurate DNA binding site for these NPs.

4.3 *Biological Studies*

The purpose of the biological studies would be to investigate the intracellular behavior of the

Pt attached iron oxide NPs for future therapeutic applications. Additionally, the potential of the integrated NPs in radiation therapy would also be explored.

4.3.1 DNA Interaction of Platinum Attached Iron Oxide Nanoparticles In Vitro

The Pt-iron oxide NPs synthesized via an aqueous phase was used to show successful DNA interactions in Chapter 3. These NPs would be used for *in vitro* experiments with mammalian cell lines to show the distribution and DNA interaction of the NPs within the cell. The cytotoxicity of the NPs towards mammalian cells could be estimated from these studies using an MTT (3-(4,5-dimethylthiazol-2-yl)-5-(3-carboxymethoxyphenyl)-2-(4-sulfophenyl)-2H-tetrazolium) assay.

Next, the DNA interaction of Pt-iron oxide NPs synthesized via an organic route would be investigated for comparison. Here, gel electrophoresis experiments would be designed with DNA samples interacted with free small Pt NPs, Pt-iron oxide NPs synthesized via an aqueous route, and Pt-iron oxide NPs synthesized via an organic route. Subsequently, *in vitro* studies could be performed with the Pt NP-attached iron oxide NPs, synthesized via an organic route.

4.3.2 Platinum Attached Iron Oxide Nanoparticles as Radiation Therapy Enhancers

Noninvasive radiation therapy is attractive for treatment of inoperable tumors (*e.g.*, brain tumors) and solid tumors. Conventional radiation therapy (such as x-rays or γ -rays) dosages are limited by normal cell damage in the path of radiation.¹⁵ Recently, heavy metal (Au) NPs were used as radiation therapy sensitizers.^{16,17} The NPs could localize the radiation to the tumor site. The ionizing radiations of different energies induced different types of interactions in Au NPs.¹⁸ For example, 10-500 keV photons produced electrons, characteristic x-rays, and auger electrons

from Au NPs (photoelectric effect). Photons above 500 keV induced phonon emissions (Compton effect). Photons and positrons resulted from high energy photon (> 1.02 MeV) irradiations. However, Auger cascades were considered to be the major contributors for radiation enhancing effect of Au NPs.¹⁹ Such Auger cascades resulted when electrons from outer shells dropped to fill radiation induced, inner-shell electron vacancies.

Small Au NPs had shown great potential as radiation enhancers because they could induce 86% one-year survival rate in tumor-bearing mice compared to 20% for x-rays alone (250 kVp).²⁰ Theoretical calculations also predicted a high radiation enhancing effect for small Au NPs.²¹ Recently, a high molar concentration of Au NPs (~1:1 DNA: NP molar ratio) was found to facilitate highest radiation dose enhancement (6 times).²² However, this report involved larger Au NPs (8-92 nm), likely due to the challenge in targeting the ultrasmall NPs.

The targeting inefficiency could be largely overcome by using our Pt attached iron oxide NPs. Pt is a heavy metal like Au, and could potentially induce radiation enhancement.²³ Therefore, a promising future scope would be to investigate the radiation enhancing capacity of these integrated NPs (Figure 4.3).

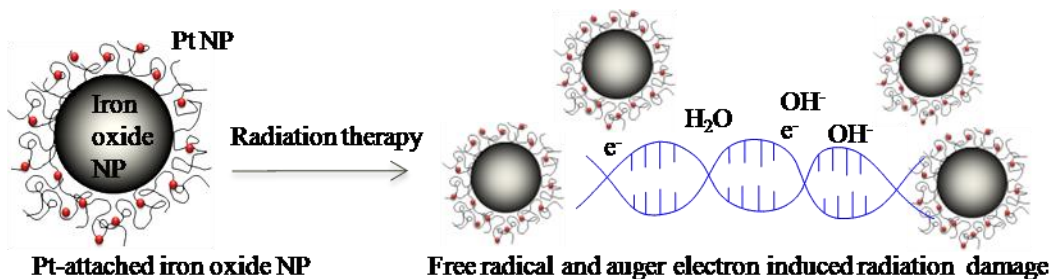


Figure 4.3. Future application of Pt-attached iron oxide NPs as radiation therapy sensitizers

In conclusion, the multiple Pt-attached iron oxide NPs synthesized in this research could be potentially used for applications, such as chemotherapy and radiation therapy enhancement. This chapter described the future work to prove the therapeutic potential of the integrated NPs, and

the prospective future scope of the NPs. Successful DNA interaction of Pt-iron oxide NP has been shown in this research (Chapter 3). This could be very promising for chemotherapeutic purposes, although further investigations are still required. The following chapter summarizes all the promising results obtained, including the DNA interactions.

References

1. Peng, X.; Qian, X.; Mao, H.; Wang, A.; Chen, Z.; Nie, S.; Shin, D., Targeted magnetic iron oxide nanoparticles for tumor imaging and therapy. *International Journal of Nanomedicine* **2008**, 3 (3), 311-321.
2. Douziech-Eyrolles, L.; Marchais, H.; Herve, K.; Munnier, E.; Souce, M.; Linassier, C.; Dubois, P.; Chourpa, I., Nanovectors for anticancer agents based on superparamagnetic iron oxide nanoparticles. *International Journal of Nanomedicine* **2007**, 2 (4), 541-550.
3. Arbab, A. S.; Wilson, L. B.; Ashari, P.; Jordan, E. K.; Lewis, B. K.; Frank, J. A., A model of lysosomal metabolism of dextran coated superparamagnetic iron oxide (SPIO) nanoparticles: implications for cellular magnetic resonance imaging. *NMR in Biomedicine* **2005**, 18 (6), 383-389.
4. Xu, Y.; Qin, Y.; Palchoudhury, S.; Bao, Y., Water Soluble Iron Oxide Nanoparticles with High Stability and Selective Surface Functionality. *Langmuir* **2011**, 27 (14), 8990-8997.
5. Senarath-Yapa, M. D.; Phimphivong, S.; Coym, J. W.; Wirth, M. J.; Aspinwall, C. A.; Saavedra, S. S., Preparation and characterization of poly(lipid)-coated, fluorophore-doped silica nanoparticles for biolabeling and cellular imaging. *Langmuir* **2007**, 23 (25), 12624-12633.
6. Li, P.; Li, D.; Zhang, L.; Li, G.; Wang, E., Cationic lipid bilayer coated gold nanoparticles-mediated transfection of mammalian cells. *Biomaterials* **2008**, 29 (26), 3617-3624.
7. Hu, J.; Wu, T.; Zhang, G.; Liu, S., Efficient synthesis of single gold nanoparticle hybrid amphiphilic triblock copolymers and their controlled self-assembly. *Journal of the American Chemical Society* **2012**.
8. Wu, L.; Brazel, C. S., Modifying the release of proxyphylline from PVA hydrogels using surface crosslinking. *International Journal of Pharmaceutics* **2008**, 349 (1-2), 144-151.

9. Talelli, M.; Rijcken, C. J. F.; Lammers, T.; Seevinck, P. R.; Storm, G.; van Nostrum, C. F.; Hennink, W. E., Superparamagnetic Iron oxide nanoparticles encapsulated in biodegradable thermosensitive polymeric micelles: toward a targeted nanomedicine suitable for image-guided drug delivery. *Langmuir* **2009**, *25* (4), 2060-2067.
10. Nasongkla, N.; Bey, E.; Ren, J.; Ai, H.; Khemtong, C.; Guthi, J. S.; Chin, S.-F.; Sherry, A. D.; Boothman, D. A.; Gao, J., Multifunctional polymeric micelles as cancer-targeted, MRI-ultrasensitive drug delivery systems. *Nano Letters* **2006**, *6* (11), 2427-2430.
11. Maeda, H.; Bharate, G. Y.; Daruwalla, J., Polymeric drugs for efficient tumor-targeted drug delivery based on EPR-effect. *European Journal of Pharmaceutics and Biopharmaceutics* **2009**, *71* (3), 409-419.
12. Petrovykh, D. Y.; Kimura-Suda, H.; Whitman, L. J.; Tarlov, M. J., Quantitative analysis and characterization of DNA immobilized on gold. *Journal of the American Chemical Society* **2003**, *125* (17), 5219-5226.
13. Sharma, P.; Sharma, S.; Singh, H.; Mitra, A., Interaction of size expanded DNA bases with small neutral gold nanoclusters. *Nanoelectronics Conference, 2008. INEC 2008. 2nd IEEE International* **2008**, 1083-1086.
14. Wang, X.; Pandey, R. R.; Singh, K. V.; Andavan, G. T. S.; Tsai, C.; Lake, R.; Ozkan, M.; Ozkan, C. S., Synthesis and characterization of peptide nucleic acid-platinum nanoclusters. *Nanotechnology* **2006**, *17* (5), 1177-1183.
15. Xu, X. G.; Bednarz, B.; Paganetti, H., A review of dosimetry studies on external-beam radiation treatment with respect to second cancer induction. *Physics in Medicine and Biology* **2008**, *53* (13), R193-R241.

16. Jelveh, S.; Chithrani, D. B., Gold nanostructures as a platform for combinational therapy in future cancer therapeutics. *Cancers* **2011**, *3*, 1081-1110.
17. Chithrani, D. B.; Jelveh, S.; Jalali, F.; van Prooijen, M.; Allen, C.; Bristow, R. G.; Hill, R. P.; Jaffray, D. A., Gold nanoparticles as radiation sensitizers in cancer therapy. *Radiation Research* **2010**, *173* (6), 719-728.
18. Mesbah, A., A review on gold nanoparticles radiosensitization effect in radiation therapy of cancer. *Reports of Practical Oncology and Radiotherapy* **2010**, *15*, 176-180.
19. Pradhan, A. K.; Nahar, S. N.; Montenegro, M.; Yu, Y.; Zhang, H. L.; Sur, C.; Mrozik, M.; Pitzer, R. M., Resonant x-ray enhancement of the auger effect in high-Z atoms, molecules, and nanoparticles: potential biomedical applications. *Journal of Physical Chemistry A* **2009**, *113* (45), 12356-12363.
20. Hainfeld, J. F.; Slatkin, D. N.; Smilowitz, H. M., The use of gold nanoparticles to enhance radiotherapy in mice. *Physics in Medicine and Biology* **2004**, *49* (18), N309-N315.
21. Carter, J. D.; Cheng, N. N.; Qu, Y.; Suarez, G. D.; Guo, T., Nanoscale energy deposition by x-ray absorbing nanostructures. *Journal of Physical Chemistry B* **2007**, *111* (40), 11622-11625.
22. Brun, E.; Sanche, L.; Sicard-Roselli, C., Parameters governing gold nanoparticle X-ray radiosensitization of DNA in solution. *Colloids and Surfaces B-Biointerfaces* **2009**, *72* (1), 128-134.
23. Kobayashi, K.; Usami, N.; Porcel, E.; Lacombe, S.; Le Sech, C., Enhancement of radiation effect by heavy elements. *Mutation Research-Reviews in Mutation Research* **2010**, *704* (1-3), 123-131.

CHAPTER 5

CONCLUSION

This dissertation reports the reproducible synthesis, characterization, DNA interaction, and future scope of multiple Pt NP decorated iron oxide NPs (Figure 5). The work is novel because multiple attachments of Pt NPs on iron oxide NP surfaces has proved challenging in earlier reports.^{1,2} Crystalline and size-tunable (~ 2 nm) multiple Pt NP attachments were obtained in this research, which has not been reported so far.³ Additionally, the crystalline iron oxide nanowhisker, nanoflower, and nanoplate morphologies have not been synthesized earlier via the thermal decomposition technique.^{4,5} The iron oxide nanoworms were also synthesized with good crystallinity and size control compared to earlier literature reports.⁶ Finally, the DNA interactions were reported for the Pt NPs attached on iron oxide seeds. Previous reports have shown DNA interaction with free Pt NPs.⁷⁻¹¹ The following paragraphs summarize the results obtained in this research.

First, single Pt NPs were attached on iron oxide nanospheres in organic solvent (Figure 5a). The reaction parameters for controlled Pt NP (~ 2 nm) attachment were investigated using this model system. A modified “heat-up” method was used for the spherical iron oxide ($\gamma\text{-Fe}_2\text{O}_3$) NPs. It was concluded that 140 °C reaction temperature and the presence of a weaker binding ligand (*e.g.*, trioctylphosphine oxide, TOPO) on iron oxide NP surfaces facilitated Pt NP attachment in organic phase.

Second, multiple Pt NPs were attached to spherical iron oxide NPs via two synthetic approaches (Figure 5b). One method (organic phase) involved growing the Pt NPs on iron oxide

seeds in organic solvent, followed by an aqueous phase transfer of the integrated NP. It was discovered that a high packing density of TOPO on the iron oxide seed surface could induce multiple Pt NP attachments. This method could potentially minimize loss of therapeutic Pt NPs before reaching the target due to the protective polymer coating on the integrated NP. In another simple approach, small Pt NPs were deposited on already phase transferred polyacrylic acid (PAA) coated iron oxide NPs. Here, UV reduction time played a key role in the size control of Pt NPs. The small Pt NPs were linked to the PAA surface coating of iron oxide seeds, and could potentially be more accessible for interaction.

Third, different shapes of iron oxide NPs were synthesized to increase the Pt NP attachment density on iron oxide surfaces via an organic phase approach (Figure 5c, upper).

Selective decomposition of the iron oleate precursor at 150 °C could form thin iron oxide (γ -Fe₂O₃) nanowhiskers (2 x 20 nm). A ligand (undecomposed oleate arm)-directed growth mechanism was proposed based on theoretical calculations and thermogravimetric analysis. The nanowhiskers were superparamagnetic, but showed some paramagnetic behavior, likely from the heavy ligand coating. Such ultrathin, one-dimensional iron oxide NPs has not been reported so far.

Highly crystalline, one-dimensional iron oxide (γ -Fe₂O₃) nanoworms could be synthesized via a modified “heat-up” method using large percentage coverage of TOPO. The reaction time controlled the length of nanoworms (diameter 12 nm) from 50-200 nm. Time-dependent reactions showed that aggregation of spherical iron oxide NPs resulted in the ferromagnetic nanoworms. The aggregation was likely induced by the increased surface coverage of weakly bound ligand, TOPO.

Iron oxide nanoplates (18 x 18 x 3 nm) and nanoflowers (15 nm) were formed from less dried and easy to handle iron oleate precursor. The nanoplates were thin and highly crystalline. They showed a mixture of superparamagnetism and paramagnetism, likely due to the high ligand coated surface. Based on mechanistic studies we concluded that preferential binding of potassium ethoxide (C_2H_5OK) played a significant role in nanoplate growth. Here, C_2H_5OK , a by-product from precursor synthesis, served as the shape-directing ligand. However, the growth mechanism for superparamagnetic iron oxide nanoflowers was very different. Here, the volatile reflux and large percentage of TOPO induced multiple nucleation events to produce a high nuclei count. The small nuclei followed oriented attachment to form the nanoflowers.

The organic phase Pt NP attachment was investigated using the different iron oxide NP morphologies. We concluded that nanoplates facilitated the most Pt NP attachment.

Finally, DNA interaction studies were reported using Pt attached iron oxide NPs produced in aqueous solution as a model system (Figure 5c, lower). Plasmid DNA-NP interaction was investigated using electrophoresis. Two types of interactions were concluded based on the agarose gel bands by comparing with the control DNA. This conclusion was further supported by electron microscopy, dynamic light scattering, and atomic absorption spectroscopy. Unfortunately, the Pt attached iron oxide NPs also showed non-specific interactions with other biomolecules, such as glutathione and bovine serum albumin. Even though this proof-of-concept study proves the DNA interaction ability of iron oxide supported Pt NPs, further consideration and medications are needed to reduce non-specific interactions. For example, polymer-encapsulation could significantly reduce the non-specific interaction of Pt NPs with other molecules.¹²

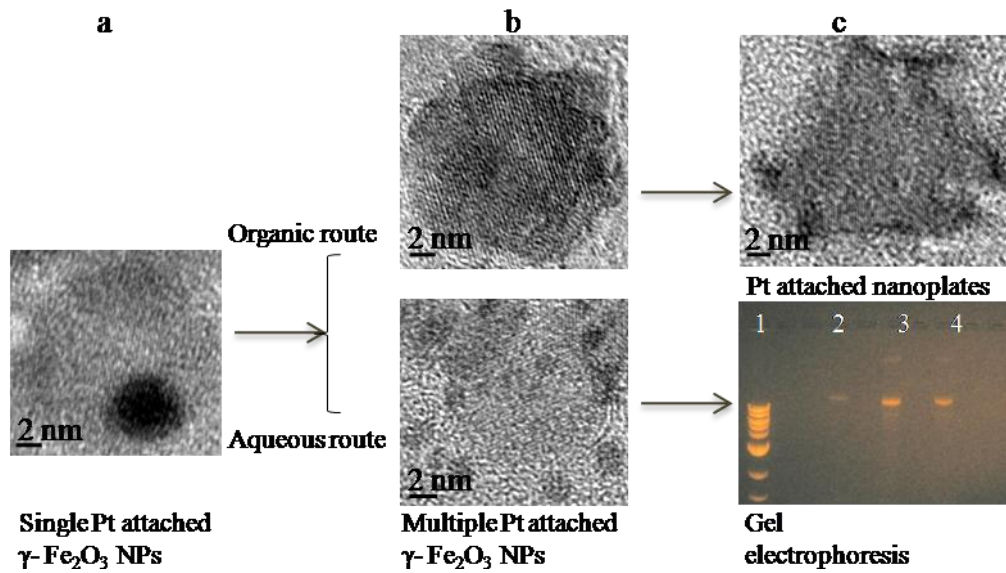


Figure 5. Conclusion: (a) single Pt NP-attached iron oxide NPs via an organic route, (b) multiple Pt NP attachments via organic (upper) and aqueous (lower) routes, and (c) Pt NP-attached nanoplates (upper) and DNA interaction of aqueous Pt-iron oxide NPs (lower).

References

1. Wang, C.; Xu, C. J.; Zeng, H.; Sun, S. H., Recent progress in syntheses and applications of dumbbell-like nanoparticles. *Advanced Materials* **2009**, *21* (30), 3045-3052.
2. Choi, S. H.; Bin Na, H.; Park, Y. I.; An, K.; Kwon, S. G.; Jang, Y.; Park, M.; Moon, J.; Son, J. S.; Song, I. C.; Moon, W. K.; Hyeon, T., Simple and generalized synthesis of oxide-metal heterostructured nanoparticles and their applications in multimodal biomedical probes. *Journal of the American Chemical Society* **2008**, *130* (46), 15573-15580.
3. Zhang, J.; Liu, X.; Guo, X.; Wu, S.; Wang, S., A general approach to fabricate diverse noble-metal (Au, Pt, Ag, Pt/Au)/Fe(2)O(3) hybrid nanomaterials. *Chemistry-A European Journal* **2010**, *16* (27), 8108-8116.
4. Park, M.; Lee, N.; Choi, S. H.; An, K.; Yu, S.-H.; Kim, J. H.; Kwon, S.-H.; Kim, D.; Kim, H.; Baek, S.-I.; Ahn, T.-Y.; Park, O. K.; Son, J. S.; Sung, Y.-E.; Kim, Y.-W.; Wang, Z.; Pinna, N.; Hyeon, T., Large-scale synthesis of ultrathin manganese oxide nanoplates and their applications to T1 MRI contrast agents. *Chemistry of Materials* **2011**, *23* (14), 3318-3324.
5. Bao, N. Z.; Shen, L. M.; Wang, Y. H. A.; Ma, J. X.; Mazumdar, D.; Gupta, A., Controlled growth of monodisperse self-supported superparamagnetic nanostructures of spherical and rod-like CoFe₂O₄ nanocrystals. *Journal of the American Chemical Society* **2009**, *131* (36), 12900-12901.
6. Park, J. H.; von Maltzahn, G.; Zhang, L. L.; Schwartz, M. P.; Ruoslahti, E.; Bhatia, S. N.; Sailor, M. J., Magnetic iron oxide nanoworms for tumor targeting and imaging. *Advanced Materials* **2008**, *20* (9), 1630-1631.

7. Asharani, P. V.; Xinyi, N.; Hande, M. P.; Valiyaveettil, S., DNA damage and p53-mediated growth arrest in human cells treated with platinum nanoparticles. *Nanomedicine* **2010**, 5 (1), 51-64.
8. Pelka, J.; Gehrke, H.; Esselen, M.; Tuerk, M.; Crone, M.; Braese, S.; Muller, T.; Blank, H.; Send, W.; Zibat, V.; Brenner, P.; Schneider, R.; Gerthsen, D.; Marko, D., Cellular uptake of platinum nanoparticles in human colon carcinoma cells and their impact on cellular redox systems and DNA integrity. *Chemical Research in Toxicology* **2009**, 22 (4), 649-659.
9. Sawosz, E.; Chwalibog, A.; Szeliga, J.; Sawosz, F.; Grodzik, M.; Rupiewicz, M.; Niemiec, T.; Kacprzyk, K., Visualization of gold and platinum nanoparticles interacting with *Salmonella Enteritidis* and *Listeria Monocytogenes*. *International Journal of Nanomedicine* **2010**, 5, 631-637.
10. Yang, J.; Pong, B.-K.; Lee, J. Y.; Too, H.-P., Dissociation of double-stranded DNA by small metal nanoparticles. *Journal of Inorganic Biochemistry* **2007**, 101 (5), 824-830.
11. Wang, X.; Pandey, R. R.; Singh, K. V.; Andavan, G. T. S.; Tsai, C.; Lake, R.; Ozkan, M.; Ozkan, C. S., Synthesis and characterization of peptide nucleic acid-platinum nanoclusters. *Nanotechnology* **2006**, 17 (5), 1177-1183.
12. Hu, J.; Wu, T.; Zhang, G.; Liu, S., Efficient synthesis of single gold nanoparticle hybrid amphiphilic triblock copolymers and their controlled self-assembly. *Journal of the American Chemical Society* **2012**.

APPENDIX

1. **Palchoudhury, S.**; Xu, Y.; Rushdie, A.; Yang, L.; Ritchie, S.; Bao, Y. "DNA Interaction of Multiple Platinum Attached Iron Oxide Nanoparticles" *Journal of Magnetism and Magnetic Materials* **2012** (to be submitted).
 2. **Palchoudhury, S.**; Xu, Y.; Rushdie, A.; Goodwin, J.; Bao, Y. "Synthesis of Iron Oxide Nanoflowers and Nanoplates" *Journal of Physical Chemistry C* **2012** (to be submitted).
 3. **Palchoudhury, S.**; An, W.; Xu, Y.; Qin, Y.; Zhang, Z.; Holler, R.; Turner, C. Heath; Chopra, N.; Bao, Y. "Synthesis and Growth Mechanism of Iron Oxide Nanowhiskers" *Nano Letters* **2011**, *11* (3), 1141-1146.
 4. **Palchoudhury, S.**; Xu, Y.; Goodwin, J.; Bao, Y. "Synthesis of Multiple Platinum Attached Iron Oxide Nanoparticles" *Journal of Material Chemistry* **2011**, *21*, 3966-3970.
 5. **Palchoudhury, S.**; Xu, Y.; Goodwin, J.; Bao, Y. "Synthesis of Iron Oxide Nanoworms" *Journal of Applied Physics* **2011**, *109* (7), 07E314 (1-3).
 6. **Palchoudhury, S.**; Xu, Y.; An, Wei; Turner, C. H.; Bao, Y. "Platinum Attachments on Iron Oxide Nanoparticle Surfaces" *Journal of Applied Physics* **2010**, *107* (9), 09B311 (1-3).
 7. Xu, Y.; **Palchoudhury, S.**; Yin, Q.; Bao, Y. "Make Conjugation Simple: A Facile Approach to Integrated Nanostructures" *Langmuir*. **2012** (submitted).
 8. Xu, Y.; Yin, Q.; **Palchoudhury, S.**; Bao, Y. "Water Soluble Iron Oxide Nanoparticles with High Stability and Selective Surface Functionality" *Langmuir*. **2011**, *27* (14), 8990-8997.
- Dozier, D.; **Palchoudhury, S.**; Bao, Y. "Synthesis of Iron Oxide Nanoparticles with Biological Coatings" *JOSHUA* **2010**, *7*, 16-18.